

Part III

Constitutive Aspects

Potentials and Limitations of Griffith's Energy Release Rate Criterion for Mode I Type Microcracking in Brittle Material

Bernhard Pichler^{1,2}, Christian Hellmich¹ and Luc Dormieux²

¹Institute for Mechanics of Materials and Structures,
Vienna University of Technology (TU Wien),
Karlsplatz 13/202,
A-1040, Vienna,
Austria.
E-mail: Bernhard.Pichler@tuwien.ac.at, Christian.Hellmich@tuwien.ac.at

²Laboratory for Materials and Structures (LMSGC),
National School of Civil Engineering (ENPC),
Avenue Blaise Pascal 2 et 4,
77455 Marne-la-Vallée,
France.
E-mail: Luc.Dormieux@lmsgc.enpc.fr

Summary

We here investigate potentials and limitations of Griffith's energy release rate criterion to describe effective stress-strain behavior of brittle materials damaged by mode I type propagating microcracks. For this purpose stiffness estimates for representative volume elements (RVEs) of a microcracked material (based on continuum micromechanics) are combined with the energy release rate criterion for the behavior of one single penny-shaped crack embedded in an infinite matrix subjected to remote uniform stresses (taken from linear-elastic fracture mechanics). This combination allows for studying the effect of stable (quasi-static) mode I propagation of open microcracks on the macroscopic behavior of microcracked material volumes subjected to different types of macroscopic loading. As regards uniaxial tension, the combined fracture-micromechanics approach predicts macroscopic strain-softening, resulting from propagation of cracks perpendicular to the loading direction. As regards uniaxial compression, consideration of non-zero crack openings is mandatory in order to predict a typical relation between tensile and compressive strengths, amounting to about 1:12. Thereby, uniaxial compressive failure is related to axial split-

ting, i.e. to propagation of open cracks in the loading direction. As regards axial splitting caused by confined compression, additional strength increase because of lateral confinement can be represented at least qualitatively. However, it turns out to be necessary to combine Griffith's energy release rate criterion with a stress criterion taking into account the sign of the microstresses in the vicinity of the crack edge.

1 Introduction

Microcracking is the dominant failure mechanism of brittle materials. Specific types of macroscopic loading lead to propagation of microcracks along their planes, while the relative displacement between the two crack surfaces is perpendicular to the crack growth direction. This type of crack propagation, referred to as cracking mode I, is observed under macroscopic uniaxial tension, macroscopic uniaxial compression, and macroscopic axial compression with lateral confinement. It is the central issue of the present paper.

Uniaxial tension experiments on brittle materials are very sensitive to imperfections [33]. Therefore, such experiments require very accurate and experienced handling of the specimen, the loading machine, and the measurement equipment [33]. In the post-peak regime of a uniaxial tension experiment, strain-softening is observed. Thereby, crack propagation is concentrated in a localization zone, i.e. to a narrow crack band [1]. The crack propagation direction is perpendicular to the direction of the applied tension. At the end of a uniaxial tension test on a brittle specimen, the sample splits up into two parts.

In uniaxial compression experiments with carefully lubricated interfaces between load platens and specimen, characterized by approximately uniform stress states within the tested sample, open cracks propagate in the direction of axial loading, through a predominantly mode I cracking mechanism [37]. In the post-peak regime of such a test, crack propagation is accompanied by strain-softening. Thereby, the number of cracks developing within a certain volume is rather large [36]. At the end of a uniaxial compression test on a brittle specimen, the sample splits up into many slender "columns", and final failure is due to buckling and bending, or tilting and sliding of these columns [37].

Complementing uniaxial compression experiments by lateral confinement pressure results in different failure mechanisms, related to different levels of confinement pressure:

- At small confinements, strain-softening is observed after the onset of axial splitting, and the final failure mode is the same as in unconfined uniaxial compression experiments.
- At moderate confinements, axial splitting is first associated with strain hardening, i.e. an increase of stress with increasing strain. Subsequently, strain softening and final failure is caused by shear-mode propagation of closed cracks which are inclined to the axis of uniaxial loading. This type of failure is referred to as faulting [19].
- At large confinements a transition from brittle failure to ductile material behavior is observed [19].

In this paper, we investigate whether effective macroscopic stress-strain behavior under uniaxial tension, uniaxial compression, and axial compression with lateral confinement, respectively, can be predicted by combining Griffith's energy release rate criterion for mode I crack propagation (taken from linear-elastic fracture mechanics) with the Mori-Tanaka stiffness estimate specified for microcracked materials (taken from continuum micromechanics). In Section 2, we shortly revisit Griffith's energy release rate criterion and determine, in the framework of the equivalent inclusion method, the energy release associated with the growth of a single crack embedded in an infinite matrix subjected to remote uniform stress states, namely uniaxial tensile stresses acting perpendicular to the crack plane, uniaxial compressive stresses acting parallel to the crack plane, and triaxial compressive stresses acting both parallel and perpendicular to the crack plane. Section 3 deals with continuum micromechanics. There, we give details on the Mori-Tanaka estimation of the effective stiffness of a representative material volume damaged by microcracks. Employing the simple concentration procedure proposed by Zaoui [39, 40, 41], we recall how these estimates can be derived on the basis of the strain state in a single penny-shaped crack surrounded by an infinite matrix subjected to fictitious remote (uniform) strains. The explicit consideration of these fictitious remote strains provides the link between continuum micromechanics and classical fracture mechanics, i.e. the link between the crack propagation criteria at the level of a single crack and the damage evolution at the level of the microcracked ("damaged") material. This link is worked out in detail for macroscopic uniaxial tension, uniaxial compression, and axial compression with lateral confinement in Section 4: Through the aforementioned upscaling technique, we study the effect of stable (quasi-static) mode I propagation of open microcracks on the macroscopic behavior of a microcracked material volume.

2 Single Crack Mechanics

2.1 Short Review of Griffith's Crack Propagation Criterion

Linear-elastic fracture mechanics deals with the behavior of a single crack embedded in an infinite matrix subjected to remote uniform stresses Σ^∞ (Fig. 2.1). Griffith [12] and Irwin [21] related crack propagation to the energy

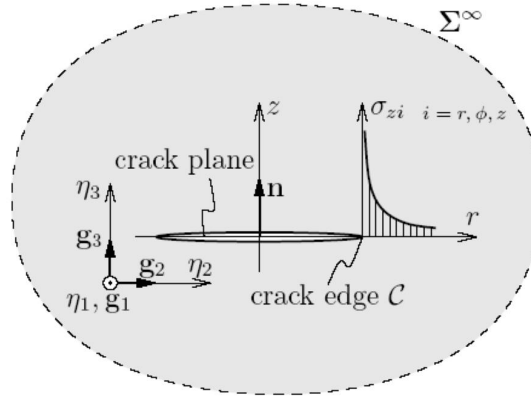


Fig. 2.1. Problem of linear-elastic fracture mechanics: A single penny-shaped crack (Fig. 2.2) is embedded in an infinite matrix subjected to remote uniform stresses Σ^∞

ε released upon an increase of the crack area A from zero to its current size, $\varepsilon = \varepsilon(\Sigma^\infty, A)$. The driving force for crack propagation is the energy release rate \mathbf{G} , which is obtained by derivation of ε with respect to A .

$$G(\Sigma^\infty, A) = \frac{\partial \varepsilon(\Sigma^\infty, A)}{\partial A} \quad (2.1)$$

The material resistance against crack propagation is referred to as \mathbf{G}_c . Comparison of $\mathbf{G}(\Sigma^\infty, A)$ with \mathbf{G}_c allows for identifying different types of crack behavior:

- a crack is stationary, i.e. it does not propagate, if

$$G(\Sigma^\infty, A) < G_c \quad (2.2)$$

- onset of cracking occurs, if

$$G(\Sigma^\infty, A) = G_c \quad (2.3)$$

- stable (quasi-static) crack propagation occurs, if (2.3) is satisfied and if

$$dG = \frac{\partial G}{\partial \Sigma^\infty} d\Sigma^\infty + \frac{\partial G}{\partial A} dA = 0 \quad \text{and} \quad dA > 0 \quad (2.4)$$

- and instable (dynamic) crack growth is associated with

$$G(\Sigma^\infty, A) > G_c \quad (2.5)$$

Since we restrict our considerations throughout the paper to penny-shaped cracks with crack radius a and crack half-opening c (Fig. 2.2), it is convenient to reformulate the expression of the energy release rate (2.1) as [26]

$$G = \frac{\partial \varepsilon}{\partial \alpha} \frac{\partial \alpha}{\partial A} = \frac{1}{2\alpha\pi} \frac{\partial \varepsilon}{\partial \alpha} \quad (2.6)$$

where, instead of the crack area $A = a^2\pi$, the crack radius a is introduced as the parameter describing the size of the crack.

2.2 Energy Released by Penny-Shaped Cracks Propagating in Mode I under Uniaxial and Triaxial Stress States

The energy ε , released upon crack growth from zero to its current size, can be determined in the framework of the equivalent inclusion method [9, 27, 18]. This method deals with two different types of subdomains within an infinite, linear-elastic matrix: inhomogeneities and inclusions (see, e.g., [27]). An inhomogeneity has an elastic stiffness C_i differing from the matrix stiffness C_m (Fig. 2.3a); whereas an inclusion has the same stiffness as the matrix, but exhibits eigenstrains ε^* [27] (Fig. 2.3b), also called stress-free strains [9].

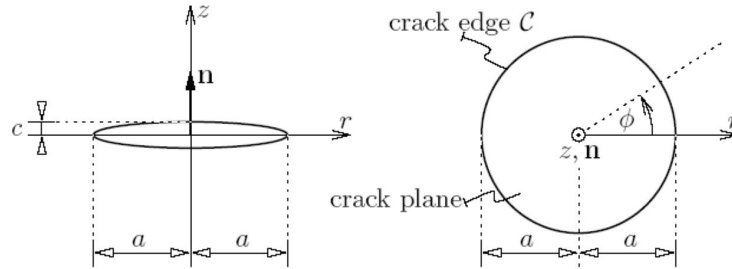


Fig. 2.2. Spatial dimensions of a penny-shaped crack (inhomogeneity) with unit normal to the crack plane \mathbf{n} , and definition of the crack coordinate system (r, ϕ, z)

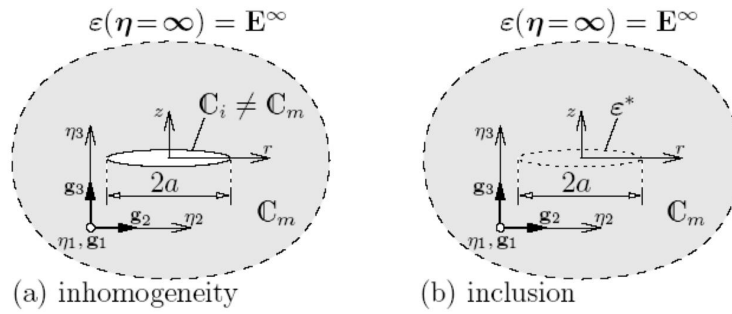


Fig. 2.3. Eshelby's equivalent inclusion problem: the behavior of (a) a single ellipsoidal inhomogeneity with stiffness C_i , embedded in a 3D infinite matrix of stiffness C_m , which is subject to remote uniform strain E^∞ , is modeled by (b) an ellipsoidal inclusion with equivalent eigenstrain ϵ^* , embedded in a homogeneous infinite body of stiffness C_m , which is subject to remote uniform strain E^∞

In case of remote uniform loading, either in terms of strains E^∞ or of stresses

$$\Sigma^\infty = C_m : E^\infty \quad (2.7)$$

the mechanical behavior of an infinite matrix containing a single ellipsoidal inhomogeneity is equivalent to that of an infinite matrix containing an

equally-shaped inclusion with eigenstrains ε^* [9] (Figs. 2.3a and 2.3b), reading as [13].

$$\varepsilon^* = -[\mathbb{S}_i^m + (C_i - C_m)^{-1} : C_m]^{-1} : E^\infty \quad (2.8)$$

where \mathbb{S}_i^m denotes the so-called Eshelby tensor, relating the eigenstrains ε^* to the difference between the total inclusion strains ε^i (eigenstrains plus elastic strains resulting from constraints of the inclusion by the surrounding matrix) and the remote uniform strains E^∞ [39].

$$\varepsilon^i = -E^\infty = \mathbb{S}_i^m : \varepsilon^* \quad (2.9)$$

ε^* enters the expression for the difference between the potential energy W of a Σ^∞ -loaded matrix with an inhomogeneity and that of the same matrix without any inhomogeneity, W_0 , [27].

$$\Delta W = W - W_0 = \frac{1}{2} V_i \Sigma^\infty \varepsilon^* \quad (2.10)$$

where V_i denotes the volume of the inhomogeneity. The energy difference ΔW is called interaction energy.

For an open crack, represented as an ellipsoidal inclusion with vanishing stiffness $C_i = 0$, the equivalent eigenstrains follow from (2.8) as

$$\varepsilon^* = (\mathbf{I} - \mathbb{S}_c^m)^{-1} : E^\infty \quad (2.11)$$

where \mathbf{I} denotes the fourth-order unity tensor, $I_{ijkl} = 1/2 (\delta_{ik}\delta_{jl} + \delta_{il}\delta_{kj})$, with δ_{ij} denoting the Kronecker delta. For a penny-shaped crack (Fig. 2.2) with unit normal \mathbf{n} pointing in the x_3 direction ($\theta=0$, Fig. 2.4), embedded in an isotropic matrix, the non-zero components of \mathbb{S}_c^m read as [18, 27].

$$\begin{aligned}
S_{1111} &= \frac{13-8\nu_m}{32(1-\nu_m)} \pi \frac{c}{a} + O\left(\frac{c}{a}\right)^2, & S_{2222} &= S_{1111}, \\
S_{1122} &= \frac{8\nu_m-1}{32(1-\nu_m)} \pi \frac{c}{a} + O\left(\frac{c}{a}\right)^2, & S_{2211} &= S_{1122}, \\
S_{1133} &= \frac{2\nu_m-1}{8(1-\nu_m)} \pi \frac{c}{a} + O\left(\frac{c}{a}\right)^2, & S_{2233} &= S_{1133}, \\
S_{3311} &= \frac{\nu_m}{1-\nu_m} \left(1 - \frac{4\nu_m+1}{8\nu_m} \pi \frac{c}{a}\right) + O\left(\frac{c}{a}\right)^2, & S_{3322} &= S_{3311}, \\
S_{2323} &= \frac{1}{2} \left(1 + \frac{\nu_m-2}{1-\nu_m} \frac{\pi c}{4a}\right) + O\left(\frac{c}{a}\right)^2, & S_{3131} &= S_{2323}, \\
S_{1212} &= \frac{7-8\nu_m}{32(1-\nu_m)} \pi \frac{c}{a} + O\left(\frac{c}{a}\right)^2, \\
S_{3333} &= 1 - \frac{1-2\nu_m}{1-\nu_m} \frac{\pi c}{4a} + O\left(\frac{c}{a}\right)^2, \text{ with } S_{ijkl} = S_{jikl} = S_{ijlk}
\end{aligned} \tag{2.12}$$

and with ν_m as the Poisson's ratio of the matrix. The crack interaction energy ΔW i.e. the change in potential energy because of the presence of the crack, is identical to Griffith's energy \mathcal{E} released upon an increase of the crack radius a from zero to its current size, so that [compare (10)]

$$\mathcal{E} = \frac{1}{2} V_c \Sigma^\infty \varepsilon^* \tag{2.13}$$

where V_c denotes the volume of the crack:

$$V_c = \frac{4\pi}{3} a^2 c \tag{2.14}$$

In the following, we consider three specific remote uniform stress states Σ^∞ (i) uniaxial tension acting orthogonal to the crack plane, (ii) uniaxial

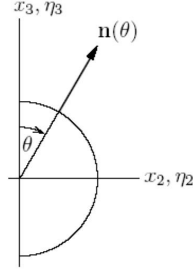


Fig. 2.4. Definition of the unit vector \mathbf{n} as a function of the angular coordinate θ

compression acting parallel to the crack plane, and (iii) a triaxial stress state where compressive stresses act both orthogonal as well as parallel to the crack plane.

For remote uniaxial tensile stress acting perpendicular to the crack plane (Fig. 2.1).

$$\Sigma^\infty = \Sigma_{33}^\infty \mathbf{g}_3 \otimes \mathbf{g}_3, \quad \Sigma_{33}^\infty \geq 0 \quad (2.15)$$

\mathcal{E} follows from specification of (2.13) for (2.14), (2.15), (2.11), (2.12), and (2.7) as

$$\mathcal{E} = \frac{8a^3 (\Sigma_{33}^\infty)^2}{3} \frac{1 - \nu_m^2}{E_m} + \frac{\pi a^3 (\Sigma_{33}^\infty)^2}{3} \frac{1 + 3\nu_m - 4\nu_m^3}{E_m} \left(\frac{c}{a} \right) + O\left(\frac{c}{a} \right)^2 \quad (2.16)$$

and the energy release rate follows from insertion of (2.16) into (2.6) as

$$G_I = \frac{4a (\Sigma_{33}^\infty)^2}{\pi} \frac{1 - \nu_m^2}{E_m} + \frac{a (\Sigma_{33}^\infty)^2}{3} \frac{1 + 3\nu_m - 4\nu_m^3}{E_m} \left(\frac{c}{a} \right) + O\left(\frac{c}{a} \right)^2 \quad (2.17)$$

In case of $(c/a) \ll 1$, the first term of (2.17) is significantly larger than the following terms, such that the energy released by a slightly opened crack ($a \gg c \neq 0$) can be approximated by that released by a sharp crack ($c = 0$).

For remote uniaxial compressive stress acting parallel to the crack plane (Fig. 2.1).

$$\Sigma^\infty = \Sigma_{11}^\infty \mathbf{g}_1 \otimes \mathbf{g}_1, \quad \Sigma_{11}^\infty \leq 0 \quad (2.18)$$

\mathcal{E} follows from specification of (2.13) for (2.14), (2.18), (2.11), (2.12), and (2.7) as

$$\mathcal{E} = \frac{2\pi a^3 (\Sigma_{11}^\infty)^2}{3E_m} \left(\frac{c}{a} \right) + O\left(\frac{c}{a} \right)^2 \quad (2.19)$$

and the energy release rate follows from insertion of (2.19) into (2.6) as

$$\mathcal{G} = \frac{2a (\Sigma_{11}^\infty)^2}{3E_m} \left(\frac{c}{a} \right) + O\left(\frac{c}{a} \right)^2 \quad (2.20)$$

Hence, energy release requires at least slight opening of the crack; and *no* energy is released if a sharp crack ($c = 0$) propagates.

For remote triaxial stress states in the form of compressive stress Σ_{11}^∞ acting parallel to the crack plane and confinement stress Σ_{33}^∞ acting both parallel and perpendicular to the crack plane (Fig. 2.1).

$$\Sigma^\infty = \Sigma_{11}^\infty \mathbf{g}_1 \otimes \mathbf{g}_1 + \Sigma_{33}^\infty (\mathbf{g}_2 \otimes \mathbf{g}_2 + \mathbf{g}_3 \otimes \mathbf{g}_3), \quad \Sigma_{11}^\infty \leq 0, \Sigma_{33}^\infty \leq 0 \quad (2.21)$$

\mathcal{E} follows from specification of (2.13) for (2.14), (2.21), (2.11), (2.12), and (2.7) as

$$\begin{aligned} \mathcal{E} = & \frac{8a^3 (\Sigma_{33}^\infty)^2}{3} \frac{1 - \nu_m^2}{E_m} + \frac{\pi a^3}{3} \left[\frac{(\Sigma_{33}^\infty)^2 (1 + \nu_m + 4\nu_m^2 - 4\nu_m^3)}{E_m} + \right. \\ & \left. + \frac{2(\Sigma_{11}^\infty)^2 - 2\Sigma_{11}^\infty \Sigma_{33}^\infty (1 + 3\nu_m - 2\nu_m^2)}{E_m} \right] \left(\frac{c}{a} \right) + O\left(\frac{c}{a} \right)^2 \end{aligned} \quad (2.22)$$

and the energy release rate follows from insertion of (2.22) into (2.6) as

$$\begin{aligned} \mathcal{G}_I = & \frac{4a (\Sigma_{33}^\infty)^2}{\pi} \frac{1 - \nu_m^2}{E_m} + \frac{a}{3} \left[\frac{(\Sigma_{33}^\infty)^2 (1 + \nu_m + 4\nu_m^2 - 4\nu_m^3)}{E_m} + \right. \\ & \left. + \frac{2(\Sigma_{11}^\infty)^2 - 2\Sigma_{11}^\infty \Sigma_{33}^\infty (1 + 3\nu_m - 2\nu_m^2)}{E_m} \right] \left(\frac{c}{a} \right) + O\left(\frac{c}{a} \right)^2 \end{aligned} \quad (2.23)$$

For very small confinements $\Sigma_{33}^\infty \ll \Sigma_{11}^\infty$, the first two terms on the right-hand side in (2.23), containing as factors $(c/a)^0 = 1$ and $(c/a)^1$, respectively, are of the same magnitude; otherwise the confinement pressure Σ_{33}^∞ governs the energy release rate in (2.23).

3 Representative Volume Elements Damaged by many Interacting Microcracks

3.1 Representative Volume Element (RVE) and Material Phases [17, 40, 31]

To study the mechanical behavior of a deformable solid with the help of continuum (micro)mechanics, constitutive material elements must be labeled and their geometrical evolution must be followed [40, 31]. A representative volume element (RVE) of a micro-heterogeneous material must be homogeneous on a macroscopic scale [17], which implies that the characteristic length ℓ of a RVE satisfies the condition

$$\ell \gg b \quad (3.1)$$

where b denotes the characteristic length of heterogeneities within the RVE, see Figs. 5b, 6b, and 6c for RVEs containing penny-shaped microcracks. Furthermore, in order to render differential calculus applicable in continuum mechanics, the condition

$$\{L, P\} \gg \ell \quad (3.2)$$

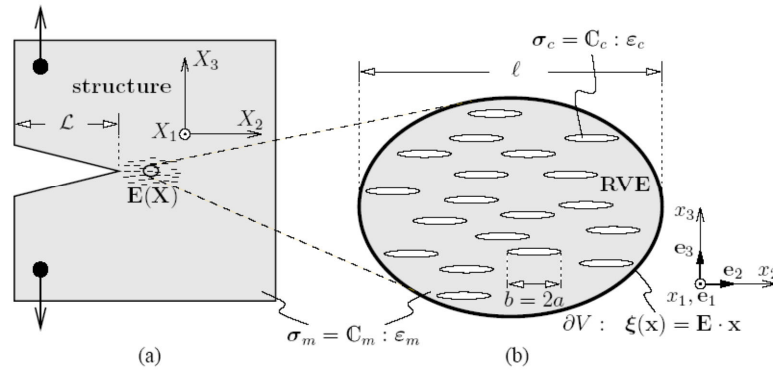


Fig. 3.1. Separation of scales: (a) Structure containing a fracture process zone ahead of a macrocrack and (b) RVE of a microcracked (damaged) material with cracks of identical size and orientation, subjected to displacements ξ related to “homogeneous strains” E at the boundary

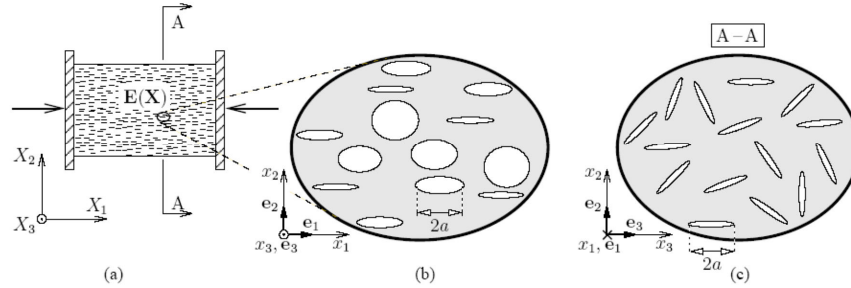


Fig. 3.2. (a) Microcracked sample tested in a uniaxial compression device, (b) and (c) sections through a RVE of a microcracked (damaged) material with equally-sized penny-shaped cracks, axisymmetrically distributed with respect to the x_1 axis

must be satisfied, where L denotes the characteristic length of the structure containing the RVE, and P stands for the characteristic length of structure excitations such as, e.g., surface-loads or wave lengths (Figs. 3.1a and 3.2a).

In general, the microstructure within each RVE is so complicated that it cannot be described in complete detail. Therefore, quasi-homogeneous sub-domains with known physical quantities (such as volume fractions and elastic properties) are reasonably chosen. They are called material phases. As regards microcracked (damaged) media, the introduction of two phases is most common in the open literature [5, 13, 23, 29, 30, 32]: (1) the sane (uncracked) matrix, and (2) the cracks in form of penny-shaped inhomogeneities.

For the sake of simplicity, we deal with RVEs comprising penny-shaped cracks with identical size. In case of uniaxial tension, we consider cracks of identical orientation where the crack normal \mathbf{n} is aligned with the direction of tensile loading. Notably, the problem of strain localization, as observed, e.g., in a uniaxial tension test on a brittle material, is beyond the scope of this paper. Moreover, we do not deal with macrocracking, and in particular not with the influence of many microcracks on the behavior of a macrocrack, such as done in [10, 20, 28, 8]. We rather describe the behavior of a material volume element (Fig. 3.1b) inside the localization zone (narrow crack band [1]) observed in a uniaxial tension experiment or *inside* the fracture process zone ahead of a macrocrack (Fig. 3.1). In case of axial compression (with and without lateral confinement), we consider axisymmetrically distributed cracks with normals \mathbf{n} orthogonal to the direction of the predominant axial compressive loading (Fig. 3.2).

3.2 Stress / Strain Averaging and Concentration [17, 39, 40, 41]

For studying deformation states of the RVE, a position vector \mathbf{x} is introduced. It labels, with resolution b , locations within the RVE and on its boundary. Subjecting the boundary ∂V of the RVE to displacements

$$\xi(\mathbf{x}) = \mathbf{E} \cdot \mathbf{x} \quad \text{on } \partial V \quad (3.3)$$

(Hashin boundary condition [15]), implies

$$\mathbf{E} = \langle \boldsymbol{\varepsilon} \rangle = \frac{1}{V} \int_V \boldsymbol{\varepsilon}(\mathbf{x}) dV = f_c \frac{1}{\theta^*} \int_0^{\theta^*} \boldsymbol{\varepsilon}_c[\mathbf{n}(\theta)] d\theta + f_m \boldsymbol{\varepsilon}_m \quad (3.4)$$

with $\langle \bullet \rangle := (1/V) \int \bullet dV$ as the volume average. f_m and f_c denote the volume fraction of the matrix and of the cracks, respectively. $\boldsymbol{\varepsilon}_m$ and $\boldsymbol{\varepsilon}_c[\mathbf{n}(\theta)]$ denote the (average) strains of the matrix and of cracks with normals \mathbf{n} defined by the angular coordinate θ (Fig. 2.4), respectively. The integral over $d\theta$ in (3.4) accounts for different crack orientations. Cracks of identical orientation, as observed under uniaxial tension (Fig. 3.1b), correspond to $\theta^* \rightarrow 0$. An axisymmetrical distribution of cracks, as observed under axial compression with and without lateral confinement (Figs. 3.2b and 3.2c), refers to $\theta^* = \pi$.

Linear-elastic behavior of the cracks and of the matrix is considered

$$\boldsymbol{\sigma}_c = \mathbf{C}_c : \boldsymbol{\varepsilon}_c \quad \text{and} \quad \boldsymbol{\sigma}_m = \mathbf{C}_m : \boldsymbol{\varepsilon}_m \quad (3.5)$$

with \mathbf{C}_c and \mathbf{C}_m as the stiffness of the cracks and of the matrix, respectively. Consequently, the superposition principle implies the existence of a linear relationship between macroscopic strains \mathbf{E} and (“microscopic”) strains $\boldsymbol{\varepsilon}_m$ and $\boldsymbol{\varepsilon}_c(\theta)$ [17].

$$\boldsymbol{\varepsilon}_c[\mathbf{n}(\theta)] = \mathbf{A}_c[\mathbf{n}(\theta)] : \mathbf{E} \quad \text{and} \quad \boldsymbol{\varepsilon}_m = \mathbf{A}_m : \mathbf{E} \quad (3.6)$$

with \mathbf{A}_m as the fourth-order concentration tensors of the matrix and $\mathbf{A}_c[\mathbf{n}(\theta)]$ as the fourth-order concentration tensors of the cracks with normal \mathbf{n} defined by θ . (3.4) and (3.6) imply that

$$f_c \frac{1}{\theta^*} \int_0^{\theta^*} \mathbf{A}_c[\mathbf{n}(\theta)] d\theta + f_m \mathbf{A}_m = \mathbf{I} \quad (3.7)$$

Insertion of (3.6) into (3.5), averaging over the resulting expressions for $\boldsymbol{\sigma}_c[\mathbf{n}(\theta)]$ and $\boldsymbol{\sigma}_m$ according to

$$\Sigma = \langle \sigma \rangle = f_c \frac{1}{\theta^*} \int_0^{\theta^*} \sigma_c[n(\theta)] d\theta + f_m \sigma_m \quad (3.8)$$

(with Σ as the macroscopic stress tensor), and accounting for (3.7) yields the macroscopic constitutive law

$$\Sigma = C_{\text{hom}} : E \quad (3.9)$$

with

$$C_{\text{hom}} = C_m + f_c \frac{1}{\theta^*} \int_0^{\theta^*} (C_c - C_m) : A_c[n(\theta)] d\theta \quad (3.10)$$

as the homogenized (macroscopic) elasticity tensor. We are left with the determination of the strain concentration tensors $A_c[n(\theta)]$, which are unknown so far. However, they can be estimated from Eshelby's matrix-inclusion problem.

3.3 Stiffness Estimation on the Basis of Eshelby's Matrix - Inclusion Problem [39, 40, 41]

The concentration tensors $A_c[n(\theta)]$ can be estimated on the basis of matrix-inclusion problems [39, 40, 41], such as the ones of Eshelby [9] or Laws [24, 25]. The stiffness of the same matrix of the (microcracked) RVE, C_m , is introduced as the stiffness of the matrix in the Eshelby problem (Figs. 3.1b and 2.3). Following Zaoui's concentration procedure [39, 40, 41], the average strains of each phase, $\varepsilon_c[n(\theta)]$ and ε_m , are set equal to the strains in a single ellipsoidal inclusion (with stiffness C_c and C_m , respectively) embedded in an infinite matrix of stiffness C_m , subjected to fictitious (uniform) strains E^∞ at infinity [39, 40, 41]. Accordingly, the average strains of penny-shaped microcracks embedded in a RVE follow as [39, 13].

$$\varepsilon_c[n(\theta)] = [I + S_c^m[n(\theta)] : C_m^{-1} : (C_c - C_m)]^{-1} : E^\infty \quad (3.11)$$

as can be shown from (2.8) and (2.9). In the same sense, the average strains of the matrix phase of the RVE are set equal to those prevailing in an inclusion of stiffness C_m , resulting in the trivial relation [39, 40, 41].

$$\varepsilon_m = E^\infty \quad (3.12)$$

The strains \mathbf{E}^∞ , prescribed at infinity to a matrix surrounding a single crack, must be related appropriately to the macroscopic strains \mathbf{E} , imposed as uniform boundary condition onto the RVE.

Assuming the case of a non-dilute concentration of cracks, their interaction needs to be considered. The simplest consideration of crack interaction consists of defining the fictitious remote strains \mathbf{E}^∞ such that the strain average rule (3.4) is satisfied [39, 40, 41], i.e. by insertion of (3.11) and (3.12) into (3.4).

$$\mathbf{E}^\infty = \left\{ f_m \mathbf{I} + f_c \frac{1}{\theta^*} \int_0^{\theta^*} [\mathbf{I} + \mathbb{S}_c^m[n(\theta)]: C_m^{-1} : (C_c - C_m)]^{-1} d\theta \right\}^{-1} : \mathbf{E} \quad (3.13)$$

Back-substitution of (3.12) into (3.10), while considering (3.6.1), yields the Mori-Tanaka estimate for the concentration tensors $\mathbf{A}_c[n(\theta)]$.

$$\begin{aligned} \mathbf{A}_c^{(MT)}[n(\theta)] &= [\mathbf{I} + \mathbb{S}_c^m[n(\theta)]: C_m^{-1} : (C_c - C_m)]^{-1} : \\ &: \left\{ f_m \mathbf{I} + f_c \frac{1}{\theta^*} \int_0^{\theta^*} [\mathbf{I} + \mathbb{S}_c^m[n(\theta)]: C_m^{-1} : (C_c - C_m)]^{-1} d\theta \right\}^{-1} \end{aligned} \quad (3.14)$$

Finally, insertion of (3.14) into (3.10) yields the Mori-Tanaka stiffness estimate of a material with microcracks [2, 3, 4, 11]

$$\begin{aligned} C_{\text{hom}}^{(MT)} &= C_m + f_c \frac{1}{\theta^*} \int_0^{\theta^*} (C_c - C_m) : [\mathbf{I} + \mathbb{S}_c^m[n(\theta)]: C_m^{-1} : (C_c - C_m)]^{-1} d\theta : \\ &: \left\{ f_m \mathbf{I} + f_c \frac{1}{\theta^*} \int_0^{\theta^*} [\mathbf{I} + \mathbb{S}_c^m[n(\theta)]: C_m^{-1} : (C_c - C_m)]^{-1} d\theta \right\}^{-1} \end{aligned} \quad (3.15)$$

Evidence for the suitability of considering crack interaction through (3.15) was gained in 2D, see [22]. There, it is shown that the 2D equivalent to the 3D Mori-Tanaka stiffness estimate used in this paper is quasi-identical to effective stiffnesses determined from a series of full structural computations (computer experiments [22]) of solids with different crack configurations (Fig. 3.3). These numerical analyses precisely accounted for (i) the load-carrying behavior of the matrix between the cracks and, hence, for (ii) crack interaction. The self consistent scheme and the differential scheme (for the latter see also [16]), however, overestimate the stiffness decrease with increasing crack density parameter (Fig. 3.3). This is the motivation to restrict our considerations to the Mori-Tanaka scheme.

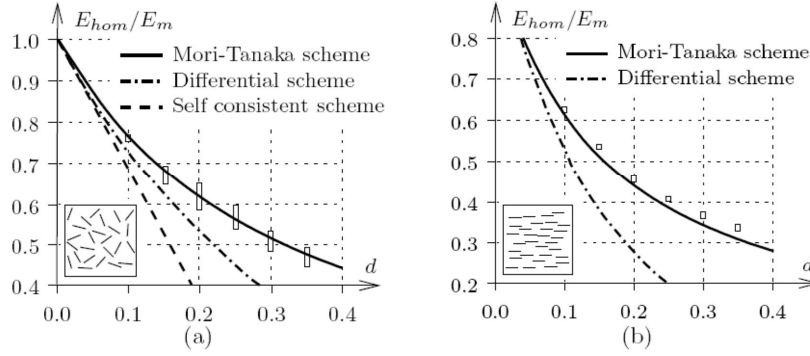


Fig. 3.3. Illustration of results of [22]: Young's modulus of a microcracked material over Young's modulus of the uncracked (sane) matrix, as a function of the (2D) crack density parameter; for (a) randomly orientated cracks and (b) parallel cracks. The vertical bars refer to the scatter interval of computed effective stiffnesses obtained from 15 numerical simulations with the same crack density, but with different, randomly generated configurations of interacting cracks.

3.4 Open and Empty Penny-Shaped Cracks

Specification of (3.15) for open and empty penny-shaped cracks, characterized by $C_c = 0$, yields

$$C_{\text{hom}}^{(MT)} = f_m C_m \left\{ f_m \mathbf{I} + f_c \frac{1}{\theta^*} \int_0^{\theta^*} [\mathbf{I} - \mathbb{S}_c^m[n(\theta)]]^{-1} d\theta \right\}^{-1} \quad (3.16)$$

Based on (2.14), the crack volume fraction reads as

$$f_c = NV_c = N \frac{4\pi}{3} a^2 c \quad (3.17)$$

with N denoting the number of cracks per unit volume.

As regards microcracking under uniaxial tension, we deal with RVEs comprising penny-shaped cracks of identical orientation (Fig. 3.1b) with $\mathbf{n} = \mathbf{n}(\theta=0)$. The corresponding stiffness estimate is obtained from specification of (3.16) for the limit case $\theta^* \rightarrow 0$. When also considering (3.17) and $f_m = 1 - f_c$, it reads as

$$C_{\text{hom}}^{(MT)} = (1 - f_c) C_m \left\{ (1 - f_c) \mathbf{I} + f_c [\mathbf{I} - \mathbb{S}_c^m[n(\theta=0)]]^{-1} \right\}^{-1} \quad (3.18)$$

where the non-vanishing components of $\$^m_c[n(\theta=0)]$, which are function of the crack aspect ratio c/α , are given in (2.12). For the limit case of sharp open cracks, characterized by the crack aspect ratio tending to zero: $c/\alpha \rightarrow 0$, the stiffness estimate (3.18) reduces to [6, 7]

$$C_{\text{hom}}^{(MT)} = C_m \left(\mathbf{I} + \frac{4\pi}{3} Na^3 \mathbf{T} \right)^{-1} \quad (3.19)$$

Thereby, the tensor \mathbf{T} , introduced by Dormieux and Kondo [6, 7], is defined as

$$\mathbf{T} = \lim_{c/\alpha \rightarrow 0} \left\{ \frac{c}{a} [\mathbf{I} - \$^m_c[n(\theta=0)]]^{-1} \right\} \quad (3.20)$$

The non-vanishing components of \mathbf{T} , exhibiting the symmetries $\mathbf{T}_{ijkl} = \mathbf{T}_{jikl} = \mathbf{T}_{ijlk}$, read as [6, 7]

$$\begin{aligned} T_{3311} = T_{3322} &= \frac{4v_m(1-v_m)}{(1-2v_m)\pi}, & T_{3333} &= \frac{4(1-v_m)^2}{(1-2v_m)\pi}, \\ T_{1313} = T_{2323} &= \frac{2(1-v_m)}{(2-v_m)\pi}, \end{aligned} \quad (3.21)$$

As regards microcracking under axial compression (with and without lateral confinement), we consider cracks with normals \mathbf{n} , oriented perpendicular to the direction of loading, i.e. $\mathbf{n} \perp \mathbf{e}_1$. The corresponding stiffness estimate is obtained from specification of (3.16) for $\theta^* = \pi$. When also considering (3.17) and $f_m = 1 - f_c$, this yields

$$C_{\text{hom}}^{(MT)} = (1 - f_c) C_m \left\{ (1 - f_c) \mathbf{I} + f_c \frac{1}{\pi} \int_0^\pi [\mathbf{I} - \$^m_c[n(\theta)]]^{-1} d\theta \right\}^{-1} \quad (3.22)$$

The secant-stiffness estimates of (3.19) and (3.22) depend on the actual degree of damage within the RVE, described by the crack volume fraction f_c [see (3.22)] or Budiansky's crack density parameter Na^3 [see (3.19)], respectively. For $f_c = \text{const}$ or $Na^3 = \text{const}$, respectively, they describe the behavior of stationary (non-propagating) cracks. Estimation of the homogenized stiffness during microcrack propagation requires quantification of the evolution of f_c or Na^3 , respectively, i.e. a damage evolution law is needed, which is derived subsequently. To end up with a fully micromechanics-based damage model for brittle materials, we will consider onset of

cracking and crack propagation of every *single microcrack* embedded in a RVE containing many such cracks.

3.5 Linking Macroscopic Stresses to Single-Crack Related Crack Propagation Criteria

In the following, we describe a link between the single-crack related crack propagation criteria of Section 2 and the macroscopic stresses Σ imposed as uniform boundary conditions on a microcracked RVE. This link allows for investigation of the influence of the propagation of single cracks on the progressive reduction of the effective stiffness of a material comprising numerous propagating cracks. The key to this link is that both micromechanics and fracture-mechanics rely on matrix-inclusion problems (Figs. 2.3 and 2.1) dealing with a single crack embedded in an infinite matrix subjected to remote uniform loading: Zaoui's concentration procedure [39, 40, 41] provides a relation between the macroscopic strains \mathbf{E} (Fig. 3.1b) acting on the boundary of the RVE of a damaged material with numerous microcracks and the strains \mathbf{E}^∞ (Fig. 2.3) imposed (at infinity) on a matrix surrounding a single microcrack:

$$\mathbf{E}^\infty = \left[f_m \mathbf{I} + f_c \frac{1}{\theta^*} \int_0^{\theta^*} \left(\mathbf{I} + \mathbb{S}_c^m [n(\theta)] \right)^{-1} d\theta \right]^{-1} : \mathbf{E} \quad (3.23)$$

as follows from specification of (3.13) for $\mathbf{C}_c = 0$. Setting the fictitious strains \mathbf{E}^∞ equal to the ones caused by Σ^∞ in the fracture mechanics problem of Fig. 2.1, i.e.

$$\mathbf{E}^\infty = \mathbf{C}_m^{-1} : \Sigma^\infty \quad (3.24)$$

establishes the aforementioned link between micromechanics and fracture-mechanics: (3.24), together with (3.23), allow for relating the remote stresses Σ^∞ “felt” by one single microcrack to the macroscopic strains \mathbf{E} prevailing on the RVE of the material with numerous microcracks. Additional consideration of (3.9) delivers the relation between Σ^∞ and the macroscopic stresses Σ acting on the RVE, reading, with $\mathbf{C}_{\text{hom}} = \mathbf{C}_{\text{hom}}^{(MT)}$ from (3.16), as

$$\Sigma^\infty = \frac{\Sigma}{f_m} = \frac{\Sigma}{1 - f_c} \quad (3.25)$$

Particularly, (3.25) provides the link between the RVE-related quantity Σ and the fracture-mechanics related quantity Σ^∞ , playing the governing role in the criteria for single-crack propagation (2.2)-(2.5), see also (2.17), (2.20), and (2.23).

4 Effective Stress-Strain Behavior of Microcracked Brittle Materials – Assessment of Griffith's Energy Release Rate Criterion

While the stiffness estimates (3.19) and (3.22) define the effective stress-strain behavior in the elastic regime, the link (3.25), together with single-crack related propagation criteria (2.2)-(2.4) mark the limit of this regime, and give access to the effective stress-strain behavior during stable mode-I-type propagation of the microcracks; i.e. during evolving damage of the material defined on the RVE. Thereby, they relate the macroscopic stress imposed on the RVE to the characteristics of the microcracks inside the RVE (i.e. α , c , and N).

Comparison of model predictions with the behavior of brittle materials observed in corresponding experiments will allow for assessing the performance of Griffith's energy release rate criterion in the framework of mode I type microcracking in brittle materials.

4.1 Uniaxial Macroscopic Tension – Tensile Mode I Micro-cracking

To study tensile microcracking, we consider a RVE (Fig. 3.1b) subjected to the macroscopic uniaxial tensile stress state

$$\Sigma = \Sigma_{33} e_3 \otimes e_3, \quad \Sigma_{33} > 0 \quad (4.1)$$

In order to represent the crack patterns observed in corresponding experiments [33, 34], we consider cracks of identical orientation with normals \mathbf{n} (Fig. 2.2) pointing in the direction of loading ($\mathbf{n} = \mathbf{e}_3$ in Fig. 3.1b). Consideration of sharp cracks ($c = 0$), as relevant approximation for slightly opened cracks under tensile mode-I-type loading (see (2.17) and discussion below), implies $f_c = 0$ [see (3.17)], and, hence, $\Sigma^\infty = \Sigma$ [see (3.25)]. Therefore, the expression of G_I for every single of the many microcracks embedded in the considered RVE follows from replacing Σ_{33}^∞ by Σ_{33} in (2.17), i.e.

$$G_I = \frac{4\Sigma_{33}^2 a}{\pi} \left(\frac{1 - \nu_m^2}{E_m} \right) \quad (4.2)$$

The relation (4.2), together with the crack propagation criteria (2.2)-(2.4), allows for testing whether or not macroscopic loading Σ_{33} on the RVE of the microcracked material leads to propagation of the individual microcracks in the material. If the criterion (2.2) is satisfied:

$$G_I = \frac{4\Sigma_{33}^2 a}{\pi} \left(\frac{1 - \nu_m^2}{E_m} \right) < G_c \quad (4.3)$$

the microcracks do not propagate, i.e. $\alpha = \alpha_{ini} = \text{const.}$, where α_{ini} denotes the initial radius of the penny-shaped cracks. The damaged material behaves linear elastically, according to the specification of (3.9) for (3.19) and (4.1)

$$\Sigma_{33} = E_m \left[1 + \frac{16}{3} N a^3 (1 - \nu_m^2) \right]^{-1} E_{33} \quad (4.4)$$

If, however, (2.3) and (2.4) are satisfied:

$$G_I = \frac{4\Sigma_{33}^2 a}{\pi} \left(\frac{1 - \nu_m^2}{E_m} \right) = G_c \quad (4.5)$$

the cracks propagate such that the crack radius increases ($d\alpha > 0$) while the equality (4.5) remains satisfied. This renders the uniaxial macroscopic stress Σ_{33} as a function of the crack radius α .

$$\Sigma_{33}(\alpha) = \sqrt{\frac{G_c E_m \pi}{4a(1 - \nu_m^2)}} \quad (4.6)$$

When assuming that $N = \text{const.}$ during crack propagation, the corresponding strain $E_{33} = E_{33}(\alpha)$ follows from substitution of (4.6) into the stress-strain relation (4.4),

$$E_{33}(\alpha) = \sqrt{\frac{G_c \pi}{4aE_m(1 - \nu_m^2)}} \left[1 + \frac{16}{3} N a^3 (1 - \nu_m^2) \right] \quad (4.7)$$

(4.6) and (4.7) describe stress-strain relations in parameter form, with the crack radius α as the parameter, see descending crack propagation paths in Fig. 4.1a and 4.2b.

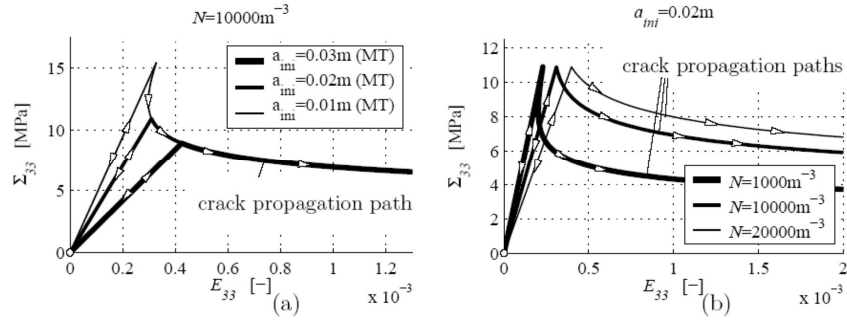


Fig. 4.1. Effective stress-strain behavior in uniaxial tension of a microcracked brittle material (Fig. 3.1b), predicted by combined fracture-micromechanics model on the basis of material constants of Silurian sedimentary rock (Table 4.1): (a) effect of initial crack radius a_{ini} and (b) effect of number of cracks per unit volume, N

Table 4.1. Material constants, uniaxial tensile strength, and uniaxial compressive strength of Silurian sedimentary rock [14]

E_m [GPa]	ν_m [-]	K_{Ic} [MPa \sqrt{m}]	G_c [J/m ²]	Σ_m [MPa]	$ \Sigma_{cu} $ [MPa]
49.4	0.24	1.74	57.76	13.6	158

(4.6) and (4.7) propose that materials *with the same number of differently sized* microcracks exhibit identical softening paths in the Σ_{33} - E_{33} space (Fig. 4.1a). However, the peak stresses (theoretical tensile strengths) of such materials decrease with increasing initial crack radius a_{ini} (Fig. 4.1a). On the other hand, materials *with different numbers of equally sized* microcracks exhibit identical peak stresses (Fig. 4.1b). Related softening paths are, however, the steeper the fewer cracks are contained in the RVE (Fig. 4.1b). Summarizing these results, effective strain-softening under uniaxial tension can be, at least qualitatively, predicted by a combined fracture micromechanics model based on Griffith's energy release rate criterion.

4.2 Uniaxial Macroscopic Compression – Axial Splitting

To study axial splitting, we consider a RVE subjected to the macroscopic uniaxial compressive stress state

$$\Sigma = \Sigma_{11} e_1 \otimes e_1, \quad \Sigma_{11} < 0 \quad (4.8)$$

In order to represent the crack patterns observed in corresponding experiments [35, 36, 37], we consider cracks with normals \mathbf{n} (Fig. 2.2) perpendicular to the direction of loading ($\mathbf{n}(\theta) \perp \mathbf{e}_1 \Leftrightarrow \theta \in [0, \pi]$ in Fig. 2.4), i.e. we introduce microcracks with orientations axisymmetrically distributed with respect to the axis of loading, the x_1 axis in Fig. 3.2. Opposed to the situation in Subsection 4.1, consideration of the crack opening ($c \neq 0$) is mandatory for appropriate determination of the energy release (see (2.20) and discussion below), even if the crack is only slightly opened. Accordingly, the released energy \mathcal{E} for every single of many axisymmetrically distributed microcracks embedded in the considered RVE follows from insertion of (3.25), relating Σ_{11}^∞ to $\Sigma_{11}/(1-f_c)$, into (2.19), yielding

$$\mathcal{E} = \frac{2\pi a^3 \Sigma_{11}^2}{3(1-f_c)^2 E_m} \left(\frac{c}{a} \right) + O\left(\frac{c}{a} \right)^2 \quad (4.9)$$

Calculation of G_I requires derivation of \mathcal{E} with respect to α [see (2.6)]. Thereby, the dependence of f_c on α [see (3.17)] must be taken into account, which yields

$$G_I = \frac{2a \Sigma_{11}^2}{3E_m} \left(\frac{c}{a} \right) + O\left(\frac{c}{a} \right)^2 \quad (4.10)$$

Since $c/\alpha \ll 1$, quadratic and higher-order terms in c/α may be neglected, rendering G_I as

$$G_I = \frac{2c \Sigma_{11}^2}{3E_m} \quad (4.11)$$

The relation (4.11), together with the crack propagation criteria (2.2)-(2.4), allows for testing whether or not macroscopic loading Σ_{11} on the RVE of the microcracked material leads to propagation of the individual microcracks in the material. If the criterion (2.2) is satisfied:

$$G_I = \frac{2c \Sigma_{11}^2}{3E_m} < G_c \quad (4.12)$$

the cracks do not propagate, i.e. $\alpha = \alpha_{ini} = \text{const.}$, and the damaged material behaves linear elastically, according to the specification of (3.9) for (3.22) and (4.8):

$$\Sigma_{11} = E_m \left(1 + \frac{4\pi}{3} N a^2 c \right)^{-1} E_{11} \quad (4.13)$$

If, however, (2.3) and (2.4) are satisfied:

$$G_I = \frac{2c\Sigma_{11}^2}{3E_m} = G_c \quad (4.14)$$

the cracks propagate such that the crack radius increases ($d\alpha > 0$) while the equality (4.14) remains satisfied. Since (4.14) does not depend on α , it follows that stable crack propagation (increase of α) requires a constant macroscopic stress: $\Sigma_{11} = \text{const.}$ (Fig. 4.2). This is a remarkable difference to macroscopic uniaxial tension where stable microcrack propagation requires a decreasing loading of the RVE (Figs. 4.1a and 4.1b). (4.14) delivers the macroscopic stress Σ_{11} associated to microcrack propagation as

$$\Sigma_{11}(a) = -\sqrt{\frac{3G_c E_m}{2c}} = \text{const.} \quad (4.15)$$

When assuming that $N = \text{const}$ during crack propagation, the corresponding strain $E_{11} = E_{11}(\alpha)$ follows from substitution of (4.15) into the stress-strain relation (4.13),

$$E_{11}(a) = -\sqrt{\frac{3G_c E_m}{2c}} \left(1 + \frac{4\pi N a^2 c}{3} \right) \quad (4.16)$$

(4.15) and (4.16) describe stress-strain relations in parameter form, with the crack radius α as the parameter. Related crack propagation paths yield a stress plateau in the Σ_{11} - E_{11} space (Fig. 4.2). Thereby, the absolute value of the bearable compressive stress increases with decreasing crack half opening width (Fig. 4.2). However, Griffith's energy release rate criterion does not predict strain-softening under uniaxial compression. In this line, the experimentally observed strain-softening behavior [36] would have to be caused by failure effects after the sample has split up into many slender "columns", i.e. by buckling and bending and/or tilting and sliding of these columns. Experimental observations of [38] foster this argumentation: The characteristic stress strain curve referring to unconfined axial compression shows, before the stress drop beyond the peak load, a region of almost vanishing inclination of the stress strain curve, i.e. a quasi-plateau, such as predicted by our model. In this region of the stress strain curve, a *large*

number of isolated fractures are formed, and fracturing clearly predominates along the direction of loading [38].

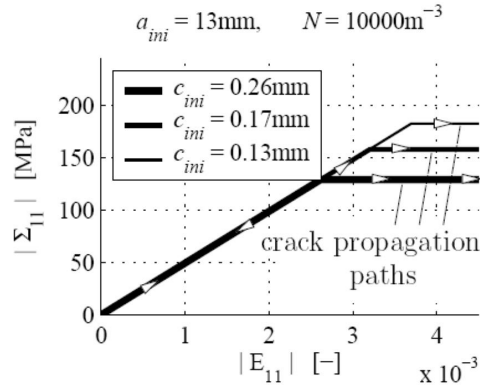


Fig. 4.2. Effective stress-strain behavior in uniaxial compression of a micro-cracked brittle material (Figs. 3.2b and 3.2c), predicted by combined fracture-micromechanics model on the basis of material constants of Silurian sedimentary rock (Table 4.1): effect of initial crack half opening width c_{ini}

4.3 Determination of the Initial Microcrack Radius and of the Initial Microcrack Half-Opening from the Uniaxial Tensile Strength and the Uniaxial Compressive Strength

By example of brittle Silurian sedimentary rock [14] (Table 4.1), experimentally determined uniaxial strength values in tension and compression, Σ_{tu} and Σ_{cu} , will be used for identification of the (initial) geometric properties of the microcracks: The initial crack radius a_{ini} follows from setting $\Sigma_{33} \equiv \Sigma_{tu}$ and in (4.5) and solving the resulting expression for a , yielding

$$a_{ini} = \frac{\pi E_m G_c}{4 \Sigma_{tu}^2 (1 - \nu_m^2)} = 12.86 \text{ mm} \quad (4.17)$$

according to the material constants listed in Table 4.1. The initial crack half-opening c_{ini} follows from setting the stress $\Sigma_{11} \equiv \Sigma_{cu}$ in (4.14) and solving the resulting expression for c , yielding

$$c_{ini} = \frac{3 E_m G_c}{2 \Sigma_{cu}^2} = 0.17 \text{ mm} \quad (4.18)$$

according to the material constants listed in Table 4.1. Remarkably, (4.17) and (4.18) imply that the ratio between the uniaxial compressive strength and the uniaxial tensile strength depends on the Poisson's ratio of the matrix and on the initial crack aspect ratio c_{ini}/a_{ini} (Fig. 4.3).

$$\frac{\Sigma_{cu}}{\Sigma_{tu}} = -\sqrt{\frac{6(1-\nu_m^2)}{\pi}} \left(\frac{c_{ini}}{a_{ini}} \right)^{-1} \quad (4.19)$$

This is a key result of the combined fracture-micromechanics approach of Subsection 3.5. According to (4.17) and (4.18), the Silurian sedimentary rock, described in [14], is characterized by an initial microcrack aspect ratio equal to $c_{ini}/a_{ini} = 1/75$.

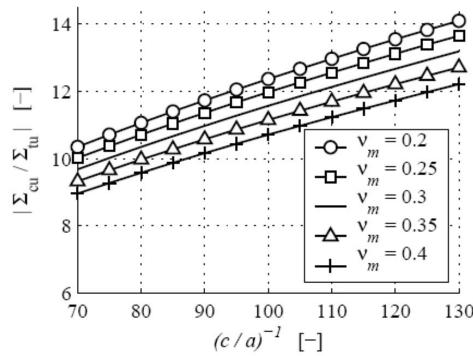


Fig. 4.3. Ratio between the uniaxial compressive strength Σ_{cu} and the uniaxial tensile strength Σ_{tu} as a function of the crack aspect ratio c/a and Poisson's ratio of the matrix, ν_m , predicted by the combined fracture-micromechanics approach

$c_{ini} = 0.17\text{mm}$ may appear as quite large, however, one should take into account that c_{ini} is the half opening of an *equivalent penny-shaped crack*. Real crack surfaces in rocks are not plane but have some kind of micro-roughness (Fig. 4.4), and the initial opening of real cracks might be well below 0.17mm . If such a crack is modeled by an equivalent (ideal) penny-shaped microcrack, the initial opening of the latter accounts for both the microroughness and the initial opening of the real crack (Fig. 4.4). Therefore, modeled crack openings are always larger than the real ones.

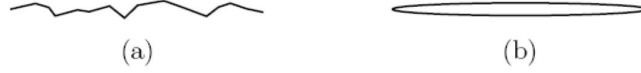


Fig. 4.4. Representation of (a) a realistic crack shape with microroughness by (b) an equivalent elliptic crack

4.4 Confined Macroscopic Compression – Axial Splitting

To study axial splitting under confined compression, we consider a RVE subjected to the macroscopic triaxial compressive stress state

$$\Sigma = \Sigma_{11}e_1 \otimes e_1 + \Sigma_{33}(e_2 \otimes e_2 + e_3 \otimes e_3), \quad \Sigma_{11} \leq 0, \quad \Sigma_{33} \leq 0 \quad (4.20)$$

where Σ_{11} is the predominant axial compressive stress and Σ_{33} is the lateral confinement pressure. In order to represent the crack patterns observed in corresponding experiments [35, 36, 37], we again consider cracks with axisymmetric orientation and non-vanishing crack half-opening widths, $c \neq 0$, as in Subsection 4.2 (Fig. 3.2). The released energy \mathcal{E} for every single of many axisymmetrically distributed microcracks embedded in the considered RVE follows from insertion of (3.25), relating Σ_{11}^∞ to $\Sigma_{11}/(1-f_c)$ and $\Sigma_{33}/(1-f_c)$, into (2.22), yielding

$$\begin{aligned} \mathcal{E} = & \frac{8a^3\Sigma_{33}^2}{3(1-f_c)^2} \frac{1-\nu_m^2}{E_m} + \frac{\pi a^3}{3} \left[\frac{\Sigma_{33}^2(1+\nu_m+4\nu_m^2-4\nu_m^3)}{E_m} + \right. \\ & \left. + \frac{2\Sigma_{11}^2-2\Sigma_{11}\Sigma_{33}(1+3\nu_m-2\nu_m^2)}{E_m(1-f_c)^2} \right] \left(\frac{c}{a} \right) + O\left(\frac{c}{a} \right)^2 \end{aligned} \quad (4.21)$$

Calculation of G_I requires derivation of \mathcal{E} with respect to a [see (2.6)]. Thereby, the dependence of f_c on a [see (3.17)] must be taken into account:

$$\begin{aligned} \mathcal{G} = & \frac{4\Sigma_{33}^2a}{\pi} \frac{1-\nu_m^2}{E_m} \left[1 + \frac{40\pi Na^3}{9} \left(\frac{c}{a} \right) \right] + \frac{a}{3} \left[\frac{\Sigma_{33}^2(1+\nu_m+4\nu_m^2-4\nu_m^3)}{E_m} + \right. \\ & \left. + \frac{2\Sigma_{11}^2-2\Sigma_{11}\Sigma_{33}(1+3\nu_m-2\nu_m^2)}{E_m} \right] \left(\frac{c}{a} \right) + O\left(\frac{c}{a} \right)^2 \end{aligned} \quad (4.22)$$

In order to assess whether or not Griffith's energy release rate criterion has the potential to satisfactorily predict material damage under confined

compression, it is useful to consider onset of microcracking, by inserting G_I from (4.22) into the condition (2.3), yielding

$$\begin{aligned} G = \frac{4\Sigma_{33}^2 a}{\pi} \frac{1-v_m^2}{E_m} \left[1 + \frac{40\pi N a^3}{9} \left(\frac{c}{a} \right) \right] + \frac{a}{3} \left[\frac{\Sigma_{33}^2 (1+v_m+4v_m^2-4v_m^3)}{E_m} + \right. \\ \left. + \frac{2\Sigma_{11}^2 - 2\Sigma_{11}\Sigma_{33}(1+3v_m-2v_m^2)}{E_m} \right] \left(\frac{c}{a} \right) = G_c \end{aligned} \quad (4.23)$$

when having neglected the higher-order terms $O(c/a)^2$ in (4.22). Solving (4.23) for Σ_{11} delivers the predominant axial compressive stress at onset of microcracking, denoted by Σ_{11}^{cr} , as a function of the lateral confinement pressure Σ_{33} .

$$\Sigma_{11}^{cr} = -\sqrt{\frac{3G_c E_m}{2a} - \frac{6\Sigma_{33}(1-v_m^2)}{\pi} \left(\frac{c}{a} \right)^{\frac{1}{2}} + \frac{\Sigma_{33}(1+3v_m-2v_m^2)}{2}} + O\left(\frac{c}{a} \right)^{\frac{1}{2}} \quad (4.24)$$

Evaluation of (4.24) for the material parameters of Table 4.1 and for α_{ini} and c_{ini} according to (4.17) and (4.18), proposes that an increase of lateral confinement pressure from zero up to 1% of Σ_{cu} increases the predominant axial compressive stress at onset of axial splitting, but only by less than 1% (Fig. 4.5). Further increase of the confinement pressure is predicted to *decrease* the predominant axial compressive stress at onset of axial splitting, which contradicts experimental findings.

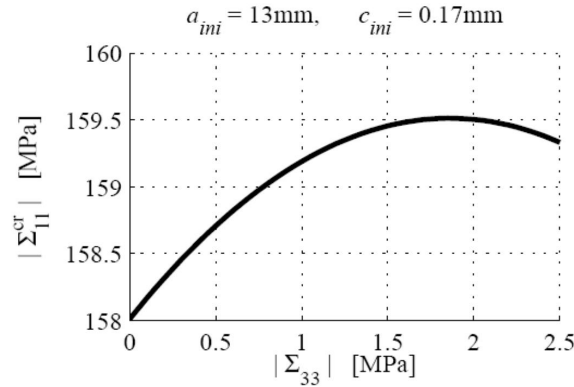


Fig. 4.5. Predominant axial compressive stress at onset of microcracking as a function of the lateral confinement pressure, predicted by combined fracture-micro-

mechanics model on the basis of material constants of Silurian sedimentary rock (Table 4.1)

This contradiction is due to the fact that we do not account for the sign of the microstress component σ_{zz} in the vicinity of the crack edge (Fig. 2.1). In case of uniaxial compression parallel to the crack plane, these stresses are tensile. If confinement stresses orthogonal to the crack plane are additionally applied, the initially tensile stresses σ_{zz} become compressive, already at very small confinement pressures. Consequently, crack propagation becomes impossible and (4.23) as well as (4.24) are no longer valid. Hence, the presented approach proposes that, under such confinements, brittle failure is not associated with mode I propagation of cracks in the direction of predominant compressive axial loading, but with propagation of closed, inclined cracks. This shear mode type of crack propagation, however, is not the topic of the present paper. Summarizing these results, Griffith's crack propagation criterion based on energy release rate is seen to be applicable also to compressive stress states, but it is mandatory to account for the sign of the normal stresses in the vicinity of the crack edge, acting in the crack normal direction.

5 Conclusions

The aim of this paper was to assess the potentials and the limitations of Griffith's energy release rate criterion to predict effective stress-strain behavior of brittle materials damaged by microcracks propagating in cracking mode I. For this purpose, Griffith's energy release rate criterion, related to a single penny-shaped crack embedded in an infinite matrix subjected to remote uniform stresses, was combined with stiffness estimates for RVEs of damaged (microcracked) materials taken from continuum micromechanics. As regards uniaxial tension, this combination allows for modeling macroscopic strain-softening as a result of propagation of microcracks, i.e. as a microstructural effect. Hence, Griffith's energy release rate criterion has the potential to predict, at least qualitatively, the behavior of microcracked materials under uniaxial tension. Thereby, the microcracks may be modeled as sharp cracks (as commonly introduced in fracture mechanics), since sharp cracks release (during tensile crack propagation) an amount of energy similar to that released by slightly opened cracks. As for uniaxial compression, however, the non-vanishing opening width of the microcracks must be taken into account, even though it is commonly by orders of magnitude smaller than the in-plane crack

diameter. There, the described combination of fracture and micromechanics proposes that macroscopic axial splitting under uniaxial compression is characterized by a constant stress level. Remarkably, the proposed model reveals that the ratio between the uniaxial tensile strength and the uniaxial compressive strength is a function of the crack aspect ratio, i.e. the ratio between the crack half-opening width and the crack radius. Therefore, the combined fracture-micromechanics approach accounts for the basic strength properties of brittle materials simply by introducing geometric properties of the microcracks within the RVE. However, Griffith's energy release rate criterion does not have the potential to predict effective strain-softening under uniaxial compression. The latter would have to be explained by buckling or tilting of slender columns after disintegration of the material. As a further limitation, Griffith's energy release rate criterion alone was found to be insufficient for prediction of axial splitting caused by confined compression: A complementary stress criterion accounting for the sign of the microstresses in the vicinity of the crack edge would be necessary.

References

1. Z.P. Bažant and J. Planas. *Fracture and Size Effect in Concrete and Other Quasibrittle Materials*. CRC Press, Boca Raton and London, 1998.
2. Y. Benveniste. A new approach to the application of Mori-Tanaka's theory in composite materials. *Mechanics of Materials*, 6(2):147{157, 1987.
3. Y. Benveniste, G.J. Dvorak, and T. Chen. On diagonal and elastic symmetry of the approximate effective stiffness tensor of heterogeneous media. *Journal of the Mechanics and Physics of Solids*, 39(7):927{946, 1991.
4. R.D. Bradshaw, F.T. Fisher, and L.C. Brinson. Fiber waviness in nanotube-reinforced polymer composites - ii: modeling via numerical approximation of the dilute strain concentration tensor. *Composites Science and Technology*, 63(11):1705-1722, 2003.
5. V. Deudé, L. Dormieux, D. Kondo, and S. Maghous. Micromechanical approach to nonlinear poroelasticity: application to cracked rock. *Journal of Engineering Mechanics (ASCE)*, 128(8):848{855, 2002.
6. L. Dormieux and D. Kondo. Approche micromécanique du couplage perméabilité-endommagement [Micromechanical approach to the coupling between permeability and damage]. *C. R. Mécanique*, 332(2):135{140, 2004. In French.
7. L. Dormieux and D. Kondo. Poroelasticity and damage theory for saturated cracked media. In L. Dormieux and F.-J. Ulm, editors, *Applied micromechanics of porous media*, volume 480 of *CISM Course and Lecture Notes*, pages 153-186. Springer Wien New York, 2005.

8. A.V. Dyskin. Self-similar crack patterns induced by spatial stress fluctuations. *Fatigue and Fracture of Engineering Materials and Structures*, 25(2):187-200, 2002.
9. J.D. Eshelby. The determination of the elastic field of an ellipsoidal inclusion, and related problems. *Proceedings of the Royal Society of London A*, 241:376-396, 1957.
10. A.G. Evans and Y. Fu. Some effects of microcracks on the mechanical properties of brittle solids - II. Microcrack toughening. *Acta Metallurgica*, 33(8):1515-1523, 1985.
11. F.T. Fisher, R.D. Bradshaw, and L.C. Brinson. Fiber waviness in nanotube-reinforced polymer composites - i: Modulus predictions using effective nanotube properties. *Composites Science and Technology*, 63(11):1689-1703, 2003.
12. A.A. Griffith. The phenomena of rupture and flow in solids. *Philosophical Transactions, Series A*, 221:163-198, 1920.
13. D. Gross and Th. Seelig. *Bruchmechanik mit einer Einführung in die Mikro-mechanik* [Fracture mechanics with an introduction to micromechanics]. Springer, Berlin, 3rd edition, 2001. In German.
14. K.L. Gunsallus and F.H. Kulhawy. A comparative evaluation of rock strength measures. *International Journal of Rock Mechanics and Mining Sciences*, 21(5):233-248, 1984.
15. Z. Hashin. Analysis of composite materials - a survey. *Journal of Applied Mechanics*, 50(3):481-505, 1983.
16. Z. Hashin. The differential scheme and its application to cracked materials. *Journal of the Mechanics and Physics of Solids*, 36(6):719-734, 1988.
17. R. Hill. Elastic properties of reinforced solids. *Journal of the Mechanics and Physics of Solids*, 11(5):357-372, 1963.
18. H. Horii and S. Nemat-Nasser. Overall moduli of solids with microcracks: load-induced anisotropy. *Journal of the Mechanics and Physics of Solids*, 31(2):155-171, 1983.
19. H. Horii and S. Nemat-Nasser. Brittle failure in compression: splitting, faulting and brittle-ductile transition. *Philosophical Transactions of the Royal Society of London, Series A*, 319:337-374, 1986.
20. J.W. Hutchinson. Crack tip shielding by micro-cracking in brittle solids. *Acta Metallurgica*, 35(7):1605-1619, 1987.
21. G.R. Irwin. Onset of fast crack propagation in high strength steel and aluminum alloys. *Segamore Research Conference Proceedings*, 2:289-305, 1956.
22. M. Kachanov. Effective elastic properties of cracked solids: critical review of some basic concepts. *Applied Mechanics Reviews (ASME)*, 45(8):304-335, 1992.
23. M. Kachanov and I. Sevostianov. On quantitative characterization of microstructures and effective properties. *International Journal of Solids and Structures*, 42(2):309-336, 2005.
24. N. Laws. On interfacial discontinuities in elastic composites. *Journal of Elasticity*, 5(3-4):227-335, 1975.

25. N. Laws. A note on penny-shaped cracks in transversely isotropic materials. *Mechanics of Materials*, 4(2):209-212, 1985.
26. N. Laws and G.J. Dvorak. The effect of fiber breaks and aligned penny-shaped cracks on the stiffness and energy release rates in unidirectional composites. *International Journal of Solids and Structures*, 23(9):1269-1283, 1987.
27. T. Mura. *Micromechanics of defects in solids*. Martinus Nijhoff Publishers, Dordrecht, 1987.
28. M. Ortiz. Microcrack coalescence and macroscopic crack growth initiation in brittle solids. *International Journal of Solids and Structures*, 24(3):231-250, 1988.
29. V. Pensée, D. Kondo, and L. Dormieux. Micromechanical analysis of anisotropic damage in brittle materials. *Journal of Engineering Mechanics (ASCE)*, 128(8):889-897, 2002.
30. J.R. Ponte Castañeda, P. Willis. The effect of spatial distribution on the effective behavior of composite materials and cracked media. *Journal of the Mechanics and Physics of Solids*, 43(12):1919-1951, 1995.
31. J. Salençon. *Handbook of Continuum Mechanics*. Springer Berlin Heidelberg, 2001.
32. V.P. Smyshlyaev and J.R. Willis. Effective relations for nonlinear dynamics of cracked solids. *Journal of the Mechanics and Physics of Solids*, 44(1):49-75, 1996.
33. J.G.M. van Mier and M.R.A. van Vliet. Uniaxial tension tests for the determination of fracture parameters of concrete: state of the art. *Engineering Fracture Mechanics*, 69(2):235-247, 2002.
34. J.G.M. van Mier and M.R.A. van Vliet. Influence of microstructure of concrete on size/scale effects in tensile fracture. *Engineering Fracture Mechanics*, 79(16):2281-2306, 2003.
35. M.R.A. van Vliet and J.G.M. van Mier. Experimental investigation of concrete fracture under uniaxial compression. *Mechanics of Cohesive-Frictional Materials*, 1:115-127, 1996.
36. J. Vardoulakis, J.F. Labuz, E. Papamichos, and J. Tronvoll. Continuum fracture mechanics of uniaxial compression on brittle materials. *International Journal of Solids and Structures*, 35(31-32):4313-4335, 1998.
37. E.Z. Wang and N.G. Shrive. Brittle fracture in compression: mechanisms, models, criteria. *Engineering Fracture Mechanics*, 52(6):1107-1126, 1995.
38. W.R. Wawersik and C. Fairhurst. A study of brittle rock fracture in laboratory compression experiments. *International Journal of Rock Mechanics and Mining Science & Geomechanics Abstract*, 7(5):561-575, 1970.
39. A. Zaoui. *Matériaux hétérogènes et composites [Heterogeneous materials and composites]*. Lecture Notes. Ecole Polytechnique, Paris, France, 1997. In French.
40. A. Zaoui. Structural morphology and constitutive behavior of microheterogeneous materials. In P. Suquet, editor, *Continuum Micromechanics*, pages 291-347, Wien, 1997. Springer.

41. A. Zaoui. Continuum micromechanics: Survey. Journal of Engineering Mechanics, ASCE, 128(8):808-816, 2002.

Modeling the Influence of Pressure and Moisture Content on the Disintegration of Weathered Rockfill Materials

E. Bauer¹, K. Kast², S.F. Tantono¹, W. Cen³

¹ Institute of Applied Mechanics,
Graz University of Technology,
Graz, Austria

² Consulting Geotechnical Engineering ICOLD,
Germany

³ Institute of Hydraulic Engineering,
Hohai University,
Nanjing,
P.R. China

Summary

In this paper the essential mechanical behavior of rockfill materials is modeled using a hypoplastic continuum approach. Critical states are included in the model for large shearing. With respect to a pressure dependent relative density the model can capture the essential mechanical properties of initially loose and dense granular materials with a single set of constants. While the calibration and application of hypoplastic models has already been extensively investigated for fine-grained materials like sand and powders, the present application to weathered rockfill materials is a first attempt to describe coarse-grained materials with a low and decreasing grain hardness. Particular attention is paid to modeling the influence of the initial density, the pressure and the moisture content of weathered broken rock on the incremental stiffness. An increase of the compressibility and a decrease of the limit void ratios with an increase of the moisture content of the grains is modeled in a simplified manner using only a moisture dependent granular hardness. The comparison of the numerical simulations of isotropic compression tests and triaxial compression test with experiments shows that the model captures the essential properties of weathered rockfill materials for both dry and water saturated grains. The

possibility of spontaneous shear band bifurcation under plane strain compression is analyzed and discussed for different initial densities.

1 Introduction

The mechanical behavior of rockfill materials is mainly determined by the grain hardness, the grain shape, the grain size distribution, the packing density, the orientation of contact planes, the stress state and the loading history. Stiffness and shear strength are influenced by the pressure level, the packing density and the rate of deformation and are therefore not material constants, e.g. [12]. The mechanical behavior of broken rock is different for unweathered or weathered grains. The degree of geological disintegration, i.e. by chemical weathering or by the intensity and the orientation of micro-cracks, has a significant influence on the granular hardness and as a consequence on the evolution of grain abrasion, grain breakage and grain size distribution. Depending on the state of weathering the propagation of micro-cracks due to water-induced stress corrosion can be strongly influenced by the moisture content of the grains [24]. Under higher stress levels the disintegration of grains can be accelerated by moisture, which leads to a reduction of the resistance to compaction and shearing [19, 20, 23].

The focus of the present paper is on modeling the mechanical behavior of broken rock materials using a hypoplastic continuum approach. In hypoplasticity the evolution equation for the stress tensor is formulated with a nonlinear isotropic tensor-valued function depending on the current state quantities and the rate of deformation. Unlike the classical concept of elasto-plasticity no decomposition of the deformation into elastic and plastic parts is needed in hypoplasticity [13, 21]. In order to model inelastic material properties the rate of deformation tensor is incorporated in the constitutive equation in a nonlinear formulation. With a pressure dependent density factor the influence of pressure and density on the incremental stiffness, the peak friction angle and the dilatancy can be modeled for an initially loose or dense state using a single set of constants [2, 15, 33, 34]. Limit states or so-called critical states are included in the constitutive equation for a simultaneous vanishing of the stress rate and volume strain rate. Originally hypoplastic material models were developed and calibrated for dry and cohesionless granular materials like sand. A comprehensive historical review can be found for instance in Wu and Kolymbas [37], Bauer and Herle [6].

While in the hypoplastic model by Gudehus [15] and Bauer [2] for granular materials with unweathered grains the so-called granular hardness is assumed to be constant, an extension of this version with a granular hardness depending on the moisture content is discussed for applications to weathered broken rock materials in the present paper. Herein the granular hardness is related to the grain assembly in the sense of a continuum description and does not mean the hardness of an individual grain. It is demonstrated that with the moisture content as an additional state variable the extended model captures the essential properties of weathered rockfill materials with a single set of constants for both dry and moisture grains. The model is calibrated for a weathered broken granite and the results obtained from the numerical simulation of element tests are compared with experiments. Finally the possibility of a spontaneous shear band bifurcation under plane strain compression is analyzed for different initial densities and for dry and wet conditions.

Throughout the paper compression stresses and strains are defined as negative. Bold lower case, bold upper case and calligraphic letters denote vectors, tensors of second order and of fourth order, respectively. In particular, the identity tensor of second order is denoted by \mathbf{I} and the identity tensor of fourth order is denoted by \mathcal{I} . For vector and tensor components indices notation with respect to a rectangular Cartesian basis \mathbf{e}_i ($i = 1, 2, 3$) is used. Operations and symbols are defined as: $\mathbf{ab} = a_i b_i$, $\mathbf{Ab} = A_{ij} b_j \mathbf{e}_i$, $\mathbf{a} \otimes \mathbf{b} = a_i b_j \mathbf{e}_i \otimes \mathbf{e}_j$, $\mathbf{I} = \delta_{ij} \mathbf{e}_i \otimes \mathbf{e}_j$, $\mathcal{I} = \delta_{ik} \delta_{jl} \mathbf{e}_i \otimes \mathbf{e}_j \otimes \mathbf{e}_k \otimes \mathbf{e}_l$, $\mathbf{A} \otimes \mathbf{B} = A_{ij} B_{kl} \mathbf{e}_i \otimes \mathbf{e}_j \otimes \mathbf{e}_k \otimes \mathbf{e}_l$, $\mathbf{AB} = A_{ik} B_{kj} \mathbf{e}_i \otimes \mathbf{e}_j$, $\mathbf{I} : \mathbf{A} = A_{ii}$, and $\mathcal{A} : \mathbf{B} = A_{ijkl} B_{kl} \mathbf{e}_i \otimes \mathbf{e}_j$. Herein δ_{ik} denotes the Kronecker delta and the summation convention over repeated indices is employed. A superimposed dot indicates a time derivatives, i.e. $\dot{\mathbf{A}} = d\mathbf{A}/dt$, and the symbol $[[\mathbf{A}]]$ denotes the jump of the field quantity \mathbf{A} at the discontinuity.

2 Granular Hardness and Pressure Dependent Limit Void Ratios

It is experimentally evident that for weathered rockfill materials the compressibility is higher for a wet than for a dry material as illustrated in Fig. (2.1). For a pre-compressed material under dry conditions (path A-B) a following wetting leads to an additional settlement along the path B-C. For a continuing loading the load-displacement curve (path C-D) follows the curve A-D obtained for an initially wet material, i.e. the memory of the

material of the pre-compaction under dry conditions is swept out if the load-displacement curve obtained for the wet material (path A-D) starts from the same initial density. In this context it is important to note that for different initial densities the compression curves are different for both dry and wet states of the material [20].

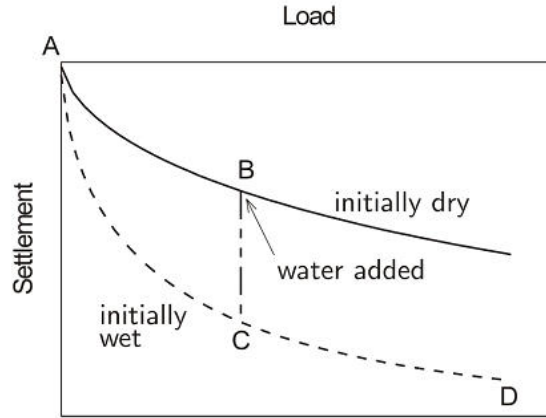


Fig. 2.1. Compression behavior of weathered broken rock in dry and wet states

In the following the compression behavior is first discussed for a dry granular material and modeled using a relation between the void ratio e and the mean pressure $p = -\mathbf{I} : \mathbf{T}/3$ where \mathbf{T} denotes the Cauchy stress tensor. The evaluation of numerous tests has shown that the compression behavior of various cohesionless materials can be approximated with the following exponential function [1]:

$$e = e_0 \exp \left[- \left(\frac{3p}{h_s} \right)^n \right]. \quad (2.1)$$

Herein the constant e_0 denotes the void ratio for $p \approx 0$, h_s has the dimension of stress and n is a dimensionless constant. The quantity of h_s is called granular hardness [15] which is related to the grain aggregate under isotropic compression and different from the hardness of an individual grain. Experimental investigations show that the quantity of h_s reflects the isotropic pressure where grain crushing becomes dominant.

More precisely, h_s represents the isotropic pressure $3p$ at which the compression curve in a semi-logarithmic representation shows the point of inflection while the exponent n is related to the inclination of the corresponding tangent (Figure 2.2a). For high pressures the void ratio in Eq. (2.1) tends to zero, which can be explained by grain plastification and grain crushing. Relation (2.1) is consistent within a very wide pressure range with the exception of states $p \rightarrow \infty$, which are characterized by a phase transition of the material.

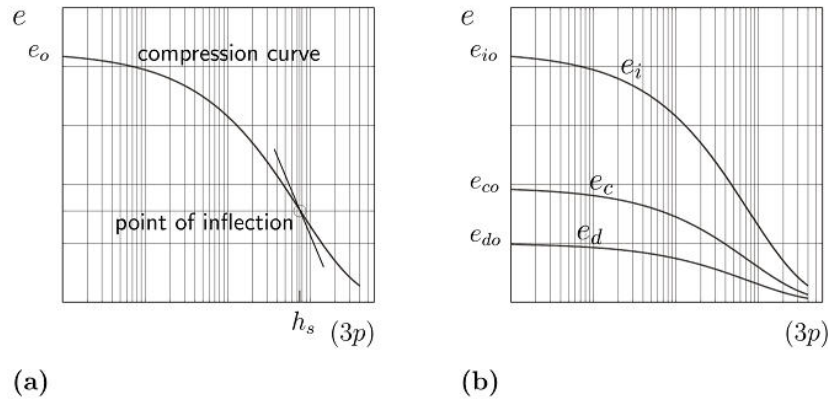


Fig. 2.2. (a) Isotropic compression relation (1) in a semi-logarithmic representation, (b) Pressure dependence of the maximum void ratio e_i , minimum void ratio e_d and critical void ratio e_c

For the evolution of the current void ratio e the assumption is made that the volume change of the solid material can be neglected. To this end, the rate of the void ratio can be directly derived from the mass balance, which yields:

$$\dot{e} = (1 + e) \mathbf{I} : \mathbf{D}. \quad (2.2)$$

Herein the rate of deformation \mathbf{D} is defined as the symmetric part of the velocity gradient of the grain skeleton. It can be noted that relation (2) is not restricted to granular materials with permanent rigid grains because the requirement of a constant solid volume is also fulfilled for a volume constant deformation of individual grains, grain crushing and abrasion.

Under the same pressure cohesionless granular materials can show different packing densities of the grain assembly so that the void ratio can range between a maximum void ratio e_i and a minimum void ratio e_d . In order to represent the range of possible void ratios for a given granular material it is convenient to consider the so-called phase diagram of grain skeletons [16] as sketched in Figure (2.2b). Herein the limit void ratios e_i and e_d are pressure dependent and they decrease with an increase of the mean pressure p . The upper bound, e_i , can be related to an isotropic compression starting from the loosest possible skeleton with grain contacts, i.e. there exists no homogeneous deformation which goes beyond $e = e_i$. Values of e_d will be achieved by cyclic shearing with very low amplitudes and nearly fixed mean pressure. By contrast, large monotonic shearing leads to a stationary state, which is characterized by a constant stress and constant void ratio. The void ratio in such a limit state, which is called critical void ratio, e_c , is not a material constant. Experimental observations with sand specimens (e.g. [8]) indicate that the critical void ratio decreases with the pressure p . It was suggested by Gudehus [15] to postulate that the maximum void ratio e_i , the minimum void ratio e_d and the critical void ratio e_c decrease with the mean pressure according to

$$\frac{e_i}{e_{io}} = \frac{e_d}{e_{do}} = \frac{e_c}{e_{co}} = \exp \left[- \left(\frac{3p}{h_s} \right)^n \right], \quad (2.3)$$

where e_{io} , e_{do} , and e_{co} are the corresponding values for $p \approx 0$ as shown in Figure (2.2b).

In order to model the influence of disintegration of a stressed rockfill by a reaction with water a degradation of the granular hardness with an increase of the moisture content ω of the solid material is assumed in the following. To this end the constant granular hardness h_s in Eq.(2.3) is replaced by the moisture dependent quantity h_s^* , i.e. [7]

$$h_s^* = h_{so} \psi(\omega). \quad (2.4)$$

Herein h_{so} is the value of the granular hardness obtained for the dry material, i.e. h_{so} is related to $\psi = 1$, and $\psi(\omega) \leq 1$ denotes the disintegration factor depending on the moisture content ω of the grain

material. A lower value of h_s^* means a higher compressibility of the material as illustrated in Fig. (2.3a).

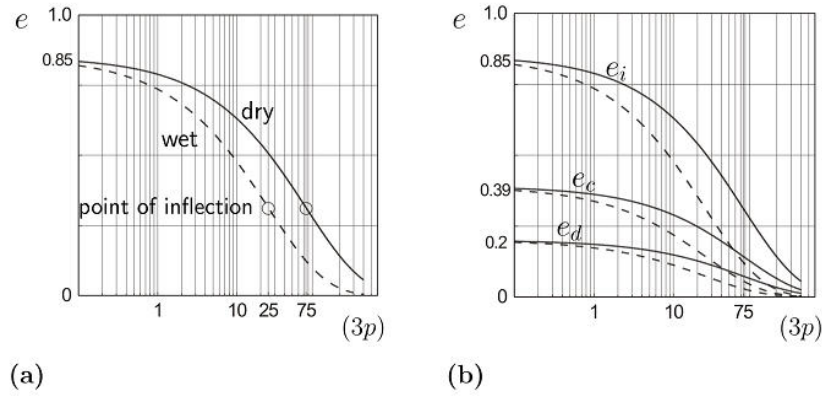


Fig. 2.3. Influence of the moisture content (solid curves: dry state, dashed curve: wet state) on **(a)** compression behavior, **(b)** limit void ratios

A specific representation of the scalar function $\psi(\omega)$ can be obtained by curve fitting experimental data. Due to the lack of experimental data for states with intermediary moisture contents, only a distinction between the granular hardness in the dry and the water-saturated state will be considered in the present paper. Then the disintegration factor $\psi(\omega)$ can be obtained by comparing the compression behavior for the dry material with the water saturated material using the compression relation (2.3) for the maximum void ratio e_i , i.e. $\psi(\omega)=1$ for the dry state and the value obtained for the water-saturated state must be $\psi(\omega) \leq 1$. It is obvious that with a degradation of the granular hardness according to relation (2.4) the pressure dependent limit void ratios and the critical void ratio obtained from relation (2.3) are lower for $\psi(\omega) \leq 1$ as illustrated in Fig. (2.3b).

3 Hypoplastic Model

3.1 Inelastic Material Properties

In hypoplasticity inelastic material properties are modeled with a constitutive equation of the rate type where the objective stress rate $\dot{\mathbf{T}}$ is expressed by an isotropic tensor-valued function consisting of the sum of the tensor function $\mathcal{A}:\mathbf{D}$, which is linear in the rate of deformation \mathbf{D} , and the tensor function $\mathbf{B}\sqrt{\mathbf{D}:\mathbf{D}}$, which is nonlinear in \mathbf{D} , i.e.

$$\dot{\mathbf{T}} = \mathcal{A}:\mathbf{D} + \mathbf{B}\sqrt{\mathbf{D}:\mathbf{D}} \quad (3.1)$$

Herein \mathcal{A} and \mathbf{B} are tensor-valued functions of the fourth order and second order, respectively. In the simplest case \mathcal{A} and \mathbf{B} only depend on the current Cauchy stress tensor \mathbf{T} , i.e. $\mathcal{A} = \mathcal{A}(\mathbf{T})$ and $\mathbf{B} = \mathbf{B}(\mathbf{T})$, but for a refined modeling of the material behavior it may also depend on additional state quantities as outlined in the following sections. The constitutive equation (3.1) is positively homogeneous of the first order in \mathbf{D} , thus the material behavior to be described is rate independent. With the nonlinearity in \mathbf{D} an inelastic material behavior is modeled in hypoplasticity with a single constitutive equation and there is no need to distinguish between elastic and plastic parts of the deformation explicitly [21]. Limit states are included in the constitutive equation for states in which $\mathbf{D} \neq 0$ and $\dot{\mathbf{T}} = 0$. In particular for a vanishing stress rate $\dot{\mathbf{T}}$ it follows from the constitutive equation (3.1) that \mathbf{T} and \mathbf{D} in the limit state satisfy the relation

$$\mathcal{A}:\mathbf{D} + \mathbf{B}\sqrt{\mathbf{D}:\mathbf{D}} = 0. \quad (3.2)$$

The normalized rate of deformation, $\hat{\mathbf{D}}$, can be obtained from Eq.(3.2) to:

$$\hat{\mathbf{D}} = \frac{\mathbf{D}}{\sqrt{\mathbf{D}:\mathbf{D}}} = -\mathcal{A}^{-1}:\mathbf{B}. \quad (3.3)$$

Inserting Eq.(3.3) into the identity $\hat{\mathbf{D}}:\hat{\mathbf{D}} = 1$ leads to the stress limit condition [10]:

$$(\mathcal{A}^{-1}:\mathbf{B}):(\mathcal{A}^{-1}:\mathbf{B}) - 1 = 0 \quad (3.4)$$

The set of all stresses which fulfill this condition can be represented by a surface in the stress space which is called limit stress surface, e.g. [35]. It

is worth noting that Eq.(3.4) first fulfills only the requirement for a vanishing stress rate and it is only related to critical stress states if the second requirement for a vanishing volume strain rate is also fulfilled, i.e.

$$\mathbf{I} : \hat{\mathbf{D}} = \mathbf{I} : (\mathcal{A}^{-1} : \mathbf{B}) = 0. \quad (3.5)$$

In order to model critical states for any deviatoric stress direction Eqs. (3.4) and (3.5) are necessary conditions for specific representations of \mathcal{A} and \mathbf{B} as firstly discussed by Bauer [1] and von Wolffersdorff [30]. Furthermore in a stationary state the right-hand side of Eq. (3.3) must be homogeneous of degree zero in \mathbf{T} , otherwise the critical stress ratio would not be invariant with regard to the stress level.

3.2 Density, Pressure and Moisture Dependent Properties

In order to take into account the influence of the density, the pressure and the disintegration of the granular hardness on the incremental stiffness the state quantities of the tensor functions \mathcal{A} and \mathbf{B} of the constitutive Eq. (3.1) are extended with the current void ratio e and the moisture dependent granular hardness h_s^* , i.e. $\mathcal{A} = \mathcal{A}(e, h_s^*, p, \mathbf{T})$ and $\mathbf{B} = \mathbf{B}(e, h_s^*, p, \mathbf{T})$. Herein the mean pressure is defined as $p = -\mathbf{I} : \mathbf{T}/3$. To specify these tensor functions a factorized representation is used in a way similar to those proposed by Gudehus [15] and Bauer [2]. In particular with $\mathcal{A} = f_s(e, h_s^*, p) \mathcal{L}(\hat{\mathbf{T}})$ and $\mathbf{B} = f_s(e, h_s^*, p) f_d(e, h_s^*, p) \mathbf{N}(\hat{\mathbf{T}})$ the extended constitutive equation can be written as:

$$\dot{\mathbf{T}} = f_s(e, h_s^*, p) \left[\mathcal{L}(\hat{\mathbf{T}}) : \mathbf{D} + f_d(e, h_s^*, p) \mathbf{N}(\hat{\mathbf{T}}) \sqrt{\mathbf{D} : \mathbf{D}} \right] \quad (3.6)$$

In Eq. (10) the scalar factors f_s and f_d are called stiffness factor and density factor, respectively. The fourth order tensor $\mathcal{L}(\hat{\mathbf{T}})$ and the second order tensor $\mathbf{N}(\hat{\mathbf{T}})$ are isotropic tensor-valued functions of the normalized stress tensor $\hat{\mathbf{T}} = \mathbf{T}/(\mathbf{I} : \mathbf{T})$ and the corresponding deviatoric part $\hat{\mathbf{T}}^* = \hat{\mathbf{T}} - \mathbf{I}/3$. The requirements (3.4) and (3.5) for modeling critical states are satisfied for the following specific functions [5]:

$$\mathcal{L}(\hat{\mathbf{T}}) = \hat{a}^2 \mathcal{I} + \hat{\mathbf{T}} \otimes \hat{\mathbf{T}}, \quad (3.7)$$

$$\mathbf{N}(\hat{\mathbf{T}}) = \hat{a}^2 (\hat{\mathbf{T}} + \hat{\mathbf{T}}^*). \quad (3.8)$$

$$f_s = \left(\frac{e_i}{e} \right)^\beta \frac{1}{\hat{\mathbf{T}} : \hat{\mathbf{T}}} f_b, \quad (3.9)$$

$$f_d = \left(\frac{e - e_d}{e_c - e_d} \right)^\alpha. \quad (3.10)$$

Herein \hat{a} is related to the stress limit condition in critical states as outlined later on and $\alpha < 0.5$ and $\beta > 1$ are constitutive constants. In relations (3.9) and (3.10) the current void ratio e is related to the maximum void ratio e_i , the minimum void ratio e_d and the critical void ratio e_c . According to the relations (2.3) and (2.4) the quantities e_i , e_d and e_c decrease with the mean pressure p and they are lower for a smaller granular hardness h_s^* (Fig. 2.3b). Factor f_s models the influence of the pressure, density and granular hardness on the incremental stiffness while factor f_d triggers the dilatancy behavior and the peak friction angle. Under shearing a stress peak is defined for a vanishing stress rate and for $f_d \neq 1$. A closer inspection shows that for an initially dense material, i.e. $e < e_c$ and $f_d < 1$, the part $f_d(e, h_s^*, p) \mathbf{N}(\hat{\mathbf{T}}) \|\mathbf{D}\|$ in (3.6) decreases and a higher peak friction angle is obtained. As a consequence of dilatancy the void ratio increases after the peak and it tends towards the critical void ratio e_c . Shearing of an initially loose material, i.e. $e > e_c$ and consequently $f_d > 1$, leads a densification towards the critical void ratio, but no stress peak appears. In a critical state, $e = e_c$, the value of the density factor $f_d = 1$ and it is independent of the initial void ratio, the pressure level and the granular hardness. It can be proved that for unlimited monotonic shearing a stationary stress state \mathbf{T}_c and void ratio e_c is reached asymptotically both for an initially dense and for an initially loose state [1]. By substituting the conditions for critical states, i.e. $\dot{\mathbf{T}}_c = 0$, $\dot{\mathbf{e}}_c = \mathbf{I} : \mathbf{D}_c = 0$ and $f_d = 1$, into the constitutive equation (3.6) the following relation for the stress limit condition in critical states is obtained [1,5]:

$$\hat{a}_c - \sqrt{\hat{\mathbf{T}}_c^* : \hat{\mathbf{T}}_c^*} = 0. \quad (3.11)$$

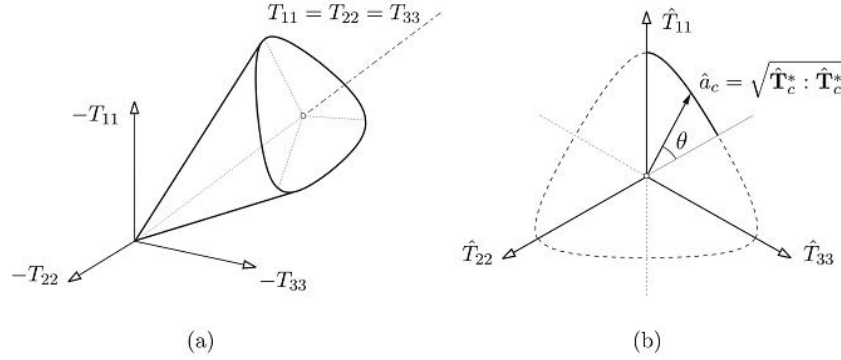


Fig. 3.1. (a) Critical stress surface in the space of principal stress component, (b) contour of the stress limit condition in the π -plane

By substituting the identity $\hat{\mathbf{T}}_c^* = \hat{\mathbf{T}} - \mathbf{I}/3$ into (3.11) it is obvious that in the space of principal stress components the stress limit condition represents a conical surface with its apex at the origin of the stress space (Fig. 3.1a). The scalar \hat{a}_c in (3.11) can be interpreted as the radius of the trace of the critical stress surface in the π -plane, i.e. \hat{a}_c is equal to the Euclidean norm of the normalized stress deviator (Fig. 3.1b). Apparently the size and shape of the critical stress surface is fully determined by factor \hat{a} of the constitutive equation. By choosing suitable representations for \hat{a} the reproduction of various conical limit surfaces is possible without loss of the general form of the constitutive equation (3.6) as outlined in detail by Bauer [5]. In the present paper the stress limit condition given by Matsuoka and Nakai [22] is considered, which can be modeled by factor \hat{a} as:

$$\hat{a} = \frac{\sin \varphi}{3 - \sin \varphi} \left[\sqrt{b} - \sqrt{\hat{\mathbf{T}}^* : \hat{\mathbf{T}}^*} \right], \quad (3.12)$$

$$\text{with } b = \frac{(8/3) - 3(\hat{\mathbf{T}}^* : \hat{\mathbf{T}}^*) + \sqrt{3/2}(\hat{\mathbf{T}}^* : \hat{\mathbf{T}}^*)^{3/2} \cos(3\theta)}{1 + \sqrt{3/2}(\hat{\mathbf{T}}^* : \hat{\mathbf{T}}^*)^{1/2} \cos(3\theta)}.$$

Herein φ denotes the critical friction angle and θ is the Lode-angle, which is defined as:

$$\cos(3\theta) = -\sqrt{6} \frac{\mathbf{I} : \hat{\mathbf{T}}^{*3}}{[\mathbf{I} : \hat{\mathbf{T}}^{*2}]^{3/2}}. \quad (3.13)$$

Since \hat{a} is embedded in the constitutive equation (3.6) it is always effective and only for cases where $\hat{\mathbf{T}}^* = \hat{\mathbf{T}}_c^*$ the value of \hat{a} obtained from Eq. (3.12) is equal to the limit condition given by Matsuoka and Nakai, i.e. $\hat{a}(\hat{\mathbf{T}}^* = \hat{\mathbf{T}}_c^*) = \hat{a}_c = \sqrt{\hat{\mathbf{T}}_c^* : \hat{\mathbf{T}}_c^*}$.

In order to link Eq. (3.6) with Eq. (2.1) it was postulated by Gudehus [15] that the response of the constitutive equation (3.6) for an isotropic compression starting from the loosest state, i.e. $e = e_{io}$, must coincide with the proposed compression law (2.1). This condition permits the direct determination of factor f_b in (3.9), yielding:

$$f_b = \frac{h_s^*}{n h_i} \frac{1 + e_i}{e_i} \left(\frac{3p}{h_s^*} \right)^{1-n}, \quad (3.14)$$

with $h_i = \frac{8 \sin^2 \varphi}{(3 - \sin \varphi)^2} + 1 - \frac{2\sqrt{2} \sin \varphi}{3 - \sin \varphi} \left(\frac{e_{io} - e_{do}}{e_{co} - e_{do}} \right)^\alpha$.

It follows from relation (3.14) that the stiffness factor f_s in (3.9) is proportional to the moisture dependent granular hardness h_s^* . Therefore the moisture content of the solid material is not only taken into account for the isotropic compression behavior and the pressure dependent limit void ratios in relation (2.3), it generally influences the incremental stiffness modeled by the constitutive equation (3.6).

The present hypoplastic model for cohesionless granular materials includes 9 constants which can be determined from simple index and element tests [2, 18]. In particular h_{so} and n can be determined from the compression behavior of the dry material, ψ depends on the moisture content ω . The quantities φ and e_{co} are related to the critical state in triaxial compression, α and β depend on the peak friction angle, and e_{io} and e_{do} are the limit void ratios for a nearly stress free state. Since the current void ratio e is related to the pressure dependent limit void ratios by the functions f_s and f_d , the constitutive constants are not restricted to a certain initial density. In the present paper the calibration of the constants is based on the experiments carried out by Kast [20] with weathered

broken granite. The following values were obtained: $\varphi = 42^\circ$, $h_{so} = 75 \text{ MPa}$, $\psi = 1$ for dry states and $\psi = 0.34$ for the water saturated state of the solid material, $n = 0.6$, $e_{io} = 0.85$, $e_{co} = 0.39$, $e_{do} = 0.2$, $\alpha = 0.125$ and $\beta = 1.05$. It should be noted that in the present model the critical friction angle φ is assumed to be a constant because the experiments used for the present calibration did not show a clear influence of the moisture content on the critical friction angle.

3.3 Comparison of Numerical Simulations with Experiments

The results obtained from the numerical simulation of homogeneous element tests are compared with experiments carried out by Kast [20] for isotropic compression (Fig. 3.2) and triaxial compression (Fig. 3.3 and Fig. 3.4). Under isotropic compression starting from an initial void ratio of $e_0 = 0.46$ the densification is significantly higher for the water-saturated state of the solid material (Fig. 3.2b) than for the dry state (Fig. 3.2a).

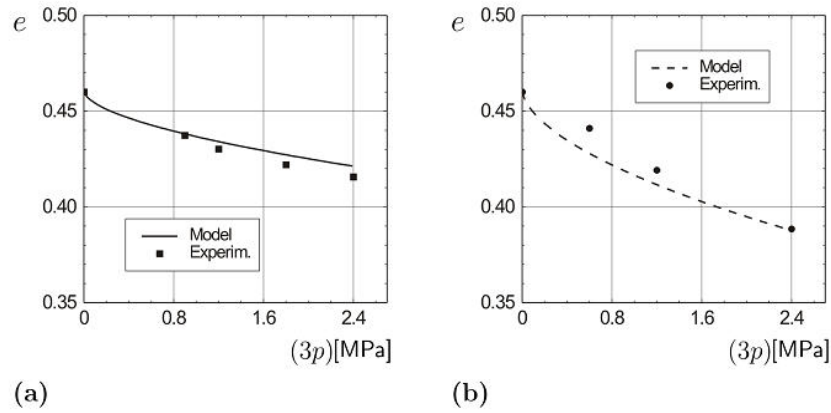


Fig. 3.2. Isotropic compression starting from an initial void ratio of $e_0 = 0.46$: (a) dry state ($\psi = 1$), (b) saturated state ($\psi = 0.34$)

For a mean pressure of $p = 0.8 \text{ MPa}$ the corresponding void ratios are $e = 0.418$ for the dry material and $e = 0.378$ for the saturated solid material. These are the initial states for the triaxial compression under a

constant mean pressure of $p = 0.8 \text{ MPa}$ as shown in Fig.(3.3). As the initial void ratio is higher than the corresponding pressure dependent critical one, i.e. for $p = 0.8 \text{ MPa} \rightarrow e_c = 0.34$ for the dry material and $e_c = 0.31$ for the saturated material, the triaxial compression leads to a further densification for both the dry material and the saturated material.

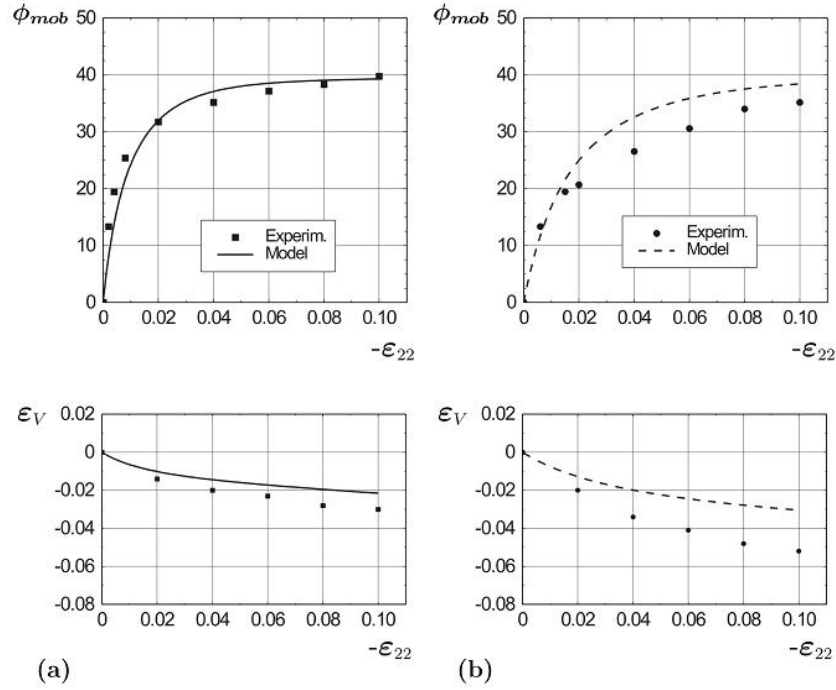


Fig. 3.3. Triaxial compression under constant mean pressure starting from an initial void ratio of: (a) $e_0 = 0.418$ for the dry state ($\psi = 1$), (b) $e_0 = 0.387$ for the saturated state ($\psi = 0.34$)

The increase of the mobilized friction angle ϕ_{mob} with the vertical strain ϵ_{22} is more pronounced for the dry material (Fig. 3.3a) than for the saturated one (Fig. 3.3b), which is also in agreement with the experiments. In order to study the influence of an initially dense material the experiments for triaxial compression under a constant mean pressure of $p = 0.8 \text{ MPa}$

starting from $e = 0.29$ for the dry material and $e = 0.285$ for the saturated solid material are compared with the prediction of the hypoplastic model in Fig.(3.4).

A comparison of Fig. (3.3) with Fig. (3.4) shows that the volume-strain behavior is strongly influenced by the initial density and it differs for the dry and saturated states of the solid material. The additional densification is less pronounced and the maximum mobilized friction angle is higher for the initially dense material. A clear peak state for ϕ_{mob} can only be detected for the dry and initially dense material (Fig. 3.4a). After the peak the value of ϕ_{mob} slightly decreases with advanced vertical compression and it is accompanied by dilatancy. For the saturated and initially dense state of the material the dilatancy is less pronounced.

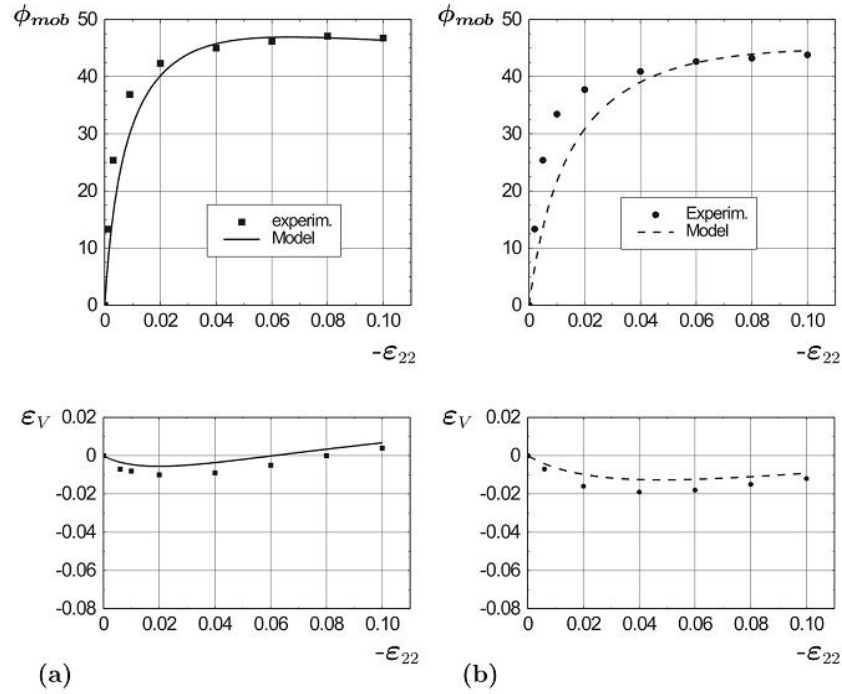


Fig. 3.4. Triaxial compression under constant mean pressure starting from an initial void ratio of: (a) $e_0 = 0.29$ for the dry state ($\psi = 1$), (b) $e_0 = 0.285$ for the saturated state ($\psi = 0.34$)

4 Shear Band Analysis or Plane Strain Compression

In this section the possibility of a spontaneous shear band formation under plane strain compression at a constant lateral pressure is studied. Of particular interest is the influence of the density, pressure level and granular hardness on the lowest stress ratio and the inclination angle of the shear band at the onset of shear band formation. The present investigation is based on the general bifurcation theory [17, 25, 26, 29]. The bifurcation condition is derived in a way similar to the ones outlined for hypoplastic models in earlier publications (e.g. [3, 4, 9, 10, 11, 14, 31, 32, 36]). A comprehensive historical review of the individual contributions can be found for instance in Tamagnini et al. [27, 28].

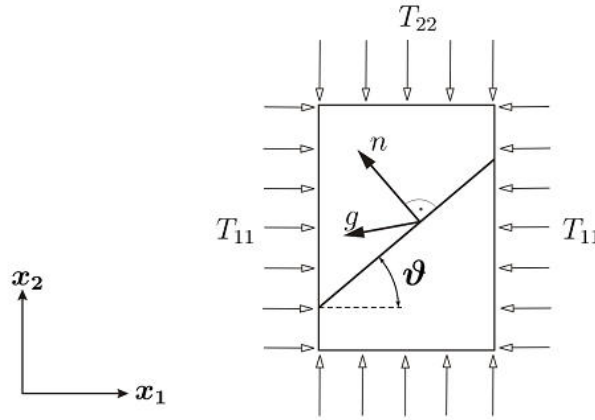


Fig. 4.1. Orientation ϑ of the shear band under plane strain compression

In the following the possibility of a spontaneous formation of a shear band is studied for discrete states (e, h_s^*, \mathbf{T}) with respect to a fixed Cartesian co-ordinate system as sketched in Fig. (4.1). The shear plane or so-called discontinuity plane is characterized by a different velocity gradient $\nabla \mathbf{v}$ on either side of this plane. The jump of the velocity gradient can be represented by the dyadic product of the unit normal \mathbf{n} of the discontinuity plane and a vector \mathbf{g} defining the discontinuity mode of the velocity gradient [4], i.e.

$$[[\nabla \mathbf{v}]] = \mathbf{g} \otimes \mathbf{n} \neq 0. \quad (4.1)$$

The condition for a continuing equilibrium across the discontinuity requires the jump of the stress rate normal to the discontinuity plane to be zero [25]:

$$[[\dot{\mathbf{T}}]] \mathbf{n} = 0. \quad (4.2)$$

Herein the jump of the stress rate can be related to the jump of the Jaumann stress rate, i.e.

$$[[\dot{\mathbf{T}}]] = [[\dot{\mathbf{T}}]] + [[\mathbf{W}]] \mathbf{T} - \mathbf{T} [[\mathbf{W}]]. \quad (4.3)$$

where $\dot{\mathbf{T}}$ is the response of the hypoplastic model (3.6) and \mathbf{W} denotes the antisymmetric part of the velocity gradient. Inserting the Jaumann stress rate into Eq.(4.2) leads to the relation:

$$f_s (\mathcal{L} : [[\mathbf{D}]]) \mathbf{n} + \lambda f_s f_d \mathbf{N} \mathbf{n} + [[\mathbf{W}]] \mathbf{T} \mathbf{n} - \mathbf{T} [[\mathbf{W}]] \mathbf{n} = 0,$$

with:

$$[[\mathbf{D}]] = \frac{\mathbf{g} \otimes \mathbf{n} + \mathbf{n} \otimes \mathbf{g}}{2}, \quad [[\mathbf{W}]] = \frac{\mathbf{g} \otimes \mathbf{n} - \mathbf{n} \otimes \mathbf{g}}{2}, \quad (4.4)$$

$$\lambda = [[\sqrt{\mathbf{D} : \mathbf{D}}]].$$

At the onset of a shear band bifurcation the quantities f_s , f_d , \mathcal{L} and \mathbf{N} of Eq.(3.6) are the same on either side of the discontinuity plane and they are independent of the velocity gradient. It is a peculiarity in hypoplasticity that the possibility of different incremental stiffnesses due to a different velocity gradient on either side of the discontinuity is taken into account by the single relation (4.4) and there is no need to distinguish whether the material outside the shear band undergoes loading or unloading (e.g. [3, 9, 31]). Relation (4.4) can be rewritten as $\mathbf{K} \mathbf{g} = \lambda \mathbf{r}$ or:

$$\mathbf{g} = \lambda \mathbf{K}^{-1} \mathbf{r}, \quad (4.5)$$

with:

$$\begin{aligned} \mathbf{K} &= f_s \mathbf{b}_1 + \frac{1}{2} \mathbf{b}_2, \\ \mathbf{b}_1 &= \hat{a}^2 \frac{1}{2} (\mathbf{I} + \mathbf{n} \otimes \mathbf{n}) + \left(\hat{\mathbf{T}} (\mathbf{n} \otimes \mathbf{n}) \right) \hat{\mathbf{T}}, \\ \mathbf{b}_2 &= (\mathbf{n} (\mathbf{T} \mathbf{n})) \mathbf{I} - (\mathbf{n} \otimes \mathbf{n}) \mathbf{T} - \mathbf{T} + \mathbf{T} (\mathbf{n} \otimes \mathbf{n}) \end{aligned} \quad (4.6)$$

and

$$\mathbf{r} = -f_s f_d \hat{a} (\hat{\mathbf{T}} + \hat{\mathbf{T}}^*) \mathbf{n}. \quad (4.7)$$

Inserting relation (4.5) for \mathbf{g} into the norm of $[[\mathbf{D}]]$, i.e.

$$\sqrt{[[\mathbf{D}]] : [[\mathbf{D}]]} = \sqrt{\frac{(\mathbf{g} \mathbf{g}) + (\mathbf{g} \mathbf{n})^2}{2}} = \gamma \quad (4.8)$$

leads to the bifurcation condition:

$$f(\theta) = \sqrt{\frac{(\mathbf{K}^{-1} \mathbf{r})(\mathbf{K}^{-1} \mathbf{r}) + [(\mathbf{K}^{-1} \mathbf{r}) \mathbf{n}]^2}{2}} - \frac{\gamma}{|\lambda|} = 0. \quad (4.9)$$

The components of the unit normal \mathbf{n} of the discontinuity plane are related to the unknown shear band inclination angle ϑ , i.e. $\mathbf{n} = [-\sin \vartheta, \cos \vartheta, 0]^T$ with respect to the co-ordinate system in Fig. (4.1).

\mathbf{K} and \mathbf{r} depend on the current state quantities: e , h_s^* , and \mathbf{T} . In order to find the lowest possible bifurcation stress ratio the value of $\gamma/|\lambda|$ can be set equal to 1 as discussed for instance by Wu et al. [32] and Bauer [4]. Thus, relation (4.9) represents an equation for the unknown ϑ , whereby only real solutions to (4.9) indicate the possibility of a shear band bifurcation.

For a homogeneous plane strain compression under a constant lateral stress of $T_{11} = -0.8 \text{ MPa}$ the results are shown for an initial loose material (Fig. 4.2a) and an initially dense material (Fig. 4.2b) for both dry state ($\psi = 1$) and water saturated state ($\psi = 0.34$) of the solid material. In all the tests an initially isotropic stress state was assumed. The stress-strain curves and volume-strain curves show a strong influence of the initial void ratio and they are different for the dry and the water saturated material. In particular the incremental stiffness at the beginning of compression is higher for an initially dense material and a dry state. The densification is more pronounced in the case of an initially looser material and for saturated states. Dilatancy can only be detected for the initially dense and dry material.

Starting from the isotropic state the bifurcation criterion (4.9) was examined for the individual stress paths. In Fig. (4.2) the first possibility where a shear band can appear is marked with a dot. Therefore the bold part of the curves denotes states in which a spontaneous shear band bifurcation is not possible. But states above the first bifurcation point

(dotted curves) again fulfill criterion (4.9) also for $\gamma > |\lambda|$ as discussed in detail for an inherently isotropic material by Bauer [4]. It can clearly be seen that the smallest stress ratio for a possible shear band bifurcation occurs before the peak state. The stress ratio is lower for the initially higher void ratio and for the saturated state of the material. But for the same initial density the difference of the predicted stress ratio for the dry state and the saturated state of the material is not very pronounced. The shear band inclination ϑ is higher for the initially denser material and the dry state.

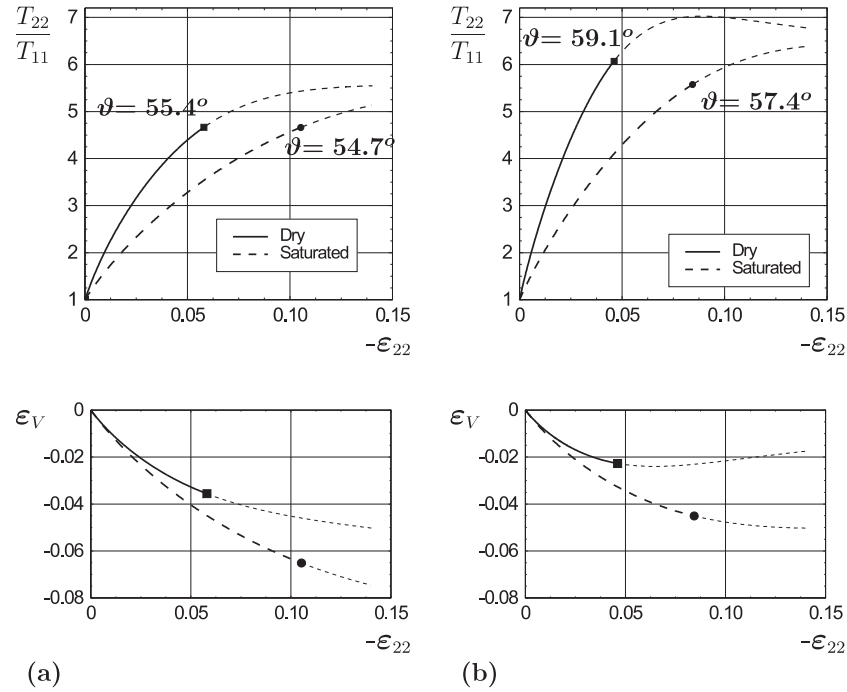


Fig. 4.2. Onset of shear band bifurcation under plane strain compression starting from an initial void ratio of: (a) $e_0 = 0.418$ for the dry state ($\psi = 1$), $e_0 = 0.387$ for the saturated state ($\psi = 0.34$), (b) $e_0 = 0.29$ for the dry state ($\psi = 1$), $e_0 = 0.285$ for the saturated state ($\psi = 0.34$)

5 Conclusions

A hypoplastic continuum model is presented to describe the essential properties of weathered rockfill materials. In particular an increase of the compressibility and a decrease of the limit void ratios with an increase of the moisture content of the solid material is modeled in a simplified manner using only a moisture dependent granular hardness. The constitutive equation for the evolution of the stress is based on nonlinear tensor-valued functions depending on the current void ratio, the stress, a moisture dependent granular hardness and the rate of deformation. As the hypoplastic concept does not need to distinguish between elastic and plastic deformation the calibration of the constitutive constants is rather easy. The calibration is carried out based on experiments for a weathered broken granite. It is demonstrated in this paper that the mechanical behavior of an initially loose and dense material can be captured with a single set of constants. The comparison of the numerical simulations of isotropic compression and triaxial compression with experiments shows that the model captures the essential properties of weathered rockfill materials for both dry and water saturated grains. For a homogeneous plane strain compression under a constant lateral stress the possibility of spontaneous shear band bifurcation is analyzed for different initial states. It can be concluded that the lowest possible bifurcation stress ratio occurs before the peak and the stress ratio and shear band inclination is higher for dry and an initially dense state of the material.

Acknowledgements

Support from the Ministry for Science and Technology in China and the Federal Ministry of Education, Science and Culture in Austria for the bilateral scientific- technological co-operation between Hohai University in Nanjing and Graz University of Technology is greatly acknowledged.

References

1. Bauer E. (1995) Constitutive modeling of critical states in hypoplasticity. In: Proceedings of the Fifth International Symposium on Numerical Models in Geomechanics, Pande and Pietruszczak (eds). Balkema press, pp. 15-20
2. Bauer E. (1996) Calibration of a comprehensive hypoplastic model for granular materials. Solis and Foundations, vol 36(1), pp13-26
3. Bauer E, Huang W (1998) The dependence of shear banding on pressure and density in hypoplasticity. In: Proc. of the 4th Int. Workshop on Localization

- and Bifurcation Theory for Soils and Rocks, Adachi, Oka and Yashima (eds). Balkema, pp. 81-90
4. Bauer E (1999) Analysis of shear band bifurcation with a hypoplastic model for a pressure and density sensitive granular material. *Mechanics of Materials*, vol 31, pp. 597-609
5. Bauer E (2000) Conditions for embedding Casagrande's critical states into hypoplasticity. *Mechanics of Cohesive-Frictional Materials*, vol 5, pp. 125-148
6. Bauer E, Herle I (2000) Stationary states in hypoplasticity. In: *Constitutive Modelling of Granular Materials*, Kolymbas (ed). Springer-Verlag, pp. 167-192
7. Bauer E, Zhu Y (2004) Constitutive modeling of the influence of pressure, density and moisture content on the mechanical behavior of rockfill materials. In: *Proc. of the 4th Int. Conference on Dam Engineering*, Wieland, Rena and Tan (eds). Balkema Publisher, Nanjing, pp. 139-146
8. Bouvard D, Stutz P (1986) Experimental study of rheological properties of sand using a special triaxial apparatus. *Geotechnical Testing Journal*, vol 9(1), pp. 10-18
9. Chambon R, Desrues J (1985) Bifurcation par localisation et non linearite incrementale: un exemple heuristique d'analyse complete. In: *Plastic Instability*, Presses de l'ENPC (eds). Paris, pp. 101-113
10. Chambon R (1989) Bases theoriques d'une loi de comportement incrementale consistante pour les sols. Groupe C.O.S.M. Rapport de Recherche
11. Charlier R, Chambon R, Desrues J, Hammad W (1991) Shear band bifurcation and soil modeling: a rate type constitutive law for explicit localization analysis. In: *3rd Int. Conf. on Constitutive Laws for Engineering Materials*, Desai and Krempl (eds). ASME Press: Tucson, pp. 1-4
12. Charles J A and Watts K S (1980) The influence of confining pressure on the shear strength of compacted rockfill. *Geotechnique*, vol 30(4), pp. 353-367
13. Darve F (1991) Incrementally non-linear constitutive relationships. In: *Geomaterials: Constitutive Equations and Modelling*, Darve (ed). Elsevier press, pp. 213-237
14. Desrues J, Chambon R (2000) Shear band analysis and shear moduli calibration. *International Journal of Solids and Structures*, vol 39, pp. 3757-3776
15. Gudehus G (1996) A comprehensive constitutive equation for granular materials. *Soils and Foundations*, vol 36(1), pp. 1-12
16. Gudehus G (1997) Attractors, percolation thresholds and phase limits of granular soils. In: *Powders and grains*, Behringer and Jenkins (eds). Balkema, pp. 169-183
17. Hill R (1962) Acceleration waves in solids. *Journal of the Mechanics and Physics of Solids*, vol 10, pp. 1-16
18. Herle I, Gudehus G (1999) Determination of parameters of a hypoplastic constitutive model from properties of grain assemblies. *Mechanics of Cohesive-Frictional Materials*, vol 4, pp. 461-486
19. Kast K, Blinde A, Brauns J (1985) Verdichtungs-, Verformungs- und Saettigungsverhalten von Schüttungen in Abhaengigkeit von der

- geologischen Gesteinsentfestigung. In: Ingenieurgeologische Probleme im Grenzbereich zwischen Locker- und Festgesteinen. Springer-Verlag: Berlin Heidelberg
20. Kast K (1992) Mechanisches Verhalten von Granitschuttungen. In: Veroeffentlichungen des Institutes fuer Bodenmechanik und Felsmechanik der Universitaet Fridericiana in Karlsruhe, Heft 125
21. Kolymbas D (1991) An outline of hypoplasticity. *Archive of Applied Mechanics*, vol 3, pp. 143-151
22. Matsuoka H and Nakai T (1977) Stress-strain relationship of soil based on the 'SMP'. In: *Proc. of Specialty Session 9, IX Int. Conf. Soil Mech. Found. Eng.*, Tokyo, pp. 153-162
23. Nobari E S, Duncan J M (1972) Effect of reservoir filling on stress and movements in earth and rockfill dams. U.S.Army Engineers Waterways Experiment Station
24. Rzdakowski B, Zurek J (1970) Influence de l'Eau sur la Deformabilites des Roches Broyees et sur le Tassement des Barrages en Enrochement. In: *Proc. Xth Congr. on Large Dams*, Montreal, vol 1, pp. 857-867
25. Rice J, Rudnicki J W (1980) A note on some features on the theory of localization of deformation. *International Journal of Solids and Structures*, vol 16, pp. 597-605
26. Rudnicki J W, Rice J (1975) Conditions for the localization of deformation in pressure sensitive dilatant materials. *Journal of the Mechanics and Physics of Solids*, vol 23, pp. 371-394
27. Tamagnini C, Viggiani G, Chambon R (2000) A review of two different approaches to hypoplasticity. In: *Constitutive Modelling of Granular Materials*, Kolymbas (eds). Springer press, pp. 107-145
28. Tamagnini C, Viggiani G, Chambon R (2001) Some remarks on shear band analysis in hypoplasticity. In: *5th Int. Workshop on Localisation and Bifurcation Theory in Geomechanics*, Muehlhaus, Dyskin and Pasternak (eds). Balkema Publisher: Perth, pp. 85-93
29. Vardoulakis I and Sulem J (1995) *Bifurcation Analysis in Geomechanics*. Blackie Academic & Professional, London
30. von Wolffersdorff P -A (1996) A hypoplastic relation for granular materials with a predefined limit state surface. *Mechanics of Cohesive-Frictional Materials*, vol 1, pp. 251-271
31. Wu W, Sikora Z (1991) Localized bifurcation in hypoplasticity. *International Journal of Engineering Science*, vol 29(2), pp. 195-201
32. Wu W, Sikora Z (1992) Localized bifurcation in pressure sensitive dilatant granular materials. *Mechanics Research Communications*, vol 19, pp. 289-299
33. Wu W, Bauer E (1993) A hypoplastic model for barotropy and pyknotropy of granular soils. In: *Proc. of the Int. Workshop on Modern Approaches to Plasticity*, Kolymbas (eds). Elsevier, pp. 225-245
34. Wu W, Bauer E and Kolymbas D (1996) Hypoplastic constitutive model with critical state for granular materials. *Mechanics of Materials*, vol 23, pp. 45-69

35. Wu W and Niemunis A (1996) Failure criterion, flow rule and dissipation function derived from hypoplasticity. *Mechanics of Cohesive-Frictional Materials*, vol 1, pp. 145-163
36. Wu W (2000) Nonlinear analysis of shear band formation in sand. *International Journal for Numerical and Analytical Methods in Geomechanics*, vol 24, pp. 245-263
37. Wu W and Kolymbas D (2000) Hypoplasticity then and now. In: *Constitutive Modelling of Granular Materials*, Kolymbas (eds). Springer press, pp. 57-105

Shear Zone Formation in 2D Random Granular Specimens within Enhanced Hypoplasticity

A. V. Dyskin¹ and E. Pasternak²

¹School of Civil and Resource Engineering,
University of Western Australia,
Australia,
E-mail: adyskin@cyllene.uwa.edu.au

²School of Mathematics and Statistics,
University of Western Australia,
Australia.

Summary

We consider a mechanism of macroscopic crack growth and failure in rock and rock mass in compression based on three-dimensional patterns of stress non-uniformity associated with generation of multitudes of wing cracks. In 3D each wing crack has a limiting ability to grow and hence cannot produce sample failure on its own. Neither the crack coalescence can form 3D patterns that can evolve into a macroscopic crack. Instead opening and shearing of the wing cracks produce additional stress disturbance. The combined effect of the stress disturbances from all wing cracks results in a non-uniform stress field spatially varying in a random fashion. The main feature of such a field is that any plane running through the sample can potentially have parts subjected to tensile stress alongside with the parts under compression (the average stress equal to the applied external load acting on this plane). As the load increases, these stress variations become stronger and, eventually, produce a macroscopic tensile crack at the place where the tension was maximal. Further growth of the macrocrack proceeds by initiating new segments, offset from the main crack plane in order to avoid the places under compression. This apparently en-echelon fracture is formed through a specific mechanism of tensile crack growth rather than coalescence. The macroscopic crack is inclined to the direction of axial compression at the angle maximising the average magnitude of the tensile parts of the stress field. This angle depends upon the ratio between total normal opening (dilatancy) and shear of the wing cracks, which in its own term depends upon the material micro-

structure and the confining pressure. When this ratio is above a certain threshold, the macrocrack will be parallel to the direction of axial compression producing splitting. When the ratio is below the threshold, the macrocrack will be inclined and look like shear fracture.

1 Introduction

Failure in compression of heterogeneous materials such as rocks and, at large scales the Earth's crust, is characterised by two major modes (see Germanovich et al. 1994 and the literature cited there): (1) splitting or columnar failure, predominantly observed in uniaxial compression; (2) shear or oblique failure observed in triaxial compression and, often in uniaxial compression. In the latter case the sample is broken by what appears as shear cracks.

The most popular approach to describe shear failure is to use the Mohr-Coulomb theory or its various modifications, which adequately represent experimental data related to the oblique failure. In this theory, as well known, the direction of the future fracture is determined as the one at which the shear stress reaches the friction stress at the least load magnitude the latter being referred to as the compressive strength. The drawbacks of this theory are also well known. Firstly, it has a contradiction in itself since it is based on friction properties of a not yet existing interface. This immediately turns the Mohr-Coulomb criterion into an empirical one in which the friction parameters are treated as internal material parameters to be back calculated from the results of compressive tests. Subsequently, the application of the criterion becomes limited to the cases allowing direct testing, which often excludes *in-situ* characterisation since direct transfer of laboratory data to large-scale situations is precluded by the scale effect. The second drawback is the inability of the Mohr-Coulomb theory to explain the splitting. In view of these drawbacks a considerable effort was devoted to developing micromechanical models of failure.

The majority of models developed to explain splitting are based on the concept of wing crack – the crack generated by a local stress concentrator (a pre-existing shear crack or pore or a certain type of grain contact) assuming that the wing crack can grow extensively at least under uniaxial compression as observed in 2D experiments (e.g., Brace and Bombolakis 1986, Horii and Nemat-Nasser 1986). The failure is attributed either to the growth of one of the wing cracks throughout the whole sample or to unstable crack growth caused by interaction between the cracks (e.g., Ashby and Hallam 1986, Germanovich and Dyskin 1988, Kemeny 1991).

These 2D models fail however to recognise the fact that the real three dimensional wing cracks have an intrinsic limitation to the growth preventing the wing elongation beyond the size of the initial shear crack even in the most favourable case of uniaxial compression, Fig. 1.1.

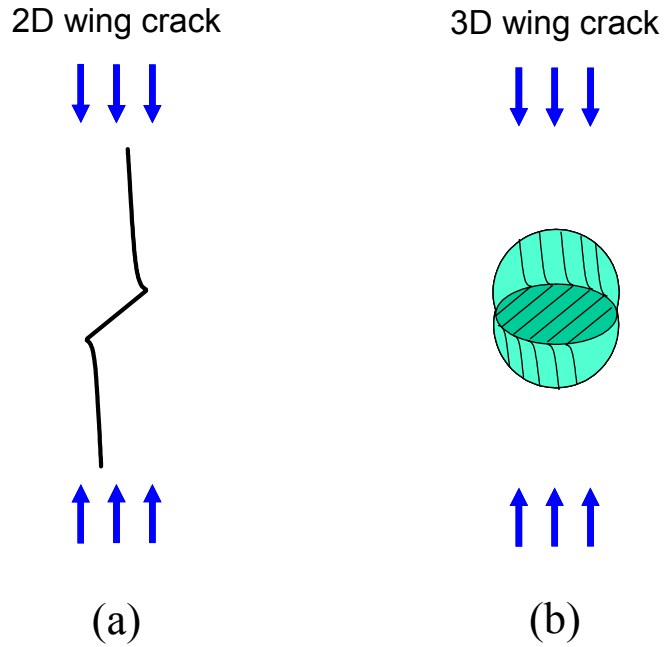


Fig. 1.1. Wing crack growth in uniaxial compression: (a) 2D wing crack growth. The wings are capable of extensive growth and can reach lengths macroscopic as compared to the length of the initial crack; (b) 3D wing crack growth. The wings have intrinsic limitations to their growth. Their maximum dimensions are comparable with the size of the initial crack, Dyskin et al. (2003).

Modelling of shear failure in compression, that takes into account the fact that the shear cracks do not propagate in their own plane, but rather kink, is based on considering various mechanisms of wing crack coalescence (e.g., Wittmann 1981, Stavrogin and Tarasov 2001) or en-echelon formation (e.g., Horii and Nemat-Nasser 1986, Schulson 1990, Reches and Lockner 1994). A typical model of en-echelon crack is shown in Fig. 1.2a. The main feature of models of this kind is that they are two-

dimensional. As soon as one returns to a real 3D situation the picture becomes complicated. Indeed, a direct three-dimensional analogue of the en-echelon model is an arrangement sketched in Fig. 1.2b. Two conditions should be satisfied to make such an arrangement possible. Firstly, all wing cracks or the corresponding parts of the wings participating in the formation of the en-echelon crack should be more or less parallel to each other. Secondly, since the wings are more or less equiaxial, the ones forming the en-echelon crack should have suitable spatial arrangement.

In order to make the idea of en-echelon crack formation viable, it is therefore necessary to identify the mechanism(s) ensuring these arrangements. If one hypothesises that the cracks forming en-echelon constitute only a portion of all cracks then, inevitably, extremely high concentrations of such cracks should be assumed. In particular, given that the dimensions of the wing cracks in rocks are often of the order of the grain size, the first of the above conditions demands that the grains happened to be in the place of future en-echelon crack be already separated from the rest of the rock volume. Indeed, while the wings separate the grain from the sides, the initial crack that initiated the wings separates the grain from above or below (the compression direction being vertical). This obviously contradicts the experimental observations according to which the formation of macroscopic shear fracture does not yet lead to full rock separation.

The above consideration suggests that the cracks forming en-echelon were not there initially, but rather were formed in the process of propagation of the macrocrack.

Direct finite element simulations of failure in heterogeneous materials are based on specifying failure criteria for each finite element (e.g., Zou et al. 1996). In essence, these criteria are usually chosen similar to the ones deduced from the tests on macroscopic samples. Therefore, the question of the failure criterion is simply shifted from macroscopic to microscopic scale without actually producing the relevant failure mechanism. Models treating the shear cracks as planes of strain localisation (e.g., Rudnicki and Rice 1975) face the same problem: the material behaviour at the micro level should resemble the macroscopic behaviour the model is set to explain. To complicate the matter further, the direct numerical simulations suffer from mesh-dependence which renders the simulations unusable.

Dyskin (1999) noticed that the wing cracks create considerable stress non-uniformity (spatial stress fluctuations) with the material in some places subjected to tensile stresses and therefore capable of generating tensile cracks. Based on this idea a 3D model of splitting crack formation and propagation was proposed. In this paper we extend this idea to model

the formation and propagation of inclined tensile cracks which produce oblique (shear-like) failure.

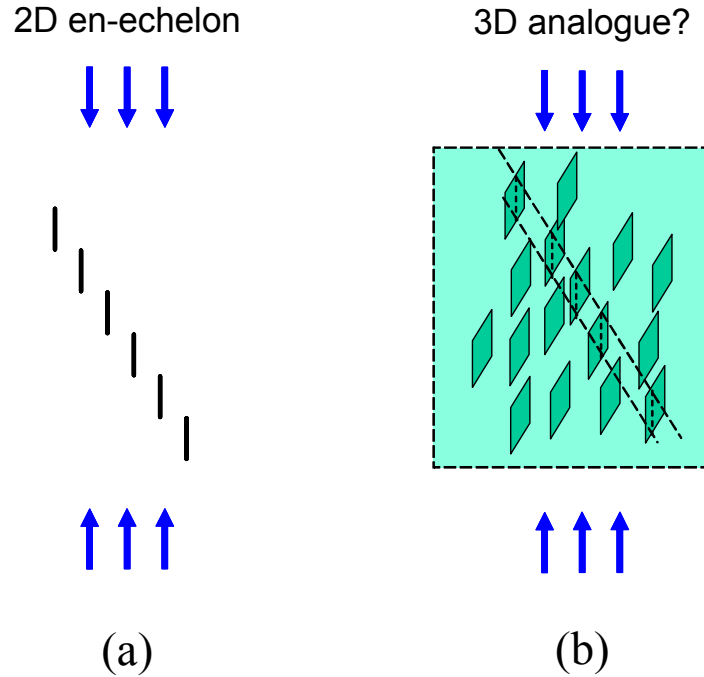


Fig. 1.2. 'En-echelon' crack: (a) 2D en-echelon crack as depicted following cross-section observations in rock samples or the Earth's crust; (b) a schematics of possible 3D analogue of en-echelon crack. It is assumed that the vertical fractures being parts of wing cracks are approximately equiaxial, as shown in Fig. 1.1. The broken line shaded area signifies a cross-section of observation, while two inclined broken lines indicate the position of traces of the en-echelon crack in the cross-section.

2 Mechanism of Crack Propagation in Non-Uniform Stress Fields

The stress field generated by wing cracks as well as other heterogeneities is non-uniform and random owing to their random locations, orientations, shapes and dimensions. In the parts of the sample where the stress variations become tensile new cracks can be generated and grown to

macrocracks, Dyskin (1999). Fig. 2.1 explains a possible mechanism of tensile macrocrack formation and propagation. Fig. 2.1a shows a possible realisation of random field of a normal stress component σ_{33} ; the stress increasing from dark to white, such that the dark areas correspond to compression, while the white areas correspond to tension. For the illustration purpose, only a section parallel to the (x_2, x_3) plane is shown. Obviously, the first crack (crack 1) is generated at the area with the maximum tensile stress. This crack will propagate until it is arrested in the areas subjected to compression. As the applied load increases, so does the amplitude of the stress variations. Further propagation of crack 1 will however be prevented by similarly increased compression; instead a new crack (crack 2) will be generated where the original stress distribution showed no compression. This will result in a discontinuous offset-type trajectory of crack growth, which in the real 3D case will look like the one shown in Fig. 2.1b. Essentially, the crack segments will be situated at places where no compressive stresses acted. On average, the magnitude of these stresses is equal to the mathematical expectation of positive (tensile) values

$$\sigma_+ = \int \max(\sigma, 0) f(\sigma) d\sigma \quad (2.1)$$

where σ denotes the relevant stress component, $f(\sigma)$ is the probability density function.

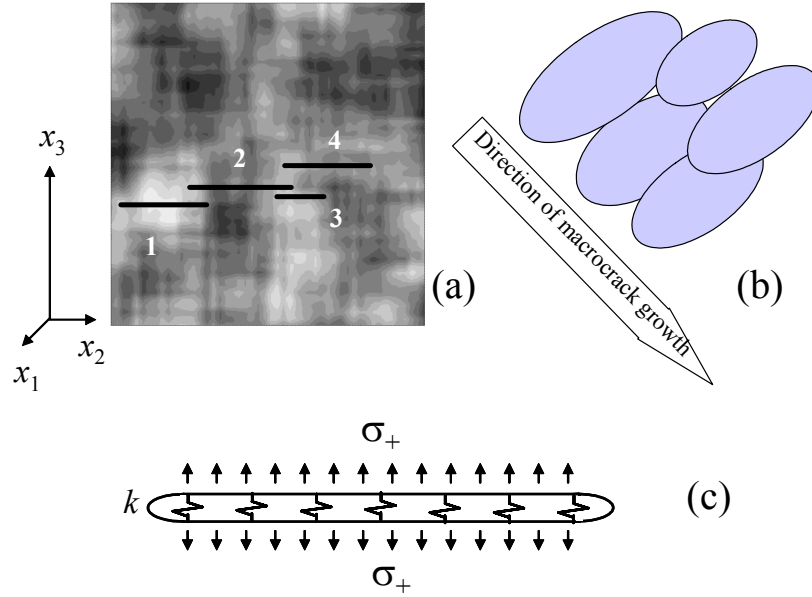


Fig. 2.1. Macroscopic crack formation and growth under spatially random stress field: (a) a realisation of the random stress field σ_{33} ; the maximum compression is shown in black, the tension - in white. The first crack segment (crack 1) appears at the place of maximum tension. Crack 2 is then generated at the closest place where the compressive stress is minimal (whitish spot), then other segments (cracks 3 and 4) are generated in the same fashion; (b) a 3D structure of the compound (en-echelon) macrocrack; (c) the macrocrack is modelled as a crack (a cross-section is shown) with Winkler layer of stiffness k that depends upon the size and the density of the segment cracks

We will model such a complex compound (en-echelon) crack, macroscopically, as a planar crack with Winkler layer, i.e. we will assume that opening of the crack is resisted by linear links between the faces, Fig. 2.1c. These linear links model the action of intact material between the crack segments. The Winkler layer is characterised by stiffness k that locally relate the mutual normal displacement of the crack faces Δv and the normal stress σ , $\sigma = k\Delta v$, the stiffness k being dependent upon the crack segment sizes and concentration. We will also assume that the faces of the macroscopic crack are subjected to a uniform load σ_+ associated with the action of stress fluctuations. We assume further that the macro-crack is

disk-like of a radius R . We will characterise the conditions of its growth using the macroscopic scale, where we can employ the conventional criterion of crack propagation $K_I = K_{Ic}$. Here K_{Ic} is the macroscopic fracture toughness which characterise the conditions of creation of the new crack segments.

Since the macrocrack is much larger than the characteristic size of the Winkler layer, E/k , where E is the Young's modulus of the rock, the stress intensity factor has the following form, Shifrin (1988)

$$K_I = \sigma_+ \sqrt{\frac{E}{\pi k(1-\nu^2)}} \quad (2.2)$$

One can see that the stress intensity factor is independent of the macrocrack size, i.e. the macrocrack can support its own growth without an increase in the load.

A remark should be made with respect to the concept introduced. Macroscopically, the considered crack grows as an open tensile crack. However, it is also subjected to shear stress. The corresponding shear component of the relative displacement of the crack faces creates tensile stresses on one side of the macrocrack contour and compressive on the other. In the process of the macrocrack growth the tensile stress concentration leads to the appearance of small tensile cracks approximately oriented in the vertical direction and predominantly located on one side of the macrocrack, Fig. 2.2. It is these cracks that create impression of en-echelon nature of the macrocrack. It has also been observed on sample cross-sections by Moore and Lockner (1995) that these vertical cracks are biased to one side of the macrocrack.

We shall now introduce a method for estimating the fluctuation-induced stress σ_+ . Suppose the random stress is Gaussian with the uniform mathematical expectation, σ_{av} and standard deviation, Σ . Then direct calculations give:

$$\begin{aligned} \sigma_+ &= \Sigma \left\{ \xi \left[\frac{1}{2} - \Phi(-\xi) \right] + \frac{1}{\sqrt{2\pi}} e^{-\frac{\xi^2}{2}} \right\} \\ \xi &= \frac{\sigma_{av}}{\Sigma}, \quad \Phi(x) = \frac{1}{\sqrt{2\pi}} \int_0^x e^{-\frac{x^2}{2}} dx \end{aligned} \quad (2.3)$$

Therefore, in order to determine the fluctuation-induced stress one needs to know the statistical properties of the Gaussian stress fluctuations. These will be determined in the following section.

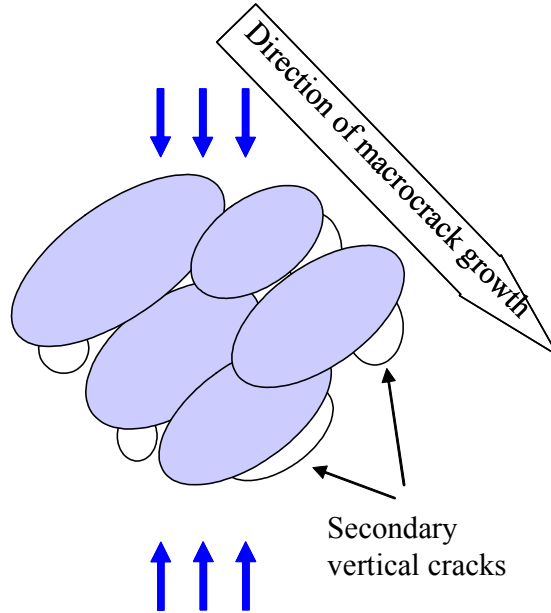


Fig. 2.2. Formation of secondary tensile cracks in the process of macrocrack growth. These secondary cracks may be responsible for the en-echelon appearance.

3 Statistical Properties of Non-Uniform Stress Field Created by Many Wing Cracks

In order to quantify the mechanism by which this field produces and drives macrocracks we need to determine the mathematical expectation and variance of this field.

Suppose that the rock volume is loaded such that in a similar homogeneous volume a uniform stress field σ_{ik}^0 ($i, k=1, 2, 3$) would be produced. In the case of compression of magnitude p in x_3 direction (see the coordinate frame on Fig. 3.1) and confining pressure of magnitude q in the normal directions

$$\sigma_{11}^0 = \sigma_{22}^0 = -q, \quad \sigma_{33}^0 = -p, \quad \sigma_{12}^0 = \sigma_{13}^0 = \sigma_{21}^0 = 0 \quad (3.1)$$

The actual stress field σ_{ik} is of course different from the uniform one, predominantly owing to the effect of wing cracks with some contribution from other heterogeneities. Nevertheless its volumetric average over the whole sample, $\langle \sigma_{ij} \rangle$, is equal to σ_{ij}^0 . Indeed, suppose a volume V is loaded at its external surface S by tractions $\sigma_{ij}^0 n_j$, where n_i is the external normal vector to S , while its internal surfaces (e.g., pores or cracks) are free from external load (only contact forces can act there). We will also neglect the body forces.

We use the following identity which is based on the divergence theorem

$$\int_{S_0} \sigma_{ik}(\mathbf{x}) x_j n_k dS = \int_V (\sigma_{ik}(\mathbf{x}) x_j)_{,k} dV_{\mathbf{x}} = \int_V \sigma_{ik,k}(\mathbf{x}) x_j dV_{\mathbf{x}} + \int_V \sigma_{ik}(\mathbf{x}) \delta_{jk} dV_{\mathbf{x}} \quad (3.2)$$

The first integral in the right-hand part is equal to zero because of the equations of equilibrium with zero body forces. Because the actual and uniform stress fields corresponds to the same tractions at S , one obtains

$$\begin{aligned} \langle \sigma_{ij} \rangle &= \frac{1}{V} \int_V \sigma_{ij}(\mathbf{x}) dV_{\mathbf{x}} = \frac{1}{V} \int_{S_0} \sigma_{ik}(\mathbf{x}) x_j n_k dS \\ &= \frac{1}{V} \int_{S_0} \sigma_{ik}^0(\mathbf{x}) x_j n_k dS = \langle \sigma_{ij}^0 \rangle = \sigma_{ij}^0 \end{aligned} \quad (3.3)$$

Furthermore, assuming ergodicity, the mathematical expectation of this random stress field can be found

$$\overline{\sigma_{ik}} = \langle \sigma_{ik} \rangle = \sigma_{ik}^0 \quad (3.4)$$

In order to estimate the variance of the stress field generated by the wing cracks we model each crack by a dislocation loop, Fig. 3.1, with the shear component of the Burgers vector, b_t , directed parallel to the axial load and the normal component, b_n , directed perpendicular to the axial load. The shear component reflects the contribution of the wing crack to the non-linear part of axial strain, while the normal component reflects the wing crack contribution to dilatancy. As further simplification, in order to account for the collective effect of the wing cracks while neglecting the peculiarities of the shape of each crack, we replace the dislocation loops with point defects. It will be done by limiting transition of the loop area, A , to zero keeping the corresponding volumes, $U_t = b_t A$, $U_n = b_n A$, constant.

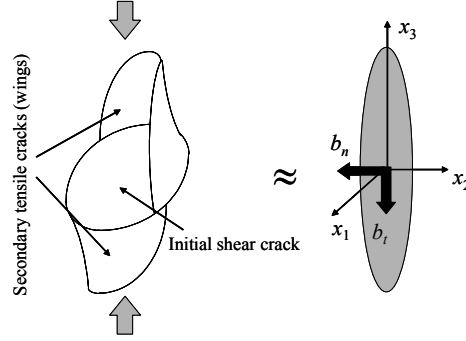


Fig. 3.1. Wing crack evolved from an initial inclined shear crack (left) and its model as a dislocation loop (right) with Burgers vector (b_t, b_n) .

We represent, following Landau and Lifshitz (1959), the dislocation loop through equivalent body forces

$$f_i = \frac{1}{2} \lambda_{iklm} [(n_l b_m + n_m b_l) \delta(\zeta)]_{,k}, \quad (3.5)$$

where n_m and b_m are the components of unit normal vector to the loop and the Burgers vector respectively, $\delta(\zeta)$ is the delta-function of coordinate ζ along the normal vector, $(\cdot)_{,k}$ denotes differentiation with respect to x_k (summation is presumed over repeated indexes) and λ_{iklm} is the tensor of elastic moduli. For isotropic rock with the Young's modulus E and Poisson's ratio ν it has the form:

$$\lambda_{iklm} = \frac{E}{1+\nu} \left[\frac{1}{2} (\delta_{il} \delta_{km} + \delta_{im} \delta_{kl}) + \frac{\nu}{1-2\nu} \delta_{ik} \delta_{lm} \right] \quad (3.6)$$

We now represent the crack as a point defect located at a point \mathbf{x}_μ , $\mu = 1, \dots, M$, where M is the number of wing cracks in the rock volume and take into account that in this representation the Burgers vectors are constant

$$b_i = U_n n_i + U_t \delta_{i3}. \quad (3.7)$$

Here we considered that the normal vector, according to Fig. 3.1 is always perpendicular to the x_3 axis. As a result, we come up with the

following expression for the body forces through the volumes of crack opening/shear

$$f_i = 1/2 \lambda_{iklm} (n_l b_m + n_m b_l) \delta(\mathbf{x} - \mathbf{x}_\mu)_{,k} \quad (3.8)$$

Now, using identity (3.2) and the equilibrium equations

$$\sigma_{ij,i} + f_j = 0, \quad (3.9)$$

with the body forces (3.8) one can express the volumetric average of the stress field generated by these point defects, which is the average stress field *outside* the wing cracks. It reads

$$\begin{aligned} \langle \sigma_{ik}^{disl} \rangle &= \sigma_{ik}^0 \\ &+ \frac{E}{1+\nu} \frac{1}{V} \sum_{\mu=1}^M \left[U_n^\mu \left(n_i^\mu n_k^\mu + \frac{\nu}{1-2\nu} \delta_{ik} \right) + \frac{1}{2} U_t^\mu (n_i^\mu \delta_{k3} + n_k^\mu \delta_{i3}) \right] \end{aligned} \quad (3.10)$$

where σ_{ik}^0 is the applied load, V is the rock volume, M is the number of wing cracks in the volume (this number can grow as loading progresses), the superscript index μ refers to a particular wing crack. It is important to distinguish between this stress field which essentially represents the stresses generated at a distance from the wing cracks (since this approximation relates to the scale from which the wing cracks are seen as point defects) with the full stress field (that includes stresses in immediate neighbourhoods of the wing cracks) which volumetric average is given by equation (3.4).

Direct computations of the correlation function for the stress fields in the point defect approximation, Dyskin (1999), suggested that the correlation length is of the order of the wing crack size. Based on this observation, we break the sample volume V into M parts V_λ , $\lambda=1, \dots, M$ such that the averages over V_λ , $\langle \sigma_{ik} \rangle_\lambda$ are approximately independent from each other. Then from the ergodicity, the variance $\text{Var}(\langle \sigma_{ik} \rangle_\lambda)$ can be expressed through the variance of the full volumetric average, $\text{Var}(\langle \sigma_{ik} \rangle)$. We assume that the latter is adequately represented by the variance of (3.10). For wing cracks uniformly oriented in the (x_1, x_2) plane, assuming that the average values of shear ‘volume’ U_t and volume of opening of wing cracks U_n are independent, one obtains

$$\begin{aligned} \text{Var}(\langle \sigma_{ik} \rangle_\lambda) &= \frac{t^2}{2} [\kappa^2 (1 - \delta_{i3} \delta_{k3}) + (\delta_{i3} + \delta_{k3} - 2\delta_{i3} \delta_{k3})] \\ t &= \frac{NEU_t}{2(1+\nu)}, \quad \kappa t = \frac{NEU_n}{2(1+\nu)} \end{aligned} \quad (3.11)$$

where N is the number of wing cracks per unit volume, κ has the meaning of the ratio between dilatancy and inelastic part of the axial strain.

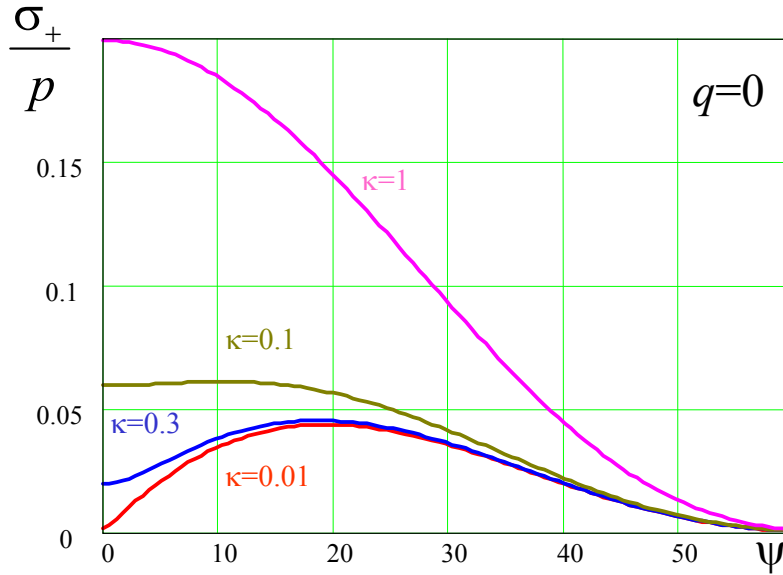
4 A Mechanism of Splitting and Oblique Failure in Compression

Consider a plane inclined at an angle ψ to the x_3 axis and determine the average tensile stress σ_+ acting on that plane. Substituting (3.1), (3.11) into (2.3) one obtains

$$\sigma_+ = \frac{t}{2\sqrt{2\pi}} e^{-\frac{\xi^2}{2}} \cos^2 \psi \sqrt{\kappa^2 + 2 \tan^2 \psi} - (p \sin^2 \psi + q \cos^2 \psi) \left[\frac{1}{2} - \Phi(-\xi) \right]$$

$$\xi = -\frac{2(q + p \tan^2 \psi)}{t \sqrt{\kappa^2 + 2 \tan^2 \psi}} \quad (4.1)$$

Fig. 4.1 shows stress (4.1) for $t=p$ and for different q and κ . It is seen that for $\kappa=1$ stress σ_+ reaches maximum at $\psi=0$, which corresponds to splitting. Small values of κ lead to oblique failure. Since for $q>0$ mainly oblique failure is observed, κ should be small as compared to $\tan(\psi)$.



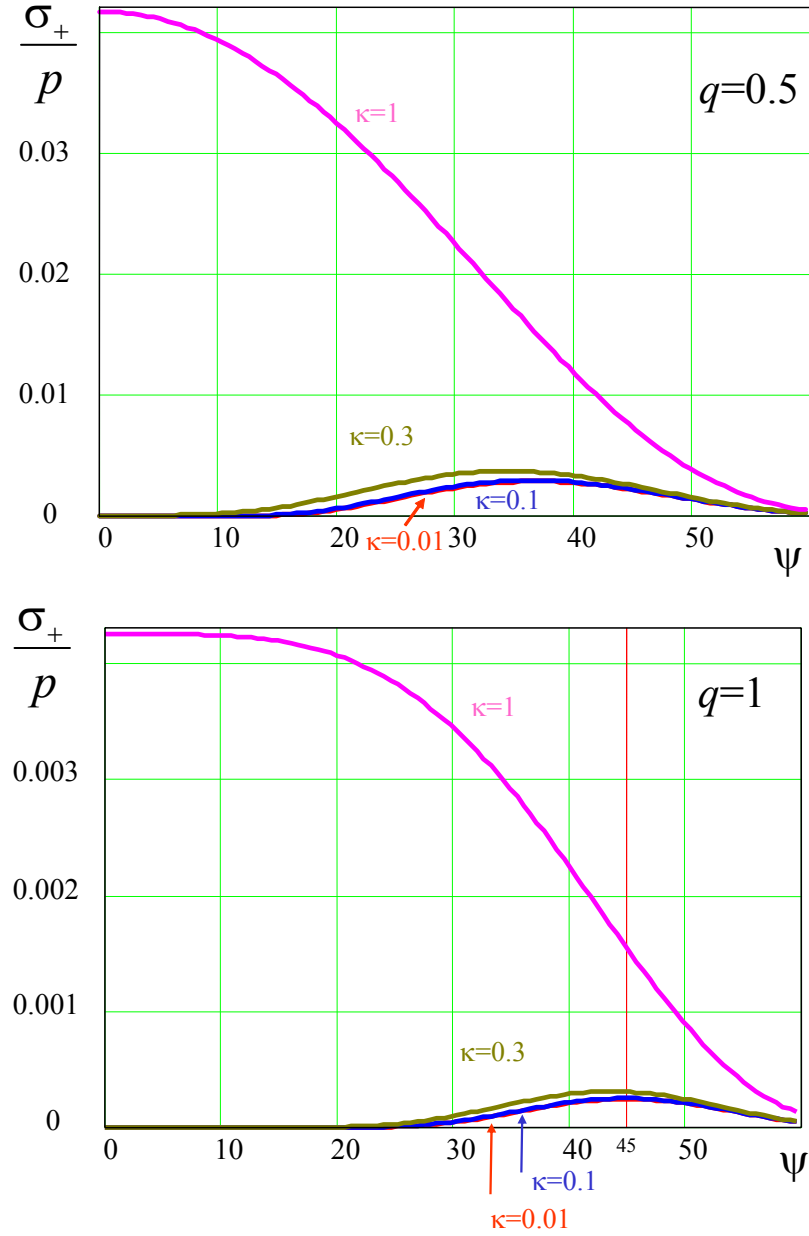


Fig. 4.1. Dependence of average tensile stress acting on a plane vs. the angle of its inclination for various values of the lateral compression q

For uniaxial compression the critical value of κ has the form

$$\kappa_{cr} = -\frac{p\sqrt{2\pi}}{t} + \sqrt{\frac{2\pi p^2}{t^2} + 1} \quad (4.2)$$

Subsequently, $\kappa > \kappa_{cr}$ corresponds to splitting, while $\kappa < \kappa_{cr}$ corresponds to oblique or ‘shear’ failure.

We now assume that the opening of the wing cracks is mainly controlled by sliding of their shear part and for that reason the average opening is proportional to the deviatoric stress acting on them such that $t = \eta(p - q)$, where η is a factor. We also assume that the macrocrack start propagating when the positive component of stress fluctuations acting in its plane reaches a certain critical value: $\sigma_+ = \sigma_{cr}$. For the case of low values of κ , such that $\sqrt{\kappa^2 + 2 \tan^2 \psi} \approx \sqrt{2} \tan \psi$, we can rearrange expression (4.1) in the following way:

$$(p - q) \sin \psi \cos \psi = c + (p \sin^2 \psi + q \cos^2 \psi) \tan \varphi \quad (4.3)$$

where

$$c = \frac{2\sqrt{\pi}\sigma_{cr}}{\eta} e^{\frac{\xi^2}{2}}, \quad \tan \varphi = \left[\frac{1}{2} - \Phi(-\xi) \right] \frac{2\sqrt{\pi}\sigma_{cr}}{\eta} e^{\frac{\xi^2}{2}} \quad (4.4)$$

This is an expression similar to Coulomb-Mohr criterion. In general its parameters are not independent of p and q . If, in addition, $t \gg p$ the Coulomb-Mohr parameters will change little and can be considered independent of the loads p and q .

The values of parameters depend upon the factors associated with the wing cracks, their sizes and distributions. However, the mechanism itself is scale-independent.

5 Conclusions

It is demonstrated that the random stress non-uniformity created by the multitude of wing cracks is sufficient to induce tensile cracks and then make them grow as a macroscopic tensile fracture. Its structure – a set of crack-segments as well as vertical cracks induced by shear stresses in the process of its growth create an appearance of en-echelon fracture. The macroscopic fracture is inclined to the direction of axial compression at the angle maximising the average magnitude of the tensile parts of the stress field. This angle depends upon the ratio between total normal opening

(dilatancy) and shear of the wing cracks. When this ratio is above a certain threshold, the macrocrack will be parallel to the direction of axial compression producing splitting. When the ratio is below the threshold, the macrocrack will be inclined and look like shear fracture.

Acknowledgements

The first author acknowledges the financial support through the University of Western Australia Research Grant 2004 and the Australian Research Council Discovery Grant DP0559737 (2005-2007), the second author acknowledges the support of the Australian Research Council Australian Postdoctoral Fellowship and Discovery Grant, DP0346148 (2003-2006).

References

1. Ashby MF, Hallam SD (1986) The failure of brittle solids containing small cracks under compressive stress states. *Acta Metallurgica* 34:497-510.
2. Brace WF, Bombolakis EG (1963) A note of brittle crack growth in compression. *J. Geophys. Res.* 68:3,709-3,713.
3. Dyskin AV (1999) On the role of stress fluctuations in brittle fracture. *Intern. J. Fracture* 100:29-53.
4. Dyskin AV, Jewell R.J, Joer H, Sahouryeh, E Ustinov KB (2003) Influence of shape and locations of initial 3-D cracks on their growth in uniaxial compression. *Engg. Fracture Mechanics* 70:2115-2136.
5. Germanovich LN, Dyskin AV (1988) A model of brittle failure for materials with cracks in uniaxial loading. *Mechanics of Solids* 23(2):111-123.
6. Germanovich LN, Salganik RL, Dyskin AV, Lee KK (1994) Mechanisms of brittle fracture of rock with multiple pre-existing cracks in compression. *Pure and Applied Geophys.* 143(1/2/3):117-149.
7. Horii H, Nemat-Nasser S (1986) Brittle failure in compression: splitting, faulting, and brittle-ductile transition. *Phil. Trans. R. Soc. Lond.*, A319:337-374.
8. Kemeny JM (1991) A model for non-linear rock deformation under compression due to sub-critical crack growth. *Int. J. Rock Mech. Min. Sci. & Geomech. Abstr.* 28:459-467.
9. Landau LD, Lifshitz EM (1959) *Theory of Elasticity*. Oxford, London Edinburgh New York Toronto Sydney Paris Braunschweig.
10. Moore DE, Lockner DA. (1995). The role of microcracking in shear fracture propagation in granite. *J. Struct. Geol.* 17:95-114.
11. Reches Z, Lockner DA (1994) Nucleation and growth of faults in brittle rocks. *J. Geophys. Res.* B99:18,159-18,173.
12. Rudnicki JW, Rice JR (1975) Conditions for the localization of deformation in pressure-sensitive dilatant materials. *J. Mech. Phys. Solids* 23:371-394,.

13. Schulson EM (1990) The brittle compressive fracture of ice. *Acta Metall. Mater.* 38:1963-1976.
14. Stavrogin AN, Tarasov BG (2001) *Experimental Physics and Rock Mechanics*. Balkema, Rotterdam.
15. Shifrin EI (1988) The I-Mode crack whose sides interact according to a linear law. *Mechanics of Solids* 23, No. 5:91-97.
16. Wittmann FH (1981) Mechanisms and mechanics of fracture of concrete. In: Francois D (ed.) *Advances in Fracture Research*. Pergamon Press, Oxford New York Toronto Sydney Paris Frankfurt, pp. 1467-1487.
17. Zou Y, Taylor WEG, Heath DJ (1996) A numerical model for borehole breakouts. *Int. J. Rock Mech. Min. Sci. & Geomech. Abstr.* 33:103-109.

A Rational Approach to Stress-Dilatancy Modelling Using an Explicit Micromechanical Formulation

J. Bobiński and J. Tejchman

Faculty of Civil and Environmental Engineering,
Gdansk University of Technology,
80-952, Gdansk, Narutowicza 11/12,
Poland.
E-mail: tejchmk@pg.gda.pl

Summary

The paper presents results of numerical simulations of the behaviour of quasi-brittle materials (like concrete) under plane strain conditions. Two boundary value problems with a dominating failure mode I were simulated: uniaxial tension and a three-point bending test for concrete beams with a different size. To model the material behaviour, two different continuum approaches were used: elasto-plastic and an isotropic damage constitutive model with non-local softening. Attention was focused of the effect of a characteristic length on the width of strain localization and load-displacement curve, and an identification of a characteristic length on the basis of the load-displacement curves only from size effect tests.

1 Introduction

The analysis of concrete elements is complex due to occurrence of strain localization which is a fundamental phenomenon under both quasi-static and dynamic conditions [5], [9], [17], [48], [50]. It can occur in the form of cracks (if cohesive properties are dominant) or shear zones (if frictional properties prevail). The determination of the width and spacing of strain localization is crucial to evaluate the material strength at peak and in the post-peak regime. The concrete behaviour can be modeled within continuum mechanics models using, e.g.: non-linear elasticity [34], fracture [4], [24], endochronic theory [3], [8], micro-plane theory [7], [27], plasticity [11], [33], [38], [48], damage theory [11], [16], [20], [37] and coupled plastic-damage approach [14], [26], [32], [42], and discrete models using a lattice approach [23], [30], [43], [49] and DEM [18], [19],

[41]. To describe properly strain localization within continuum mechanics, the models should be enhanced by a characteristic length of microstructure [13]. There are several approaches within continuum mechanics to include a characteristic length and to preserve the well-posedness of the underlying incremental boundary value problem in engineering materials as: second-gradient [17], [35], [36], [37], non-local [2], [10], [16], [39] and viscous ones [13], [45]. Owing to them, objective and properly convergent numerical solutions for localized deformation (mesh-insensitive load-displacement diagram and mesh-insensitive deformation pattern) are achieved. Otherwise, FE-results are completely controlled by the size and orientation of the mesh and thus produce unreliable results, i.e. strain localization becomes narrower upon mesh refinement (element size becomes the characteristic length) and computed force-displacement curves change considerably depending on the width of the calculated localization. In addition, a premature divergence of incremental FE-calculations is often met.

The aim of the present paper is to compare the FE-results of the width of strain localization in concrete elements (characterized by a failure mode I) during uniaxial tension and three-point bending using two different continuum models enhanced by an internal length of microstructure: isotropic elasto-plastic model and isotropic damage model both with non-local softening. The FE-results with respect to the load-displacement curves were compared to some laboratory experiments and the size effect law by Bazant [5]. Attention was focused of the effect of a characteristic length on the width of strain localization and load-displacement curve, and an identification of a characteristic length on the basis of the measured load-displacement curves only.

2 Constitutive Models for Concrete

2.1 Elasto-Plastic Model

An elasto-plastic model with isotropic hardening and softening using two yield conditions was assumed. In a compression regime, a Drucker-Prager criterion was defined as [1]

$$f_1 = q + p \tan \varphi - \left(1 - \frac{1}{3} \tan \varphi\right) \sigma_c(\kappa_1), \quad (2.1)$$

where q – von Mises equivalent stress, p – mean stress, φ – the internal friction angle, σ_c – uniaxial compression yield stress and κ_1 – hardening (softening) parameter equal to plastic vertical strain in uniaxial compression ε_{11}^p . The invariants p and q were defined as

$$p = \frac{1}{3} \sigma_{kk} \quad \text{and} \quad q = \sqrt{\frac{3}{2} s_{ij} s_{ji}}, \quad (2.2)$$

where σ_{ij} is the stress tensor and s_{ij} stands for the deviatoric stress tensor. The flow potential function was taken as

$$g_1 = q + p \tan \psi, \quad (2.3)$$

where ψ is the dilatancy angle. In a tensile regime, a Rankine criterion was assumed with the yield function

$$f_2 = \max \{ \sigma_1, \sigma_2, \sigma_3 \} - \sigma_t (\kappa_2), \quad (2.4)$$

where σ_1, σ_2 and σ_3 – principal stresses, σ_t – the tensile yield stress and κ_2 – softening parameter (equal to the maximum principal plastic strain ε_1^p). The associated flow rule was assumed.

2.2 Damage Model

An isotropic damage continuum model describes the degradation of the material due to micro-cracking with the aid of a single scalar damage parameter D growing from zero (undamaged state) to one (completely damaged state). The stress-strain function is represented by the following relationship

$$\sigma_{ij} = (1 - D) C_{ijkl}^e \varepsilon_{kl}, \quad (2.5)$$

where C_{ijkl}^e – linear elastic material stiffness matrix and ε_{kl} – strain tensor. The damage parameter D acts as a stiffness reduction factor (the Poisson ratio ν is not affected by damage). The growth of the damage variable is controlled by a damage threshold parameter κ which is defined as a maximum of the equivalent strain measure $\tilde{\varepsilon}$ reached during the load history up to time t . The loading function of damage is

$$f(\tilde{\varepsilon}, \kappa) = \tilde{\varepsilon} - \max \{ \kappa, \kappa_0 \} \quad (2.6)$$

where κ_0 – initial value of κ when damage begins. If the loading function f is negative, damage does not develop. During monotonic loading, the parameter κ grows (it coincides with $\tilde{\varepsilon}$) and during unloading and reloading it remains constant. To define the equivalent strain measure $\tilde{\varepsilon}$, two different criteria were assumed: a) a von Mises failure criterion in terms of strains [37] and b) Rankine failure type criterion [28]. In the first case $\tilde{\varepsilon}$ was [37]

$$\tilde{\varepsilon} = \frac{k-1}{2k(1-2\nu)} I_1 + \frac{1}{2k} \sqrt{\frac{(k-1)^2}{(1-2\nu)^2} I_1^2 + \frac{12k}{(1+\nu)^2} J_2}, \quad (2.7)$$

where ν is the Poisson's ratio, and I_1 and J_2 are the first invariant of the strain tensor and the second invariant of the deviatoric strain tensor, respectively:

$$I_1 = \varepsilon_{11} + \varepsilon_{22} + \varepsilon_{33} \quad \text{and} \quad J_2 = \frac{1}{2} \varepsilon_{ij} \varepsilon_{ij} - \frac{1}{6} I_1^2, \quad (2.8)$$

The parameter k in Eq.2.7 denotes the ratio between the compressive and tensile strength of the material. In the second case, the equivalent strain measure $\tilde{\varepsilon}$ was [28]

$$\tilde{\varepsilon} = \frac{1}{E} \max \{ \sigma_i^{eff} \}, \quad (2.9)$$

where E denotes the Young modulus and σ_i^{eff} are the principal values of the effective stress σ_{ij}^{eff}

$$\sigma_{ij}^{eff} = C_{ijkl}^e \varepsilon_{kl} \quad (2.10)$$

To describe the evolution of the damage parameter D , an exponential softening law was used [37]

$$D = 1 - \frac{\kappa}{\kappa_0} \left(1 - \alpha + \alpha e^{-\beta(\kappa - \kappa_0)} \right), \quad (2.11)$$

where α and β are the material parameters.

3 Non-Local Approach

To describe strain localization, to preserve the well-posedness of the boundary value problem and to obtain mesh-independent FE-results, a non-local theory was used as a regularization technique [6], [39]. Usually, it is sufficient to treat non-locally only variable controlling material softening [15], [39] (whereas stresses and strains remain local). It was assumed in elasto-plasticity that the softening parameter κ was non-local

$$\bar{\kappa}(x_k) = \frac{1}{A} \int \omega(r) \kappa(x_k + r) dV, \quad (3.1)$$

where x_k – coordinates of the considered (actual) point, r – distance measured from the point x_k to other material points, ω – weighting function and A – weighted volume. As a weighting function ω , the Gauss distribution function for 2D problems was used

$$\omega(r) = \frac{1}{l_c \sqrt{\pi}} e^{-\left(\frac{r}{l_c}\right)^2}, \quad (3.2)$$

where l_c denotes a characteristic (internal) length connected to microstructure of the material. The averaging in Eqs.3.1 and 3.2 is restricted to a small representative area around each material point. The influence of the points at the distance of $r=3l$ is only about 0.1%. The softening rates $d\kappa_i$ were assumed according to the Brinkreave modified formula [15] (independently for both yield surfaces)

$$d\bar{\kappa}_i(x_k) = (1-m)d\kappa_i(x_k) + \frac{m}{A} \int \omega(r) d\kappa_i(x_k + r) dV, \quad (3.3)$$

where m is the non-local parameter which should be greater than 1 to obtain mesh-independent results [10]. Equation 3.3 can be rewritten as [15]

$$d\bar{\kappa}_i(x_k) = d\kappa_i(x_k) + m \left(\frac{1}{A} \int \omega(r) d\kappa_i(x_k + r) dV - d\kappa_i(x_k) \right), \quad (3.4)$$

Since the rates of the hardening parameter are not known at the beginning of each iteration, the extra sub-iterations are required to solve Eq.3.4. To simplify the calculations, the non-local rates were replaced by their approximations $d\kappa_i^{est}$ calculated on the basis of the known total strain rates [15].

$$d\bar{\kappa}_i(x_k) \approx d\kappa_i(x_k) + m \left(\frac{1}{A} \int \omega(r) d\kappa_i^{est}(x_k + r) dV - d\kappa_i^{est}(x_k) \right), \quad (3.5)$$

In the damage mechanics model, the equivalent strain measure $\tilde{\varepsilon}$ was replaced in Eqs. 2.7 and 2.9 by its non-local definition $\bar{\varepsilon}$

$$\bar{\varepsilon}(x_k) = \frac{1}{A} \int \omega(r) \tilde{\varepsilon}(x_k + r) dV, \quad (3.6)$$

Both models enhanced by non-local terms were implemented in the Abaqus Standard program [1] with the aid of the subroutine UMAT (user constitutive law definition) and UEL (user element definition) [10]. The FE-simulations were performed under plane strain conditions. The geometric nonlinearity was taken into account. The non-local averaging was performed in the current configuration. The quadrilateral elements composed of four diagonally crossed triangles were used to avoid volumetric locking [42].

4 FE - Simulations

4.1 Uniaxial Tension

4.1.1 Elasto-Plastic Model

To study the size effect, the calculations were carried out with 3 different concrete specimens with one notch whose dimensions (from Fe-simulations by Gutierrez and de Borst [22]) and boundary conditions are given in Fig.4.1. The lower and upper edge of the specimen were smooth (no shear stress). The nodes along the bottom edge were fixed in vertical direction. To preserve the stability of the specimen, the node in the middle of the bottom was fixed in the horizontal direction. The deformation was imposed by prescribing a vertical displacement u along the upper edge. To introduce a non-homogenous strain field, a small notch at the left side at mid-height was assumed. Three different meshes were used with 1500, 2620 and 5100 triangular elements for the small, medium and large specimens, respectively. When calculating non-local quantities close to the notch, the so-called “shading effect” was considered (i.e. the averaging procedure considers the notch as an internal barrier that is shading the non-local interaction [29]). In the elastic region, the modulus of elasticity was taken as $E=30$ GPa and Poisson’s ratio as $\nu=0.20$. The diagram describing

the tensile stress σ_t versus the softening parameter κ_2 is shown in Fig.4.2. To simplify calculations, a linear relationship $\sigma_t=f(\kappa_2)$ was assumed with the softening modulus in tension equal to $H_t=3.0/(3.0\times 10^{-3})=1000$ MPa. The tensile strength was equal $f_t=3.0$ MPa. The non-locality parameter $m=2$ was chosen on the basis of initial own FE-studies [10] and other studies [29]. Higher values of m resulted in unrealistic large shear zone widths. The characteristic length was taken as $l_c=15$ mm.

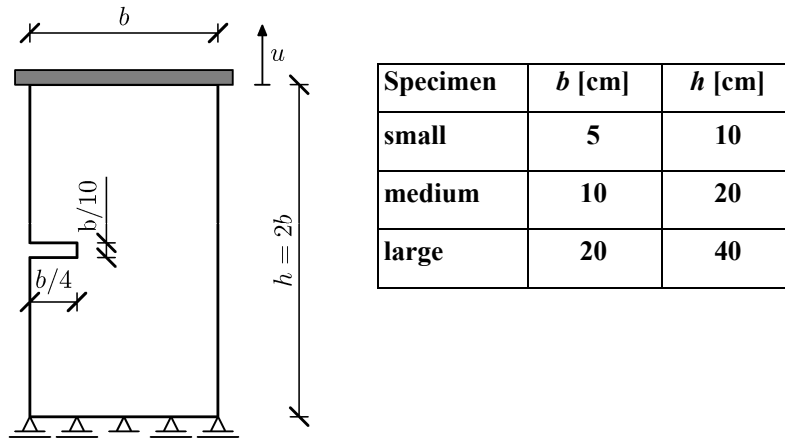


Fig. 4.1. Geometry and boundary conditions of the specimen subjected to uniaxial tension ([22])

Fig.4.3 presents the normalized load-displacement curves for different sizes of the concrete specimen of Fig.4.1 (P – resultant vertical force, u – vertical displacement of the top edge).

The size effect is significant, i.e. the smaller the specimen, the larger the normalized strength and the larger the material ductility. The plots of the non-local softening parameter $\bar{\kappa}_2$ in the neighborhood of the notch for 3 different specimens are shown in Fig. 4.4.

The calculated height of the localized zone increases with the specimen size and is equal to 5.0 cm ($3.3\times l_c$), 6.0 cm ($4\times l_c$) and 7.0 cm ($4.6\times l_c$) for the small, medium and large specimens, respectively. The results are qualitatively similar to those obtained with the second-gradient elastoplastic constitutive model by Gutierrez and de Borst [22].

The maximum loads obtained from FE-simulations for concrete were compared with the energetic size effect law given by Bazant [5], [9] which is valid for structures with pre-existing notches or large cracks:

$$\sigma = \frac{Bf_t}{\sqrt{1 - D/D_0}}, \quad (4.1)$$

where σ - nominal strength, B - dimensionless geometry-dependent parameter which depends on the geometry of the structure and of the crack, D - specimen size (equal to the specimen height h) and D_0 - size-dependent parameter called the transitional size.

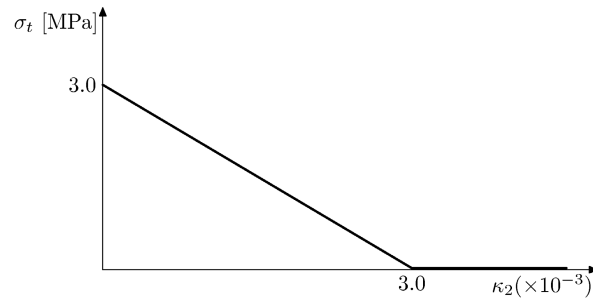


Fig. 4.2. Assumed curve $\sigma_t = f(\kappa_2)$ in tensile regime using the elasto-plastic model for uniaxial tension (σ_t – tensile stress, κ_2 – softening parameter)

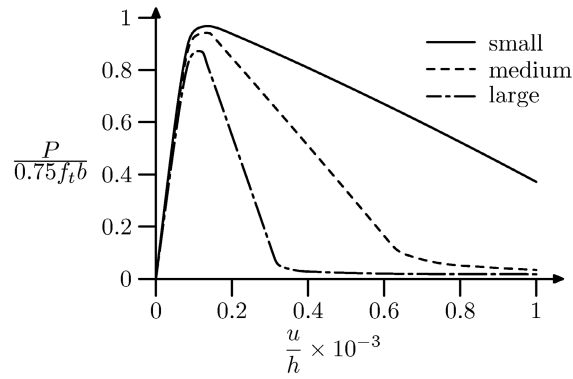


Fig. 4.3. Calculated normalized load-displacement curves for uniaxial tension (elasto-plastic model with non-local softening)

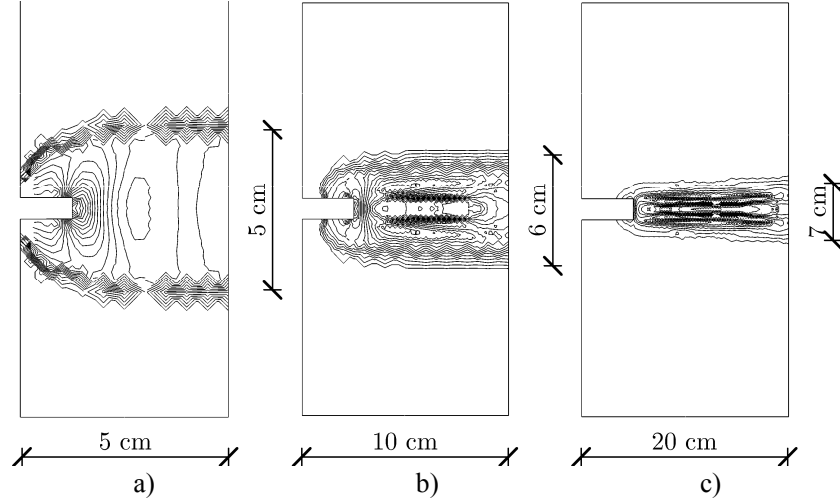


Fig. 4.4. Calculated contours of the nonlocal softening parameter \bar{K}_2 for uniaxial tension of a large (a), medium (b) and small (c) specimen within elasto-plasticity with non-local softening) (different scale is used in 3 specimens)

Eq.4.1 can be rewritten as:

$$\frac{1}{\sigma^2} = \alpha D + c \quad \text{with} \quad \alpha = c/D_0 \quad \text{and} \quad Bff = 1/\sqrt{c}, \quad (4.2)$$

To find parameters B and D_0 from the FE-analysis, a linear regression was used. Fig.4.5 present the differences between stresses σ from the FE-calculations ($\sigma = P/(0.75bt)$, b - element width, $t=1.0$ m – size in the third direction) and those obtained from Eq. 4.2. A good agreement with Bazant's size effect law [9] was obtained. The normalized strength decreases almost linearly with the size ratio h/l_c in the considered range.

4.1.2 Damage Model

The problem of a double notched specimen under uniaxial tension was experimentally investigated by Hordijk [25]. The geometry of the concrete specimen (width $b=60$ mm, height $h=125$ mm, thickness in the out-of-plane direction $t=50$ mm) and boundary conditions (similar as in Fig.4.1) are presented in Fig.4.6. Two symmetric notches $5 \times 5 \text{ mm}^2$ were located at the mid-point of both sides of the specimen. The modulus of elasticity was equal to $E=18$ GPa and the Poisson's ratio was $\nu=0.2$. The following

parameters of the damage model were chosen (using Eqs.2.7 and 2.11): $\kappa_0 = 2.1 \times 10^{-4}$, $\alpha=0.96$, $\beta=500$ and $k=10$. The characteristic length l_c was assumed to be 5 mm. Three different FE-meshes were used: coarse (1192 triangular elements), medium (1912 triangular elements) and fine (4168 triangular elements), Fig.4.7.

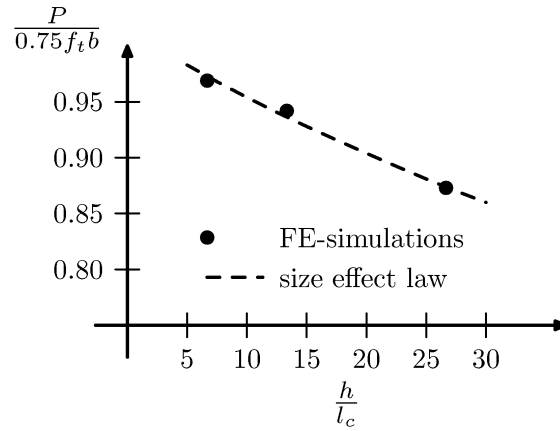


Fig. 4.5. Relationship between calculated normalized concrete strength $\sigma=P/(0.75bt)$ from uniaxial tension and ratio h/l_c (elasto-plastic model with non-local softening) compared to the size effect law by Bazant [5]

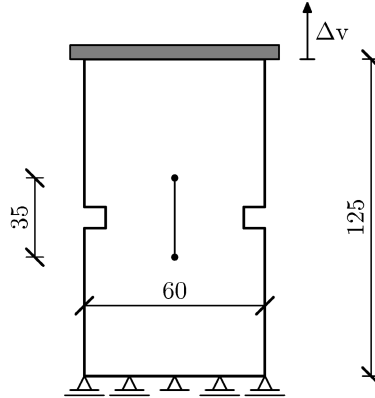


Fig. 4.6. Geometry and boundary conditions of a specimen with a notch under uniaxial tension (dimensions are given in mm)

The calculated contours of the damage parameter κ in the specimen are shown in Fig.4.8 at residual state. The results are mesh-independent since the width of the damage region in the mid-region of the specimen is always the same. The width of the localization zone is approximately 22 mm ($4.4 \times l_c$).

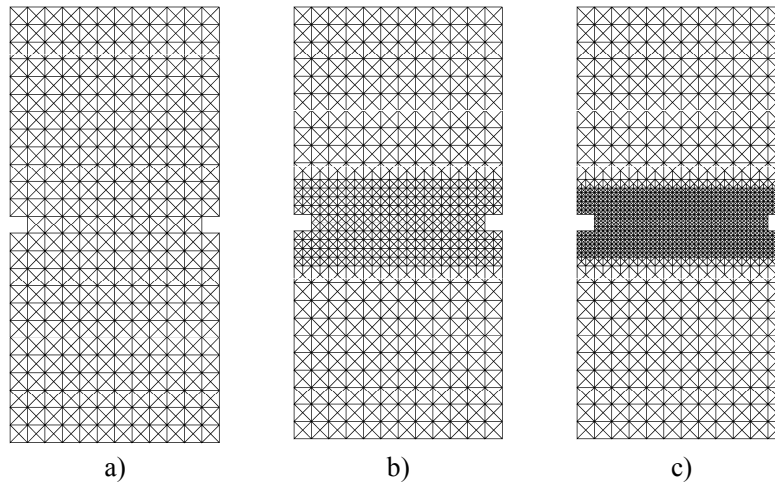


Fig. 4.7. FE-meshes used for calculations of uniaxial tension: a) coarse, b) medium, c) fine

Fig.4.9 presents the nominal stress–elongation tensile curves for all meshes as compared to the experimental curve [25]. The elongation δ in Fig.4.9 denotes the elongation of the specimen above and below both notches at the height of 35 mm (Fig.4.7). It was measured experimentally by 4 pairs of extensometers with a gauge length of 35 mm. The vertical normal stress was calculated by dividing the calculated resultant vertical force along the upper edge by the specimen cross-section of $50 \times 50 \text{ mm}^2$. The calculated load-displacement curves of Fig. 4.9 practically coincide for the different meshes. They are also in a satisfactory agreement with the experimental curve [25], although a small deviation between the theory and the experiment (in particular after the peak) takes place.

In addition, the influence of the characteristic length l_c of micro-structure on the specimen behaviour was investigated. The FE-calculations were performed with l_c in the range from 2.5 mm up to 10.0 mm. The obtained

load-displacement curves are presented in Fig. 4.10. The larger the characteristic length, the higher the maximum tensile stress. The inclination of all curves to the horizontal after the peak becomes smaller with increasing l_c (the material becomes more ductile). The width of the localized zone was 12 mm ($4.8 \times l_c$ for $l_c = 2.5$ mm), 22 mm ($4.4 \times l_c$ for $l_c = 5$ mm), 34 mm ($4.5 \times l_c$ for $l_c = 7.5$ mm) and 44 mm ($4.4 \times l_c$ for $l_c = 10$ mm), Fig. 4.11.

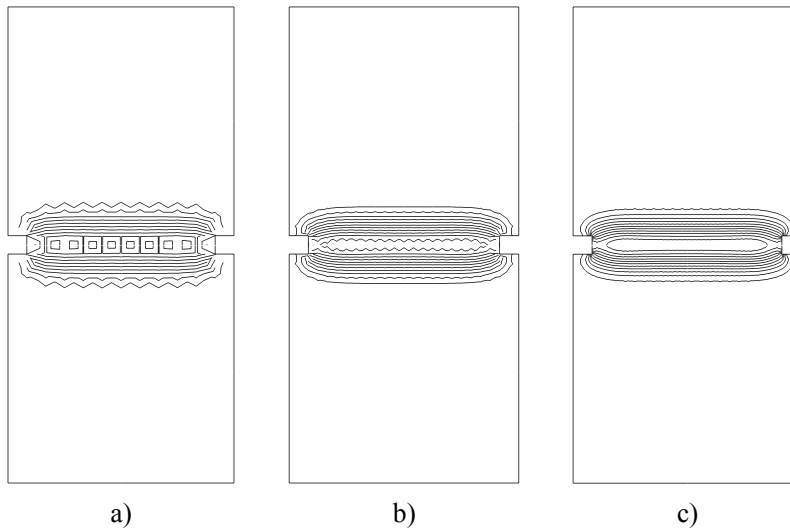


Fig. 4.8. Calculated contours of the damage parameter κ in a specimen under uniaxial tension for: a) coarse, b) medium and c) fine mesh (damage model with non-local softening)

The results are in a good accordance with the FE-results by Pamin [36] and Peerlings et al. [37] using a second-gradient damage continuum model.

4.2 Three-Point Bending

The behaviour of the concrete beam with a notch at the bottom at mid-span and free ends during three-point bending was simulated. This behaviour was experimentally investigated by Le Bellego et al. [31], and later numerically simulated by Le Bellego et al. [31] and Rodriguez-Ferran et al.

[40] with a non-local damage approach. Three different beams were used in laboratory tests: small ($h=8$ cm), medium ($h=16$ cm) and large one ($h=32$ cm). The beam length was $L=3h$. The geometry and boundary conditions of the beam are presented in Fig.4.12. The loading was prescribed at the top edge in the mid-span via displacement. Three different FE-meshes were assumed: with 1534, 2478 and 4566 triangular elements for a small, medium and large specimen, respectively. Due to the symmetry of the problem, only half of the beam was modeled. In the simulations, the modulus of elasticity was taken as $E=38.5$ GPa and the Poisson ratio as $\nu=0.2$.

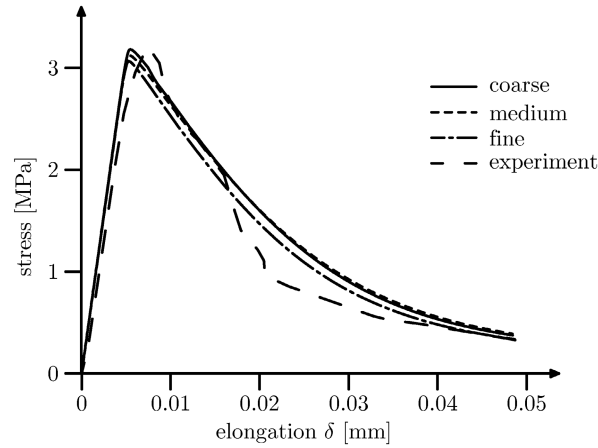


Fig. 4.9. Calculated stress–elongation diagrams for a specimen under uniaxial tension (damage model with non-local softening) with different FE-meshes compared to the experimental diagram [25]

4.2.1 Elasto-Plastic Model

In the tensile regime, the Rankine criterion (Eq.2.4) using the exponential curve in the softening regime proposed by Hordijk [25] was defined

$$\sigma_t(\kappa_2) = f_t \left\{ \left[1 + \left(c_1 \frac{\kappa_2}{\kappa_u} \right)^3 \right] \exp \left(-c_2 \frac{\kappa_2}{\kappa_u} \right) - \frac{\kappa_2}{\kappa_u} (1 + c_1^3) \exp(-c_2) \right\}, \quad (4.3)$$

where σ_t – tensile stress, f_t – tensile strength of the concrete, κ_u – ultimate value of the softening parameter and c_1 , c_2 – constants equal to 3 and 6.93,

respectively. Two different characteristic lengths were assumed in the FE-analyses, namely $l_c=5$ mm and $l_c=10$ mm. For each characteristic length, the following material parameters were chosen: $f_t=3.6$ MPa, $\kappa_u=0.005$ ($l_c=5$ mm), and $f_t=3.3$ MPa, $\kappa_u=0.003$ ($l_c=10$ mm) with $m=2$. They were adopted to obtain the best agreement between the load-displacement diagrams from FE-analyses and laboratory tests [31]. The internal friction angle was equal to $\varphi=10^\circ$ [1] and the dilatancy angle $\psi=5^\circ$. The compressive strength was equal to $f_c=40$ MPa. The softening modulus in compression was $H_c=0.8$ MPa. The material parameters in the compressive regime did not influence the FE-results.

Fig. 4.13 presents the load-displacement curves for all beams obtained from FE-calculations with the characteristic length of $l_c=5$ mm and $l_c=10$ mm compared with experiments. A satisfactory agreement was obtained. The FE-results overestimate slightly the load bearing capacity of the small and medium beam and underestimate the maximum load for the large beam. The results demonstrate that a characteristic length can be only determined on the basis of the measured width of strain localization (from an inverse identification process) but not from the measured load-displacement curves.

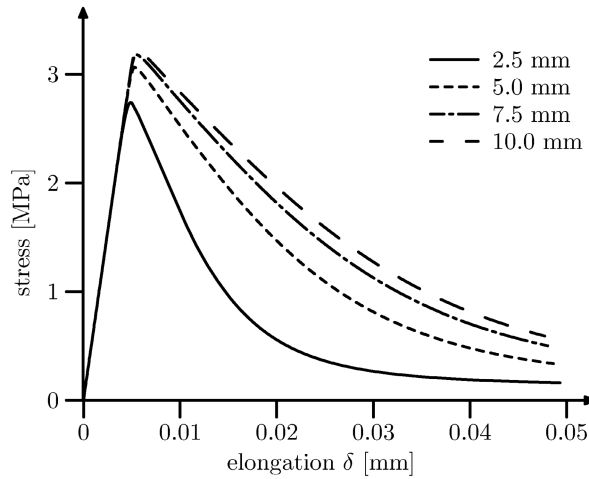


Fig. 4.10. Calculated stress–elongation diagrams using different characteristic lengths l_c for a specimen under uniaxial tension (damage model with non-local softening)

The width of the calculated localization zone was about 20 mm ($4 \times l_c$) for $l_c = 5$ mm (Fig.4.13), and 45 mm ($4.5 \times l_c$) (small beam), 40 mm ($4 \times l_c$) (medium beam, Fig.4.13) and 35 mm ($3.5 \times l_c$) (large beam) for $l_c = 10$ mm, respectively. It did not depend on the mesh size.

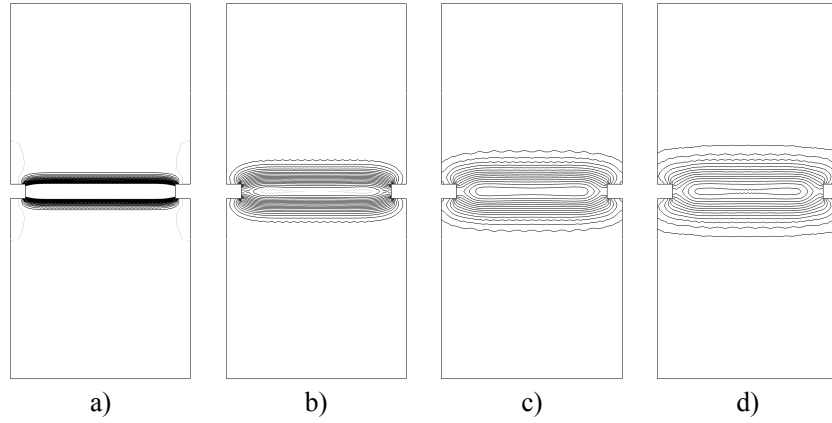


Fig. 4.11. Calculated contours of the damage parameter κ in a specimen under uniaxial tension: a) $l_c = 2.5$ mm, b) $l_c = 5$ mm, c) $l_c = 7.5$ mm, d) $l_c = 10$ mm (damage model with non-local softening, fine mesh)

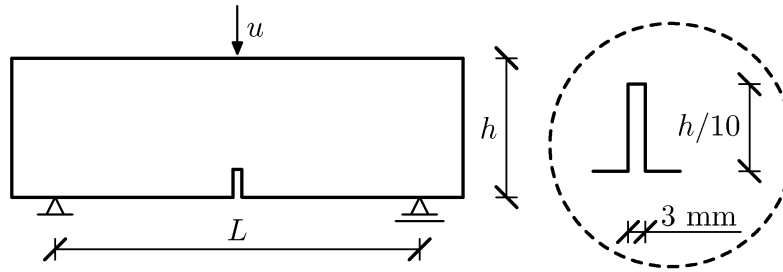


Fig. 4.12. Geometry of the beam and boundary conditions [31]

4.2.2 Damage model

Two different characteristic lengths were again assumed, namely $l_c=5$ mm and $l_c=10$ mm. For each l_c , the following material parameters were chosen: $\kappa_0=7\cdot 10^{-5}$, $\alpha=0.99$, $\beta=600$ ($l_c=5$ mm), and $\kappa_0=6.25\cdot 10^{-5}$, $\alpha=0.99$, $\beta=1000$ ($l_c=10$ mm) (using Eqs.2.9 and 2.11). A satisfactory agreement between FE-results and experimental ones was achieved in both cases (Fig. 4.14).

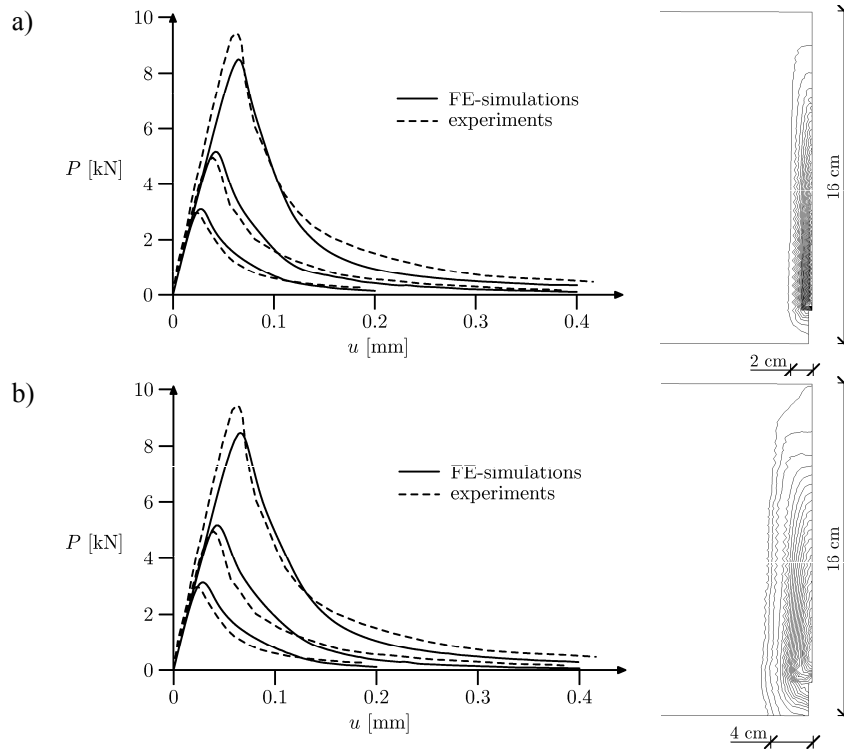


Fig. 4.13. Load-displacement curves from experiments [31] and FE-simulations, and calculated contours of the non-local parameter: a) $l_c=5$ mm, b) $l_c=10$ mm (elasto-plastic model with non-local softening, beam height $h=160$ mm)

The width of the localization zone at the end of the loading process was equal to 40 mm ($8\times l_c$) (small beam), 35 mm ($7\times l_c$) (medium beam, Fig.4.14) and 40 mm ($8\times l_c$) (large beam) for $l_c=5$ mm, and 50 mm ($5\times l_c$) (small beam), 60 mm ($6\times l_c$) (medium beam, Fig.4.14) and 80 mm ($8\times l_c$)

(large beam) for $l_c=10$ mm, respectively. It did not depend on the mesh size. The width of the localization zone was not constant and it increased during loading [36]. Similarly as in elasto-plasticity, the FE-calculations overestimate slightly the load bearing capacity for the small and medium beam and underestimate the maximum load for the large beam. The same conclusions were drawn by Le Bellego et al. [31] and Rodriguez-Ferran et al. [40] from their simulations, although they used different definitions of the equivalent strain $\tilde{\varepsilon}$ and evolution laws.

The maximum loads obtained from FE-simulations were compared again with the energetic size effect law given by Bazant (Eq.4.1) (Fig.4.15). A good match was achieved. The normalized strength decreases almost linearly with increasing size ratio h/l_c in the considered range.

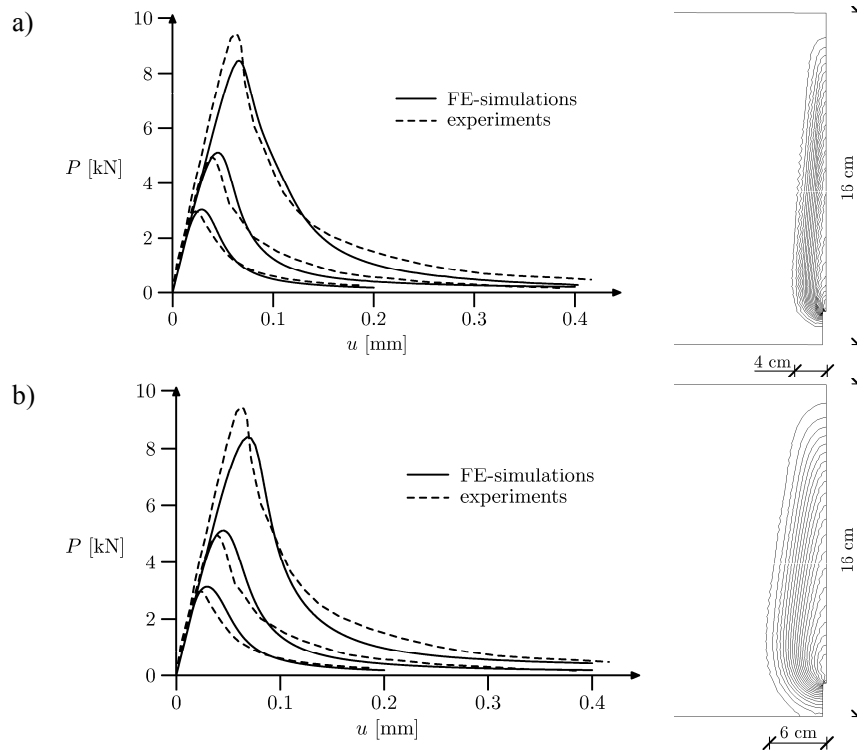
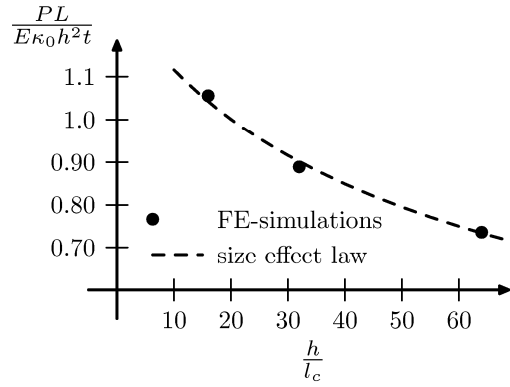
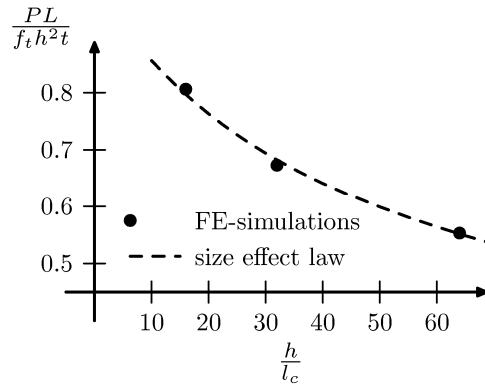


Fig. 4.14. Load-displacement curves from experiments [31] and FE-simulations and calculated contours of the non-local parameter for beam height $h=160$ mm: a) $l_c=5$ mm, b) $l_c=10$ mm (damage model with non-local softening)



a)



b)

Fig. 4.15. Relationship between the calculated normalized loads: $(PL)/(E\kappa_0 h^2 t)$ and $(PL)/(f_t h^2 t)$ during bending (with $l_c=5\text{mm}$) and the ratio h/l_c as compared to the size effect law by Bazant [5] within: a) damage mechanics, b) elasto-plasticity

5 Conclusions

The FE-calculations have shown that both constitutive models: elasto-plastic and damage with non-local softening are able to capture strain localization and related size effect in problems characterized by the failure mode I. The obtained FE-results did not suffer from the mesh sensitivity.

A satisfactory agreement between numerical simulations and laboratory experiments with respect to the load-displacement curves was achieved.

The larger the ratio between the characteristic length of micro-structure and the specimen size, the higher both the material strength and ductility of the specimen.

The width of the localized strain zone in concrete specimens increases with increasing ratio between the characteristic length of micro-structure and the specimen size.

The width of the localized strain zone is for uniaxial tension about $(3.3-4.5) \times l_c$ within elasto-plasticity and $(4.5-5.0) \times l_c$ damage mechanics. The width of the localized zone in beams was larger in FE-analyses with a damage model (about $(5-8) \times l_c$) than with an elasto-plastic model (about $(3.5-4.5) \times l_c$). It was similar in beams for the characteristic length of 5 mm, and decreased in elasto-plasticity and increased in damage mechanics with increasing beam size for the characteristic length of 10 mm.

The size effect decreases almost linearly with decreasing ratio between the specimen size and characteristic length. It is in agreement with the size effect law by Bazant.

A characteristic length of micro-structure can be only identified on the basis of measurements of strain localization.

The calculations on strain localization in concrete will be continued. To include plastic deformation and hardening, the damage model will be combined with an elasto-plastic model [12]. Afterwards, the model will be enriched by anisotropy [51]. To describe a statistical size effect, a spatially correlated distribution of the tensile strength will be assumed [46]. In addition, laboratory tests will be performed wherein the width of strain localization will be measured using a DIC technique.

Acknowledgements

The numerical calculations were performed on supercomputers of the Academic Computer Centre in Gdansk TASK.

References

1. Abaqus (1998) Theory Manual, Version 5.8, Hibbit, Karlsson & Sorensen Inc.
2. Akkermann J (2000) Rotationsverhalten von Stahlbeton-Rahmenecken, Dissertation, Universitat Fridericiana zu Karlsruhe, Karlsruhe

3. Bazant ZP, Bhat PD (1976) Endochronic theory of inelasticity and failure of concrete, *J. Engng. Mech. Div. ASCE*, 102:701-722
4. Bazant ZP, Cedolin L (1979) Blunt crackband propagation in finite element analysis, *J. Engng. Mech. Div. ASCE*, 105, 2:297-315
5. Bazant ZP (1984) Size effect in blunt fracture: concrete, rock, metal. *J. Engng. Mech. ASCE* 110:518-535
6. Bazant ZP, Lin FB, Pijaudier-Cabot G (1987) Yield limit degradation; nonlocal continuum model with local strain. *Proceedings of the International Conference on Computational Plasticity. Barcelona* pp 1757-1780
7. Bazant ZP, Ozbolt J. (1990) Non-local microplane model for fracture, damage and size effect in structures. *J. Engng. Mech. ASCE*, 116:2485-2505
8. Bazant ZP, Shieh CL (1978) Endochronic model for nonlinear triaxial behaviour of concrete, *Nucl. Engng. Des.*, 47:305-315
9. Bazant ZP (2003) *Scaling of Structural Strength*. Hermes-Penton, London
10. Bobinski J, Tejchman J (2004) Numerical simulations of localization of deformation in quasi-brittle materials within non-local softening plasticity, *Computers and Concrete*, 4:433-455
11. Bobinski J, Tejchman J (2005) Modelling of concrete behaviour with a non-local continuum damage approach. *Archives of Hydro-Engineering and Environmental Mechanics, Polish Academy of Sciences*, 1, 52, 2:85-102
12. Bobinski J, Tejchman J (2006) Modelling of strain localization in quasi-brittle materials with nonlocal continuum models. In: Bicanic N, de Borst R, Mang H (eds) *Proc. Euro-C 2006*, pp 301-307
13. de Borst R, Mühlhaus H-B, Pamin J, Sluys L (1992) Computational modelling of localization of deformation. In: Owen DRJ, Onate H, Hinton, E (eds). *Proc. of the 3rd Int. Conf. Comp. Plasticity*, Swansea, Pineridge Press pp 483-508
14. de Borst R, Pamin J, Geers M (1999) On coupled gradient-dependent plasticity and damage theories with a view to localization analysis. *Eur. J. Mech. A/Solids* 18, 6:939-962
15. Brinkgreve RBJ (1994) *Geomaterial models and numerical analysis of softening*. PhD Thesis. Delft University of Technology
16. Chen E (1999) Non-local effects on dynamic damage accumulation in brittle solids, *I. J. Num. Anal. Meth. Geomech.* 23:1-21
17. Chen J, Yuan H, Kalkhof D (2001) A nonlocal damage model for elastoplastic materials based on gradient plasticity theory. Report Nr.01-13, Paul Scherrer Institut, pp 1-130
18. D'Addetta GA, Kun F, Ramm E (2002) In the application of a discrete model to the fracture process of cohesive granular materials. *Granular Matter* 4:77-90
19. Donze FV, Magnier SA, Daudeville L, Mariotti C, Davenne L (1999) Numerical study of compressive behaviour of concrete at high strain rates, *Journal Engineering Mechanics* 1154-1163
20. Dragon A, Mroz Z (1979) A continuum model for plastic-brittle behaviour of rock and concrete, *Int. Journal Eng. Science* 17

21. Groen AE (1997) Three-dimensional elasto-plastic analysis of soils. PhD Thesis, Delft University, pp 1-114
22. Gutierrez MA, de Borst R (2003) Simulation of size-effect behaviour through sensitivity analysis, *Engineering Fracture Mechanics*, 70:2269-2279
23. Herrmann HJ, Hansen A, Roux S (1989) Fracture of disordered elastic lattices in two dimensions. *Physical Rev. B*, 39:637-647
24. Hilleborg A (1985) The theoretical basis of a method to determine the fracture energy of concrete, *Materials and Structures*, 18:291-296
25. Hordijk DA (1991) Local approach to fatigue of concrete, PhD dissertation, Delft University of Technology
26. Ibrahimbegovic A, Markovic D, Gatuog F (2003) Constitutive model of coupled damage-plasticity and its finite element implementation, *Eur. J. Finite Elem.* 12, 4:381-405
27. Jirasek M (1999) Comments on microplane theory. *Mechanics of quasi-brittle materials and structures*. In: Pijaudier-Cabot, G, Bittnar Z, and Gerard B (eds), Hermes Science Publications, pp 55-77
28. Jirasek M (2004) Non-local damage mechanics with application to concrete. *Revue Francaise de Genie Civil*. 8:683-707
29. Jirasek M, Rolshoven S (2003) Comparison of integral-type nonlocal plasticity models for strain-softening materials. *Int. J. Engineering Science*, 41:1553-1602
30. Kozicki J, Tejchman J (2006) 2D lattice model for fracture in brittle materials. *Archives of Hydro-Engineering and Environmental Mechanics*, Polish Academy of Sciences, 53, 2: 71-88
31. Le Bellego C, Dube JF, Pijaudier-Cabot G, Gerard B (2003) Calibration of nonlocal damage model from size effect tests. *European Journal of Mechanics A/Solids*, 22:33-46
32. Lemaitre J (1985) Coupled elasto-plasticity and damage constitutive equations, *Computer Methods Appl. Mech. Eng.*, 51:31-49
33. Menetrey P, Willam K J (1995) Triaxial failure criterion for concrete and its generalization, *ACI Structural Journal* 311-318
34. Palaniswamy R, Shah SP (1974) Fracture and stress-strain relationship of concrete under triaxial compression, *J. Struct. Div. ASCE*, 100:901-916
35. Pamin J, de Borst R (1998) Simulation of crack spacing using a reinforced concrete model with an internal length parameter. *Arch. App. Mech.*, 68, 9:613-625
36. Pamin J (2004) Gradient-enhanced continuum models: formulation, discretization and applications, Habilitation Monography, Cracow University of Technology, Cracow
37. Peerlings RHJ, de Borst R, Brekelmans WAM, Geers MGD (1998) Gradient enhanced damage modelling of concrete fracture, *Mech. Cohesion.-Friction. Materials*, 3:323-342
38. Pietruszczak D, Jiang J, Mirza FA (1988) An elastoplastic constitutive model for concrete, *Int. J. Solids Structures*, 24, 7:705-722
39. Pijaudier-Cabot G, Bazant ZP (1987) Nonlocal damage theory. *ASCE J. Eng. Mech.*, 113:1512 -1533

40. Rodriguez-Ferran A, Morata I, Huerta A (2002) Numerical modelling of notched specimens. Proc. WCCM V, Vienna Austria
41. Sakaguchi H, Mühlhaus HB (1997) Mesh free modelling of failure and localisation in brittle materials. In: Asaoka A, Adachi T, Oka F (eds), Deformation and Progressive Failure in Geomechanics, Pergamon, pp 15-21
42. Salari MR, Saeb S, Willam K, Patchet SJ, Carrasco RC (2004) A coupled elastoplastic damage model for geomaterials. Computers Methods in Applied Mechanics and Engineering, 193:2625-2643
43. Schlangen E, Garboczi EJ (1997) Fracture simulations of concrete using lattice models: computational aspects. Engineering Fracture Mechanics 57:319-332
44. Sluys L (1992) Wave propagation, localisation and dispersion in softening solids. PhD Thesis, Delft University of Technology
45. Sluys LJ, de Borst R (1994) Dispersive properties of gradient and rate-dependent media, Mech. Mater. 183:131-149
46. Tejchman J (2006) Effect of fluctuation of current void ratio on the shear zone formation in granular bodies within micro-polar hypoplasticity, *Computers and Geotechnics* 33, 1:29-46
47. Willam KJ, Warnke EP (1975) Constitutive model for the triaxial behaviour of concrete, IABSE Seminar on concrete structures subjected to triaxial stress, Bergamo, Italy, 1-31
48. Wittmann FH, Mihashi H, Nomura N (1992) Size effect on fracture energy using three-point bend tests. Materials and Structures, 25:327-334
49. Vervuurt A, van Mier JGM, Schlangen E (1994) Lattice model for analyzing steel-concrete interactions. In: Siriwardane, Zaman (eds) Comp. Methods and Advances in Geomechanics, Balkema, Rotterdam, pp 713-718
50. Van Vliet MRA, van Mier JGM (1996) Experimental investigation of concrete fracture under uniaxial compression. Mechanics of Cohesive-Frictional Materials, 1:115-127
51. Zhou W, Zhao J, Liu Y, Yang Q (2002) Simulation of localization failure with strain-gradient-enhanced damage mechanics, Int. J. Numer. Anal. Meth. Geomech. 26:793-813

Kinematics of Shear Zone Deformation in Soft Sensitive Clays

V. Thakur¹, S. Nordal¹, H. P. Jostad² and L. Andresen²

¹Geotechnical Division,
NTNU,
Norway.

²Geo-Mechanics Division,
NGI,
Norway.

Summary

Sensitive clays, exhibits softening, are characterized by a response in which shear stress increases monotonically up to a peak value, and decreases with further increase of shear strain i.e. second order work becomes negative, during the shear deformation and will therefore develop excess pore pressure in the shear bands. Due to the low permeability of clays in combination with a generally high deformation rate, the failure process is often considered being undrained and analyzed using a total stress approach. However, if thin localized shear zones develop, local pore-water dissipation will take place. This diffusion process may be important to define the shear bands. To study this process an effective stress based soil model is needed. The model must incorporate a formulation for how excess pore pressures accompany the softening process. Keeping in view, a simple direct shear sample (DSS) test and one dimensional soil column is simulated to analyze the coupled strain softening pore water mechanism. This study is initiated to test the hypothesis that a finite shear band thickness may result for a given deformation rate.

Key words: strain softening, sensitive clays, finite element analyses, shear band

1 Introduction

Since Biot (1941, 1965) have derived the general theory of three dimensional consolidations and initiated research on material instability, much effort has been devoted to the study of multi-phase media (Bardet 1992; Bowen 1982; Schrefler et al. 1990) and solid instability (Bardet 1991; Hill and Hutchinson 1975; Vardoulakis 1981; Bardet, 1990).

The mechanical response of multiphase (solid, air and water) system like geomaterials is of great importance in engineering practice. For instance uneven settlement of underlying soil deposits due to time dependent pore water pressure dissipation from foundation loading, shear creep are the most comely recognized examples. Since the end of 70's several authors have studied strain localization in multiphase materials. Rudnicki (1984) analyzed a fluid saturated rock mass with an embedded weakened layer. Rice (1985) studied the effect of material dilatancy on strain localization in fully saturated frictional material. In recent years, much effort has been developed to devise regularization strategies to simulate the development of shear band in multiphase material without mesh dependency. Rice (1985) and Vardoulakis (1985) extended the instability analyses from single phase to multiphase materials. (Liu, 2003)

According to studies e.g. Schrefler et al (1995), Schrefler et al.(1996), Liu et al. (2001) and Liu (2003), numerical simulation of strain localization in a multiphase material have evidenced that mesh dependency is not severe as in single phase material. The reason is that the governing field eq.s a gradient term is included through Darcy's law, an internal length scale is introduced naturally, resulting thus a regularization for strain localization (Loret and Prevost, 1991 and Schrefler et al. 1995). This internal length scale depends on several material parameters and in particular on the permeability, applied strain rates.

A numerical simulation of biaxial test by Liu (2003) reports the importance of permeability, boundary roughness and excess pore water pressure in strain localization phenomenon for granular material under undrained condition.

This paper presents some initial numerical examples using the finite element simulation to demonstrate the kinematics of shear zone deformation governed by the coupled mechanism.

2 Governing Equation for Coupled Flow

A coupled formulation for the description of deformation and motion of a multiphase media are carried out on the basis of modern mixture theory, see Bowen (1982) Ehlers (1989), Lewis and Schrefler (1998) and Liu (2003). In this study, soil is considered as two phase media, solid and water, sighting the assumption of a fully saturated state.

The equilibrium equation for the soil solid skeleton can be written as

$$\begin{aligned} & \int_V N^T \cdot \rho \cdot \alpha \cdot dV + \int_V B^T \cdot \left(\int_{t-\Delta t}^t \beta \cdot \delta \cdot \dot{p}_w \cdot dt \right) dV \\ & + \int_V B^T \cdot \int_{t-\Delta t}^t \sigma' \cdot dt \cdot dV \\ & = \int_{\Omega} N^T \cdot s \cdot d\Omega - \int_V B^T \cdot \sigma'_t \cdot dV + \int_V N^T \cdot \rho \cdot g \cdot dV \end{aligned} \quad (2.1)$$

where \mathbf{N} is the shape function, \mathbf{a} is the acceleration, \mathbf{B} is the displacement vector, β is the Biot's constant, δ is the Kronecker's delta, p_w is pore water pressure, t is the time, V represents the volume, σ' is the effective stresses which represents the stress associated with the total deformation of the multiphase media, s is the surface traction and \mathbf{g} is the gravity.

In wide sense, in finite element analyses by using multidimensional incremental springs, the element stiffness matrix for soil skeleton can also be written as

$$\mathbf{D} \cdot \Delta \mathbf{v} = \Delta \mathbf{f} \quad (2.2)$$

where \mathbf{D} is fourth order tensor that characterizes the material behavior, $\Delta \mathbf{v}$ is nodal displacements and $\Delta \mathbf{f}$ is corresponding nodal forces. By adding for all elements gives the global increment stiffness matrix.

By including the time derivative of \dot{p}_w , eq. (2.1) can also be written as

$$\tilde{\mathbf{C}} \cdot \Delta V + \mathbf{E} \cdot \Delta p = \Delta \mathbf{f} \quad (2.3)$$

$$\tilde{\mathbf{C}} = \mathbf{K}_o \cdot \mathbf{A} + \mathbf{C} \quad (2.4)$$

$$\mathbf{A} = \int_V N^T \cdot \rho \cdot \mathbf{N} \cdot dV \quad (2.5)$$

$$C = \int_V B^T \cdot {}^t\!-\Delta t D \cdot B \cdot dV \quad (2.6)$$

$$E = \int_V B^T \cdot \beta \cdot \delta \cdot N \cdot S_w dV + \int_V B^T \cdot \beta \cdot \delta \cdot N \frac{w_s}{n} \cdot N \cdot p dV \quad (2.7)$$

$$F_t = \int_{\Omega} N^T \cdot s \cdot d\Omega + \int_V N^T \cdot \rho \cdot g \cdot dV \quad (2.8)$$

$$\Delta f = T_f - f_t^{\text{int}} \quad (2.9)$$

$$T = F_t + A(K_1 \cdot \dot{v} + K_2 \cdot \ddot{v}) \quad (2.10)$$

$$f_t^{\text{int}} = \int_V B^T \cdot \sigma'_t \cdot dV \quad (2.11)$$

and, the continuity eq. of the pore fluid can be as following

$$\begin{aligned} & \int_{\Omega} (N_p)^T \cdot \hat{q} \cdot d\Omega - \int_V (\nabla N_p)^T \cdot k \frac{k_{rp}}{\mu_p} \nabla N_p \cdot p dV - \int_V (\nabla N_p)^T \\ & + \int_V (\nabla N_p)^T \cdot Q^w \cdot N_p \cdot {}^t\!-\dot{p} dV + \int_V (\nabla N_p)^T \cdot \beta \cdot \delta^T \cdot {}^t\!\dot{v} dV = 0 \end{aligned} \quad (2.12)$$

Also, for two dimensional flow cases, Darcy's law can be written as

$$\begin{bmatrix} q_x \\ q_y \end{bmatrix} = \begin{bmatrix} k_x & 0 \\ 0 & k_y \end{bmatrix} \begin{bmatrix} \frac{1}{\gamma_w} & \frac{\partial p_w}{\partial x} \\ \frac{1}{\gamma_w} & \frac{\partial p_w}{\partial y} \end{bmatrix} \quad (2.13)$$

Here p_w is the pore pressure and q designated to nodal flow in x and y directions respectively. Pore water flow follows the Darcy's law which can be rewritten from eq. (2.12)

$$J^T \cdot v + M \cdot p + R \cdot p = q_p \quad (2.14)$$

$$J^T = \int_V N^T \cdot \beta \cdot \delta^T \cdot B \cdot \dot{v} dV \quad (2.15)$$

$$M = \int_V N^T \cdot Q^p \cdot N \cdot dV \quad (2.16)$$

$$R = \int_V (\nabla N)^T \cdot k \frac{k_{rp}}{\mu_p} \nabla N \cdot dV \quad (2.17)$$

$$q_p = \int_V \nabla N^T \cdot k \frac{k_{rp}}{\mu_p} \nabla \rho_p g dV - \int_{\Omega} N^T \cdot \hat{q} \cdot d\Omega \quad (2.18)$$

After rearranging above esq., can be combined in matrix form as

$$\begin{bmatrix} \tilde{C} & E \\ J^T & (M' + \beta^*) \end{bmatrix} \cdot \begin{bmatrix} \Delta v \\ \Delta p \end{bmatrix} = \begin{bmatrix} \Delta f \\ \Delta q_p \end{bmatrix} \quad (2.19)$$

$$M' = \frac{M\beta}{\gamma} \quad (2.20)$$

$$\beta^* = R \cdot \Delta t \frac{\beta}{\gamma} \quad (2.21)$$

3 Pore Water Pressure Generation Dissipation Equation

Considering a one dimensional consolidation situation, a classical eq. of flux flow can be written as

$$\frac{\partial P_w}{\partial t} = c^2 \frac{\partial^2 P_w}{\partial z^2} \quad (3.1)$$

Assuming that drainage path is of infinite length on both sides (and laterally impermeable surface). Then there will not be any boundary conditions, but only the initial condition

$$P_w(z, 0) = f(z) \quad (3.2)$$

where $f(z)$ is the given initial pore water pressure of the bar. By substituting $P_w(z, t) = F(z)G(t)$, we obtained two ordinary differential eq.

$$\frac{\partial^2 F}{\partial z^2} + \psi^2 F = 0 \quad (3.3)$$

$$\frac{\partial G}{\partial t} + c^2 \psi^2 G = 0 \quad (3.4)$$

A complete solution can be written as

$$P_w(z, t; \psi) FG = (A \cos \psi z + B \sin \psi z) e^{-c^2 \psi^2 t} \quad (3.5)$$

Since $f(x)$ is not assumed to be periodic, it is natural to use Fourier integral instead of Fourier series. Also, A and B in eq. (3.5) are arbitrary and re-garded as the function of ψ , can be determined from initial condition.

$$P_w(z, 0) = \int_0^\infty [A(\psi) \cos \psi z + B(\psi) \sin \psi z] d\psi = f(z) \quad (3.6)$$

$$A(\psi) = \frac{1}{\pi} \int_{-\infty}^\infty f(v) \cos \psi v dv \quad (3.7)$$

$$B(\psi) = \frac{1}{\pi} \int_{-\infty}^\infty f(v) \sin \psi v dv \quad (3.8)$$

and hence $u(x, \theta)$ can be written as

$$P_w(z, 0) = \frac{1}{\pi} \int_0^\infty \left[\int_{-\infty}^\infty f(v) \cos(\psi z - \psi v) dv \right] d\psi \quad (3.9)$$

Finally, eq. (3.9) becomes

$$P_w(z, t) = \frac{1}{\pi} \int_{-\infty}^\infty f(v) \left[\int_0^\infty e^{-c^2 \psi^2 t} \cos(\psi z - \psi v) d\psi \right] dv \quad (3.10)$$

The above eq. can be simplified to

$$P_w(z, t) = \frac{1}{2c\sqrt{\pi t}} \int_{-\infty}^\infty f(v) \exp\left\{-\frac{(z-v)^2}{4c^2 t}\right\} dv \quad (3.11)$$

In order to demonstrate characteristic of eq. (3.11), a one dimensional soil column is of length (z) with an embedded shear band thickness (v). In this example, refer Fig. 3.1, the ratio between length of soil column to the shear band thickness is assumed as 10. Soft clays have coefficient of diffusion (c) equals to $0.24 \text{ m}^2/\text{year}$.

A globally undrained soil column is subjected to shear at different strain rates such that the local undrained to a partial drainage situation can be obtained. Excess pore pressure is maximum within contracting shear band due to incompressibility of pore water. At significantly higher strain rate, distribution of excess pore pressure is quasi-static. This also represents a situation where no pore water flow from shear band to the outside body and hence softening can be very rapid due to drastic reduction in effective stress. This situation is recognized as locally undrained condition.

A smooth transition of pore water is observed with decreasing applied strain rates.

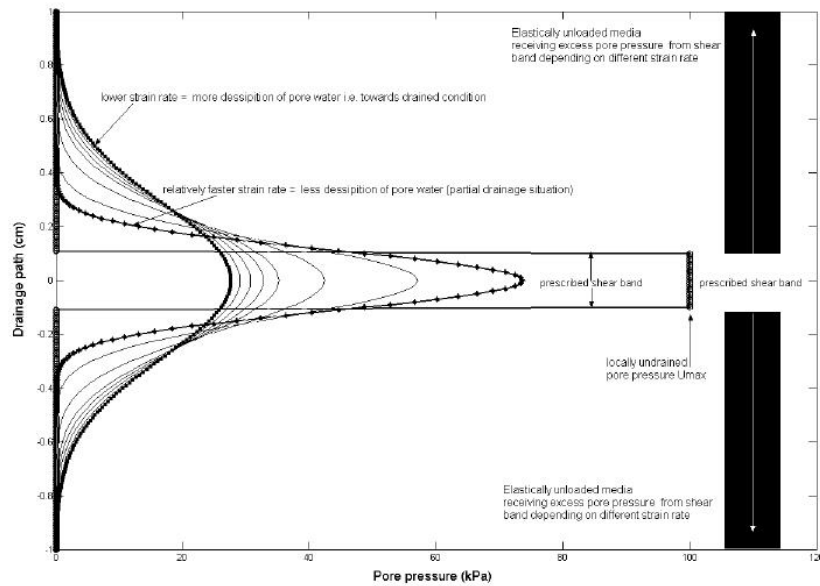


Fig. 3.1. Strain localized pore water diffusion from shear column

4 Finite Element Simulation of Coupled Pore Water and Strain Localization

A finite element model is simulated and practiced for different strain rates. A long natural slope in soft soil shown in Fig. 4.1 is utilized for modeling purpose, however due to specific nature of this study; only a small portion of the slope is modeled.

At the onset of localization, plastic deformation is only concentrated in the shear band zone and rest of the non-localized body have a rigid body motion, which means it is more important to simulate a local model which has embedded shear band and neighborhood explicitly. It is not a very useful to consider complete non-localized elastically deforming slope, because influence of localization will decrease with the increasing distance from the shear band. This statement is true only for the present case.

For simplicity, referring to a local co-ordinate (n, s) system, a direct simple shear model is simulated in finite element code using poro-elastic element in order to have a coupled tangent stiffness matrix where pore water and soil skeleton contributes simultaneously.

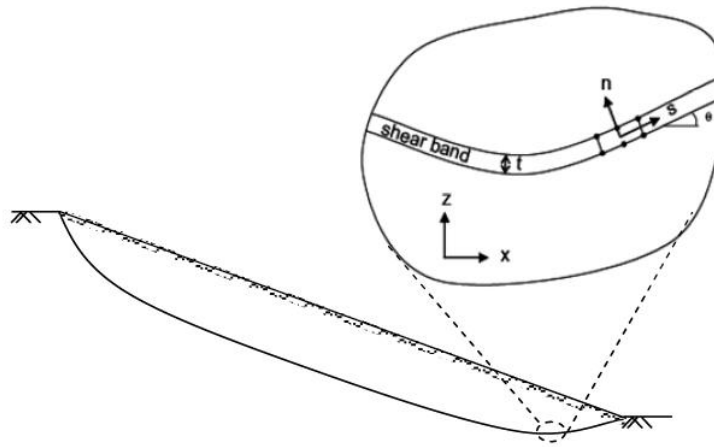


Fig. 4.1 Shear band in a natural slope

Simple elastic perfectly plastic with negative dilatancy material model is considered. Experimentally affiliated parameters have been selected for the modeling purpose, a typical soft and sensitive clay, for example the Norwegian quick clays have shear modulus of 5000 kPa, Poisson's ratio

equal to 0.25, frictional angle 30 degrees, dilatancy of minus 1 degree and horizontal and vertical permeability equal to 1×10^{-6} m/day.

In order to trigger localization, a weak perturbation is embedded within model. Fig. 4.2 represents (a) the DSS model after deformation; (b) localized zone and (c) consequently developed excess pore pressure and pore water flow. A different mesh size and different strain rates were practiced in order to study the model widely.

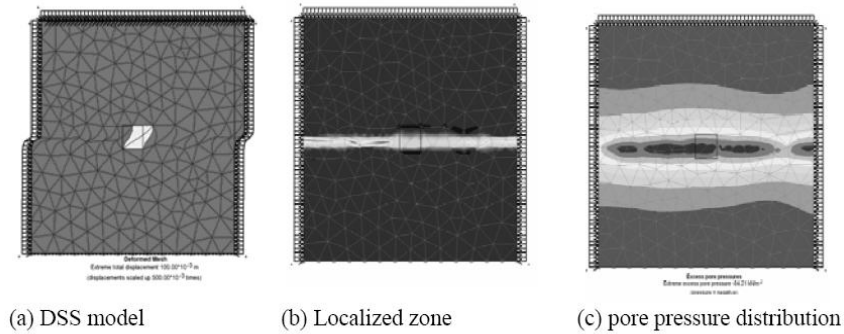


Fig. 4.2 Direct simple shear model

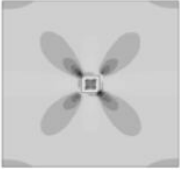

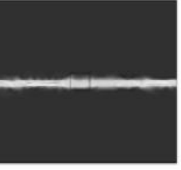

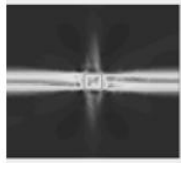


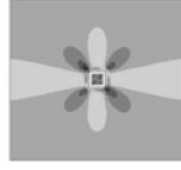

5 Results and Discussion

Phenomenological characteristics of coupled localization obtained from DSS model is discussed pedagogically. Results are presented in different sub-sections, as follows.

5.1 Evaluation of Strain Localization

Strain localization occurs when the deformation in a continuum is localized in well defined but narrow zones of intense straining. In order to illustrate, DSS model has been simulated and studied for different displacement rates to observe time dependent pore water flow and localization. Results are presented in Table 1.

Table 5.1. Evaluation of strain localization at different strain rates

Shear strain level	0.7%	1.2%	2%
→			
Displacement rate			
0.07 mm/min (fastest)			
0.007 mm/min (medium)			
0.014 mm/min (slowest)			

An embedded weak element initiates the localization process and gradually progresses in neighborhood horizontally (by virtue of direct shear). At the onset of localization shear band can propagate in any critical direction (horizontally or vertically) due to symmetric model. But in this case, a guided shear band development in the direction of globally applied displacement is achieved.

For sake of brevity, only three cases are considered where globally applied displacement rates are equal to 0.07mm/min, 0.007mm/min and 0.0014mm/min. In other words, the first two displacement rates are 50 times (0.07mm/min) and 5 times (0.007mm/min) faster than the slowest displacement rate i.e. 0.0014mm/min. Table 1 represents the growth of shear band at three different shear strain level e.g. 0.7%, 1.2% and 2%, for these displacement rates.

The slowest (0.0014mm/min) deformation rate delays the localization occurrence; refer Table 5.1, on other hand fastest deformation rate (0.07mm/min) can cause a rapid localization. In order to justify this statement, for instance, choose a strain level of 1.2 % and compare the

localization pattern for all three deformation rates. At higher rate, shear band developed more dominating and distinct, on other hand, at the slowest rate is plastic strain distribution is more diffused in behaviour and yet to localized in a well defined state.

Excess drainage of pore water from shear band at slower rate causes less reduction in effective stresses and hence post peak stress strain response is not as severe as in case of faster deformation rate. However, end result is same for all the cases, apart from different magnitude of plastic strain within shear band. The same time it must also be noted that finite element analysis is certainly suffer from mesh dependency. However, coupled analyses helps to make well posed situation up to a certain extent but at the higher strain, hydraulic gradient between two gauss point becomes very high, plastic strain distribution also becomes irregular, as shown in Fig. 5.1, and mesh dependent result yields.

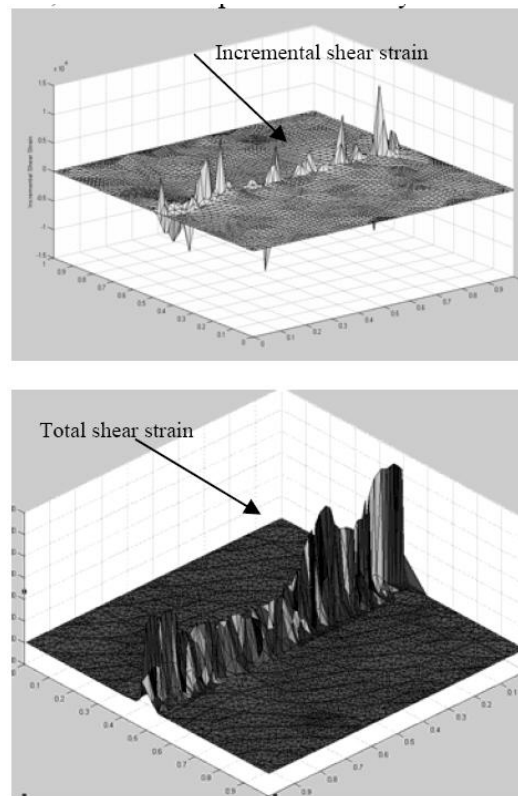


Fig. 5.1. Incremental and total shear strains along the shear band at higher strain

5.2 Effect of Excess Pore Water Pressure

According to laboratory observation, in drained test, depending on the stress level, material exhibits a dilating or contracting behavior. In the undrained test due to incompressibility of pore water will induced pore water pressure changes (Liu 2003).

Desrues (2004) describes that the low over consolidated clays have tendency of local drainage within a global undrained boundary of specimen. By finite element simulation and analytical solution proposed by Thakur et al (2005) shows that generation of excess pore pressure is one of the major reasons for localization in soft and sensitive clays. A rate dependent partial drainage characteristics coupled with localization not only influences the strain softening behavior but also affect the shear band thick-ness. Clays have a global undrained boundary and so global volumetric change must be zero, however internal exchange between contracting zones i.e. shear bands and swelling zone i.e. elastically unloading body is possible.

From Fig. 5.2, at higher deformation rate, high excess pore pressure develops within shear band and vise versa. Higher deformation rate also represent a more undrained situation where pore pressure is accumulated within shear band and thus stain softening is more pronounce. In case of slower rate of deformation, there is sufficient time for pore water to escape and hence accumulated pore water pressure within shear band is also less which ultimately causes a reduction in rate of softening and hence results are less mesh sensitive.

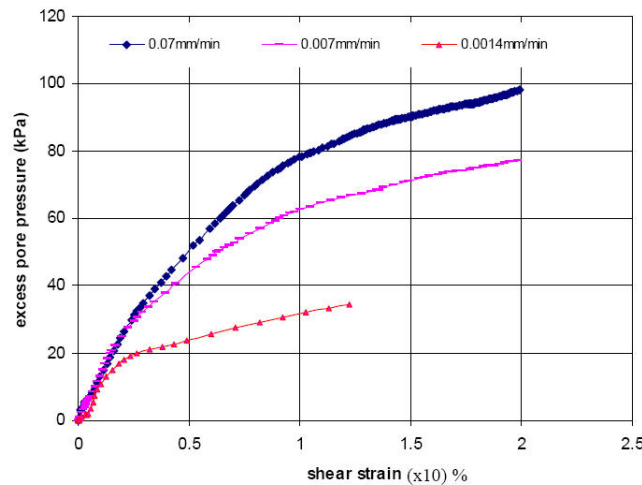


Fig. 5.2. Rate dependent pore water pressure accumulated inside shear band

Sufficient drained condition can also be responsible for a steady state situation, rate of pore water pressure generation and dissipation is constant, that can lead to a definite thickness of shear band. Smooth transition of pore water diffusion is observed at lower strain rates. At higher strain rate, due to lack of sufficient time to reach a steady state situation, pore water distribution profile along and across the shear band is abrupt, refer Fig.5.3.

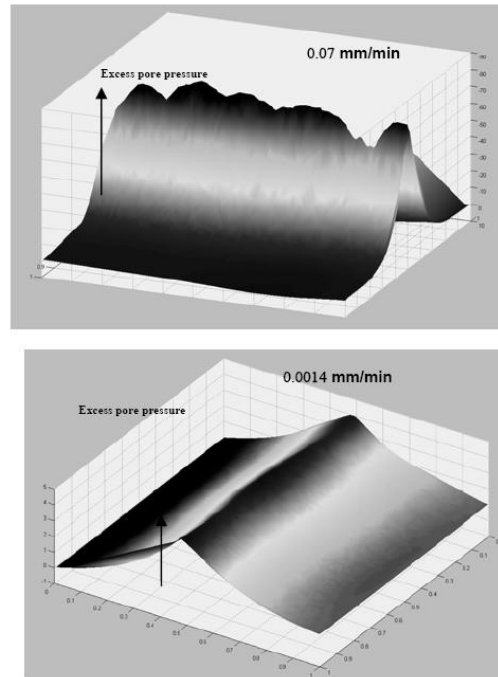


Fig. 5.3. Pore water pressure profile

5.3 Material Behavior

Well known that at the onset of localization domain divide in two parts i.e. localized and elastically unloaded part. Localized part, so called shear band emerges at low displacement and contracts as the strain concentration increases. Due to incompressibility of pore water, excess pore pressure develops and cause reduction in effective stress and so the mobilization. This statement is valid for post peak condition within the perspective of the model used for this study.

Once the partial drainage occurs, there will be a local volume change however global volume of the body remains constant. Shear band reduces to an equal volume replaced by the elastically swollen media. Change in volume depends how fast pore water is transported from shear band. If a situation when the rate of pore water pressure dissipation equal to the rate of pore water pressure generation, i.e. a steady state condition, the contraction in shear band will also stop because effective stresses will not decrease anymore. In such a situation, a definite thickness of shear band can be expected. Fig. 5.4, represents a rate dependent stress strain characteristics, with the decrease in strain rate, strain softening is also reducing.

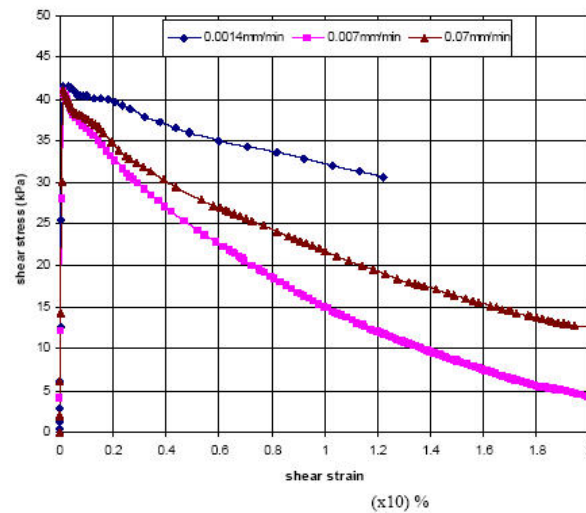


Fig. 5.4. Stress strain curve

From the present study, it is also understandable that simple material models can only predict the real characteristics of localization within a limited gamut. One of the important reasons to obtain mesh sensitive results is due to insufficient loading and unloading criterion in constitutive modeling. This becomes more severe with over simplified simple material models.

Fig. 5.5 shows a typical effective stress path for the DSS model analyses, five different gauss points has been chosen, A,B,C,D and E. Point A of the material and with equally increasing distance (in vertical direction) from shear band respectively. In the beginning A, B localizes, however C, D, E

never reaches to yield and starts unloading. Gauss point A always retains in localization state and hence passes along the failure line. On other hands, point B travel in failure line for some distance and than unloaded due to contracting shear band but parallel to failure line, due to decrease of effective stress caused by gain of high excess pore pressure from the neighborhood. Similarly, point C, D, and E also violate the constitutive rule where elastically unloading must be a rigid body motion without changing its effective stress state.

Especially point B which receives a high excess pore pressure from the shear band (point A) must also develop some plastic strain due to change in mobilization and a mesh independent result can be expected. Since the present model is not robust enough to take in account such type of facts and hence only one gauss point A remain under softening branch and mesh dependent results achieved. In sort, if proper criteria must utilize then a finite element analyses can also be well posed up to certain extent within the contrast of coupled analyses.

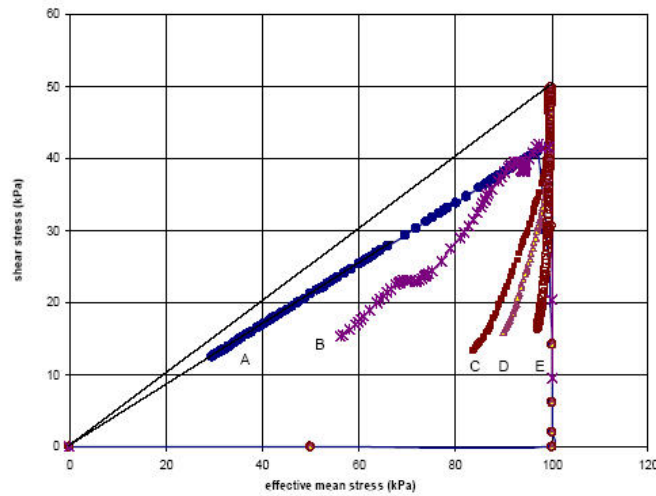


Fig. 5.5. The effective stress path

6 Conclusions

This study brings out the importance of solid fluid interaction within the perspective of strain localization in soft clays. An introductory exercise is chosen to demonstrate the mechanism of shear band and pore water flow using a simple constitutive model in finite element analyses. Rate dependent pore water diffusion from shear band and consequently, strain softening rate are analogously discussed. Inherence regularization in a form of hydraulic gradient helps to handle post peak softening. Elasto-plastic frame work with fluid coupling can also be a sufficient tool to handle strain softening problem. However, in order to validate this statement, a robust model must be utilized and practiced for complete boundary value problems. In short, contracting behavior of shear bands and pore water diffusion not only a complementary characteristics in porous media but also opens a new technique to regularize the ill posed boundary value problem.

Acknowledgements

International Centre for Geohazards, Norwegian University of science and Technology and Norwegian Geotechnical Institute is gratefully acknowledged for their financial support and assistance.

References

1. Bardet JP (1990) Finite element analysis of plane strain bifurcation within compressible solids. *Computers and Structures* 36(6) pp.993-1007.
2. Bowen RM (1982) Compressible porous media models by use of the theory of mixtures. *International Journal of Engineering Science* 20(6) pp.697-735.
3. Desrues J (1996) Strain localization in geomaterials: experimental basis. 8th European autumn school in bifurcation and localization in geomaterials ALERT/Geomaterials, Grenoble, pp.31-32.
4. Ehlers W (1989) On thermodynamics of elasto-plastic porous media. *Arch of Mech.* 41(1) pp.73-99.
5. Lewis RW, Schrefler BA (1998) The finite element method in the deformation and consolidation of porous media. John Wiley & Sons.
6. Liu X (2003) Numerical modeling of porous media response. PhD Thesis, TU Delft, the Netherlands.
7. Liu X., Scarpas A. and Blaauwendraad J. (2001) Finite element investigation of localization in porous media. 10th IACMAG, pp.559-564.

8. Loret B, Prevost JH (1991) Dynamics strain localization in fluid saturated porous media. *ASCE Journal of Engineering Mechanics* 11 pp.907-922.
9. Rice JR (1985) On the stability of dilating hardening for saturated rock masses. *Journal of Geophysics research* 80 pp.1531-1536.
10. Rudnicki JW (1984) Effect of dilatant hardening on the development of concentrated shear deformation in fissured rock masses. *Journal of geophysics Research* 89(B11) pp.9259-9270.
11. Schrefler BA, Sanavia L, Majorana CE (1996) A multiphase medium model for localization and post-localization simulation in geomaterials, *Mech. Cohes-Fric. Materials and structures* 1 pp.95-114.
12. Schrefler BA, Majorana CE, Sanavia L (1995) Shear band localization in saturated porous media. *Arch. Mech.* 47 pp.577-599.
13. Thakur V, Nordal S, Jostad HP, Andresen L (2005) Study on generation dissipation of pore water during shear banding in sensitive clays. 11th IACMAG Turin, Italy, 4 pp. 289-296.
14. Vardoulakis I (1986) Dynamics stability analysis of undrained simple shear on water saturated granular soils. *International Journal of Numerical and Analytical Methods in Geomechanics* 10 pp.177-190.

Bifurcations, Instabilities, Degradation in Geomechanics

Exadaktylos, G.; Vardoulakis, I.G. (Eds.)

2007, XVI, 469 p., Hardcover

ISBN: 978-3-540-49341-9